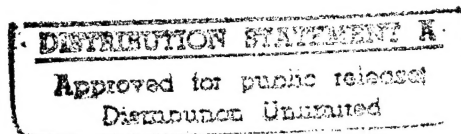DTIC
SELECTED
JAN 0 3 1996
F

ATOMIC LAYER EPITAXY OF THIN DIAMOND FILMS

Prepared by

Andrew Freedman, Gary N. Robinson, David D. Nelson, Jr.,
Paul L. Kebabian and Mark S. Zahniser

Prepared for

Max. N. Yoder
Office Of Naval Research

Final Report
Contract No. N00014-92-C-0196

19951229 015

November 1995

REPORT DOCUMENTATION PAGE

Public reporting burden for this collection of information is estimated to average 1 hour per response, including the time for reviewing instructions, searching existing data sources, gathering and maintaining the data needed, and completing and reviewing the collection of information. Send comments regarding this burden estimate or any other aspect of this collection of information, including suggestions for reducing this burden, to Washington Headquarters Services, Directorate for Information Operations and Reports, 1215 Jefferson Davis Highway, Suite 1204, Arlington, VA 22202-4302, and to the Office of Management and Budget, Paperwork Reduction Project (0704-0188), Washington, DC 20503.

1. AGENCY USE ONLY (Leave blank)	2. REPORT DATE 11 Dec, 1995	3. REPORT TYPE AND DATES COVERED Final Report – Aug 92 – Dec 94

4. TITLE AND SUBTITLE

Atomic Layer Epitaxy of Thin Diamond Films

5. FUNDING NUMBERS

N00014-92-C-0196
S405029SRR04

6. AUTHOR(S)

Andrew Freedman, Gary N. Robinson, David D. Nelson, Jr.,
Paul L. Kebabian and Mark S Zahniser

7. PERFORMING ORGANIZATION NAME(S) AND ADDRESS(ES)

Aerodyne Research, Inc.
45 Manning Road
Billerica, MA 01821

8. PERFORMING ORGANIZATION REPORT NUMBER

ARI-RR-1146

9. SPONSORING / MONITORING AGENCY NAME(S) AND ADDRESS(ES)

Office of Naval Research
800 N. Quincy Street
Arlington, VA 22217-5000

10. SPONSORING / MONITORING AGENCY REPORT NUMBER

11. SUPPLEMENTARY NOTES

12a. DISTRIBUTION / AVAILABILITY STATEMENT

Approved for public release; distribution unlimited

12b. DISTRIBUTION CODE

13. ABSTRACT (Maximum 200 words)

We are attempting to develop an atomic layer epitaxy scheme for the deposition of diamond thin films based on the use of halogenated reagents. To this end, we have been investigating the surface chemistry of diamond and graphite substrates with both fluorine and chlorine atoms. We have discovered, using ultrahigh vacuum surface analysis techniques (x-ray photoelectron spectroscopy (XPS) and low energy electron diffraction), that halogen beam dosing of diamond surfaces indicates that diamond is surprisingly unreactive towards both fluorine and chlorine atoms. Fluorine atoms efficiently adsorb as a carbon-monofluoride moiety at a saturation level of three-quarters of a monolayer at room temperature. The adlayer is ordered on the (111) surface but disordered on the (100) surface. Fluorine desorbs primarily as atomic fluorine over a broad temperature range (500-1200 K), indicating that diamond etching is not a major desorption process. Chlorine atoms bond much more weakly, saturating at a sub-monolayer coverage which is stable to a temperature of only 423 K. These results are ascribed to the severe steric crowding on the diamond surface and the inability of the diamond lattice to deform to accommodate the formation of multiple carbon-halogen bonds.

14. SUBJECT TERMS			15. NUMBER OF PAGES
			16. PRICE CODE

17. SECURITY CLASSIFICATION OF REPORT	18. SECURITY CLASSIFICATION OF THIS PAGE	19. SECURITY CLASSIFICATION OF ABSTRACT	20. LIMITATION OF ABSTRACT
Unclassified	Unclassified	Unclassified	UL

TABLE OF CONTENTS

SUMMARY

Development of electronic devices from diamond has been a major goal of the Ballistic Missile Defense Organization/Office of Innovative Scientific and Technology for the past decade due to the potential of such devices to operate under high radiation and heat stress at extremely high speeds. Other applications include high power and high frequency circuits. Diamond has almost ideal properties for high temperature and high power applications: a bandgap energy of 5.1 eV, the highest thermal conductivity of any substance, and a high breakdown field. But in order for diamond to become a viable semi-conductor material, several large advances in growth techniques must be made. To this date, no verified instances of large scale heteroepitaxy have been reported. This lack of success appears to be due to the propensity (in high pressure reactors) of diamond to nucleate at multiple sites and produce growth of micron-sized crystallites which coalesce into a thin film. In order to grow epitaxial films over large areas, films must be grown two-dimensionally (or in a Frank-Van der Merwe growth mode); this evidently requires a very slow growth rate that would be more relevant to molecular beam epitaxy (MBE) techniques. Furthermore, careful tailoring of films with features having dimensions on the order of a lattice parameter will be required to produce advanced devices such as quantum well structures.

We are attempting to develop an atomic layer epitaxy scheme for the deposition of diamond thin films based on the use of halogenated reagents. Such a scheme would involve the use of self-limiting chemical reactions that would provide control of the deposition process on an atomic scale. To this end, we have been investigating the surface chemistry of diamond and graphite substrates with both fluorine and chlorine atoms. We have discovered, using ultrahigh vacuum surface analysis techniques (x-ray photoelectron spectroscopy (XPS) and low energy electron diffraction), that halogen beam dosing of diamond surfaces indicates that diamond is surprisingly unreactive towards both fluorine and chlorine atoms. Fluorine atoms efficiently adsorb as a carbon-monofluoride moiety at a saturation level of three-quarters of a monolayer at room temperature. The adlayer is ordered on the (111) surface but disordered on the (100) surface. Fluorine desorbs primarily as atomic fluorine over a broad temperature range (500-1200 K), indicating that diamond etching is not a major desorption process. Chlorine atoms bond much more weakly, saturating at a sub-monolayer coverage which is stable to a temperature of only 423 K. These results are ascribed to the severe steric crowding on the diamond surface and the inability of the diamond lattice to deform to accommodate the formation of multiple carbon-halogen bonds.

Thus, a fluorinated surface offers the hope of controlling the rate at which reactive sites are formed in a deposition scheme. Chlorine atoms, which are only weakly chemisorbed on diamond surfaces at very low surface coverages, cannot provide effective control of the surface at reasonable growth temperatures. Another finding of this research is that molecular species are generally very unreactive on a diamond surface; water, oxygen, hydrogen, molecular chlorine and fluorine, and several alkyl halides have proven not to chemisorb. Halogen atoms, on the other

hand, are much more weakly bound to the graphite basal plane and desorb at far lower temperatures than those obtained for diamond surfaces. This behavior is ascribed to the fact that the π-bonded basal plane contains no dangling bonds with which the halogen atoms can interact. Thus, chemisorption takes place through a weak interaction with the delocalized π-electron cloud and is mainly ionic in nature. These results are in accord with high pressure studies of this system which find that halogen atom reactions with graphitic surfaces occurs predominantly at the edge planes of graphite which contain numerous dangling bonds.

As part of this continuing effort to elucidate the chemical bonding properties of carbon surfaces, we have also carried out an XPS study of fluorine atom reactions with self-assembled monolayer (SAM) films of alkanethiolates on gold surfaces which comprise ordered arrays of oriented close-packed sp^3-bonded alkane chains. Most theoretical modeling of hydrogen and fluorine atom reactions with diamond surfaces have assumed that the diamond surface can be adequately modeled as a constrained hydrocarbon and assume covalent interactions with incoming species. More empirical modeling schemes of diamond deposition systems in fact assume that the rate constants of hydrogen atom and methyl radical adsorption and desorption can be extrapolated from gas phase data detailing the reactions of these species with hydrocarbon molecules. Although these modeling efforts have been reasonably successful in predicting at least order of magnitude values for deposition rates, they have been unable to reproduce experimental data which provide microchemical details of the diamond growth process. SAM films of alkane thiols present a highly ordered, constrained and sterically hindered hydrocarbon surface to an incoming radical species and as such, should provide a test of the hydrocarbon surface reactivity model.

In fact, fluorine atoms readily react with such films and form highly stable covalent bonds. Multiple fluorination of individual carbon atoms is observed and fluorine atoms penetrate as much as a third of the way into the ~20Å high films. Although the reaction cross sections are reduced from those found in the gas phase, such hydrocarbon films are much more highly reactive that diamond films. The results presented above indicate that any accurate representation of the diamond surface must adequately take into account the uniquely dense and rigid structure of the lattice. Furthermore, the behavior of halogen atoms on diamond and graphite surfaces as compared to hydrocarbon surfaces is highly suggestive of a strong component of ionic bonding in the carbon surface-halogen atom interaction and the presence of inter-halogen atom repulsion.

As part of this work, we have also developed infrared absorption techniques using lead-salt diode lasers for the quantitative measurement of methyl radical fluxes in diamond reactors. We present a paper which reports the first measurement of pressure-induced line broadening coefficients of methyl radicals in argon and nitrogen atmospheres. The results indicate that the values for these coefficients are comparable to or slightly smaller than those found for methane. Thus, when interrogating methyl radical concentrations using infrared lasers operating at different wavelengths than used in these studies, the values for pressure broadening corrections can probably be extrapolated from those of methane, a far better studied molecule.

The last two chapters in this report present work on more practical aspects of our studies. The first represents a collaboration with Prof. Jeffrey Glass at North Carolina State University and scientists at The Pure Carbon Co. (Stackpole Corporation) in which the tribological properties of both hydrogenated and fluorinated diamond films were studied. The diamond films were subjected to testing on a modified drill press tribotester designed to simulate conditions found in rotary union and joint applications. The major conclusions of this study was that the use of unpolished diamond coated samples, whether fluorinated or not, significantly reduced wear on silicon carbide seal nose pieces under dry conditions compared to uncoated samples. The second paper presents a description of a novel ultrahigh vacuum-compatible electrostatically-driven tuning fork chopper developed with funding from this project. This chopper is intended to produce modulated beams and/or directed fluxes which can be measured using synchronous detection techniques.

HALOGENATION OF DIAMOND (100) AND (111) SURFACES BY ATOMIC BEAMS

Andrew Freedman
Center for Chemical and Environmental Physics
Aerodyne Research, Inc.
45 Manning Road, Billerica, MA 01821

ABSTRACT

Diamond (100) and (111) surfaces have been exposed to beams of atomic and molecular fluorine and chlorine in an ultrahigh vacuum environment. X-ray photoelectron spectroscopy, low energy electron diffraction, and thermal desorption techniques have been used to elucidate the chemistry involved. F atoms add to both the diamond (100)-(1x1) and (111)-(2x1) surfaces to form a carbon-monofluoride species which reaches a saturation level of approximately three quarters of a monolayer at 300 K. In other aspects of their behavior, the diamond surfaces differ. On the (111) surface, the rate of fluorine atom uptake is, to first order, proportional to the open site concentration. Adsorption produces a dimming of the half-order electron diffraction spots, suggesting the breaking of the surface dimer bonds to form regions of the bulk 1x1 reconstruction. The (100) surface uptake rate, though, is second order with respect to open site concentration and no electron diffraction pattern is observed. This difference in behavior between the two surfaces is ascribed to the difference in bonding geometry, leading to severe steric hindrance to ordered adsorption on the (100) surface. The thermal desorption data show fluorine desorption over a wide temperature range (500 K - 1200 K) on both surfaces indicating binding sites with a range of energies. Limited mass spectrometric data indicates that atomic fluorine is the major desorption product. These results imply that atomic fluorine will act in a fashion similar to hydrogen atoms in that they will break surface dimer bonds, desorb from the surface at an appropriate temperature without etching diamond, and abstract any surface hydrogen in deposition systems utilizing halocarbon species. The much larger chlorine atoms weakly chemisorb on the diamond (100) surface, producing a saturation coverage of less than half a monolayer at 300 K. The adlayer neither shows a distinct C-Cl peak in the X-ray photoelectron spectra nor exhibits any electron diffraction pattern. In addition, thermal desorption studies indicate that the concentration of chlorine atoms monotonically decreases to virtually zero as the substrate is heated from 223 K to 423 K. A small residual chlorine concentration remains up to 600 K, presumably due to binding at defect sites. This behavior implies that atomic chlorine will exhibit a less significant role in the surface chemistry of diamond deposition systems.

I. INTRODUCTION

Of diamond's many superlative attributes, including physical and radiation hardness, optical transparency, high thermal conductivity, and low coefficient of friction, chemical inertness stands out given the comparative ease with which diamond can be grown. Diamond is impervious to attack from virtually all chemicals at normal working temperatures. Yet homo- and heterogeneous diamond films have been grown by a number of techniques (hot filament reactors, RF and microwave plasmas, atmospheric plasma torches, laser excitation, and combustion flames) using simple hydrocarbons, hydrogen gas, and occasionally oxygen [1] at substrate temperatures as low as 600 K[2]. Perhaps the most interesting of these schemes from a chemical viewpoint are

those which make use of halocarbon precursors in an excess of hydrogen, in plasmas or conventional chemical vapor deposition systems.[3-8].

Questions arise as to the possible role of halogen atoms in these diamond deposition techniques: Do they play any role in the surface chemistry, or, do they just promote the gas phase production of diamond growth precursor species? Perhaps the most intriguing question is why they can be present at all in a deposition system, when etching of diamond by halogen atoms is thermodynamically favored. Halogen atoms play an essential role in the etching chemistry of electronic materials such as silicon and gallium arsenide, both of which have a diamond-like structure [9,10]. In previous studies, we have investigated these etching systems and found that halogen atoms are extremely reactive, penetrating the topmost layer and forming reaction product layers on both silicon and gallium arsenide at temperatures where product desorption is slow or non-existent [11,12]. While the formation of silicon or gallium fluoride, for instance, is more exothermic than that of carbon tetrafluoride, we note that the production of the latter species from diamond is exothermic by more than 200 kcal mole^{-1} [13], implying the presence of kinetic barriers to formation of etch products in diamond-halogen systems.

Controlled studies of the reactivity of diamond surfaces have been primarily limited to atomic hydrogen, oxygen, and fluorine - elements from the first row of the Periodic Table. The behavior of hydrogen atoms on diamond surfaces is, of course, well studied both from an experimental and theoretical perspective. [14-22] Hydrogen atoms can reversibly and facilely adsorb and desorb, causing the surface to reconstruct in different configurations. Atomic oxygen has recently been shown to form an ordered adlayer on the (100) surface and to desorb in the form of carbon monoxide [19]. Other experiments involving fluorinated compounds have used XeF_2 as a fluorine atom precursor[23,24]; they rely on the precursor molecule to dissociatively chemisorb on the surface to produce atomic fluorine. However, substantial differences in the reactivity of F and XeF_2 on silicon surfaces have been observed [10] and could exist on diamond surfaces as well.

In an earlier study involving the diamond (100) surface, we presented preliminary results on the reactions of fluorine atoms and molecules and found no evidence for etching [25]. Instead, we found that the reaction chemistry on this surface was limited by the steric hindrance caused by the extremely tight lattice structure of diamond. Harris and Belton subsequently performed molecular mechanics calculations at a modest level of sophistication and predicted that this hindrance would not be present on the (111) surface.[26].

We have extended our studies to include reactions of atomic beams of fluorine and chlorine on both the (100) and (111) surfaces of diamond. These experiments are conducted under ultrahigh vacuum conditions using x-ray photoelectron spectroscopy, low energy electron diffraction, and thermal desorption techniques. We will present evidence that fluorine atom coverage on both surfaces at room temperature is limited to less than a monolayer and that atomic fluorine is the

3

major desorption product even though a distinct surface C-F species is formed. Atomic fluorine will attack carbon dimers on the (111)-(2x1) surface to produce a fluorine terminated bulklike configuration. We will also show that chlorine atoms are only weakly chemisorbed and are probably not present on the diamond surface during typical deposition temperatures.

II. EXPERIMENTAL

Studies were performed in an ultrahigh vacuum apparatus comprising a turbomolecular pumped, liquid nitrogen-trapped ultrahigh vacuum reaction chamber (ultimate vacuum - 3 x 10^{-10} Torr) interfaced to an ion-pumped analysis chamber. The diagnostics available in the analysis chamber are x-ray photoelectron spectroscopy (XPS) and low energy electron diffraction (LEED); a quadrupole mass spectrometer, which enables identification of the desorption products, is located in another differentially pumped chamber orthogonal to the reaction chamber. The sample is transferred between chambers using a linear motion feedthrough with sample heating (1200 K) and cooling (120 K) capabilities.

The 5 x 5 x 0.25 mm type 2A diamond (111) and (100) substrates (Dubbeldee Harris) were polished using 0.25 mm diamond grit in oleic acid and rinsed in acetone and ethanol baths in an ultrasonic cleaner to remove any trace of the polishing materials. The diamond sample was clamped to the molybdenum holder using a molybdenum mask. No binder material was used to provide better thermal contact. Chromel-alumel thermocouples were placed in contact with the substrate holder at both ends of the substrate. A measurable temperature gradient exists across the holder, amounting to 50-75 K at 1200 K; we expect the actual temperature of the diamond sample to be within the range of the thermocouples. The temperatures reported in this paper are the lower of the two thermocouple readings. Heating the substrates to ≈ 750 K in vacuum produced surfaces devoid of any contaminants as measured by XPS. Bright 1x1 LEED patterns at 170 eV were obtained for both surfaces, indicating the presence of hydrogenated 1x1 bulk-like reconstructions. [14]. Further heating of the (111) surface to ≈ 1050 K produced intense 2x2 LEED patterns indicating the formation of the dehydrogenated 2 x1 surface. In our experiments, when the (100) surface is heated to 1200 K, the bulk-like 1x1 LEED pattern is retained even though changes in the XPS spectrum indicate loss of hydrogen. There is no evidence of the monohydride symmetric dimer reconstruction leading to a 2 x 1 surface.[25] Undoubtedly, the resultant surface is highly hydrogen deficient although we have no information as to the fractional coverage.

The fluorine atom source has been described in detail elsewhere.[27] Briefly, it consists of a miniature fast flow tube whose output is sampled by a small aperture (40 μm), which produces an effusive atomic or molecular beam. A 5% fluorine in argon gas mixture (2 Torr) flows (500 sccm) through an alumina tube which is surrounded by an Evenson-type microwave discharge cavity, past the aperture, and exhausts through a co-annular passage. Operating the discharge at 70W power produces nearly 100% dissociation of the fluorine. The alumina flow tube is readily

passivated and no recombination of F atoms in the gas or on the walls is seen when the beam is sampled by a mass spectrometer.

In order to produce chlorine atoms, the source is modified by replacing the alumina tube with a halocarbon wax-coated quartz tube [11]. The coating reduces wall-induced recombination. Chlorine atom recombination is further reduced by replacing the flat aperture plate with a nickel skimmer (Beam Dynamics) with a 140 μm aperture. The skimmer wall thickness is only 30 μm at the aperture, minimizing boundary layer effects. Typical dissociation fractions of 50-75 % are reached when using 5% Cl_2 in Ar gas mixtures.

The XPS analyses were performed using a PHI 15 keV, Mg K_α x-ray source and a PHI 15-255 GAR double pass cylindrical mirror electron energy analyzer operated at a bandpass energy of 25 eV. In the 'surface sensitive' mode, the electron energy analyzer's angular resolution is adjusted so that electrons which originate from the surface are preferentially detected. Due to the insulating properties of the diamond sample, significant charging effects were observed. For this reason, all spectra presented here are referenced to the C ls peak (285.0 eV binding energy) of bulk diamond [23]. This peak has a full width at half maximum (FWHM) of 1.4 eV and its assignment is never ambiguous. Fluorine atom concentrations are measured using the F 1s transition at 685.5 eV and chlorine atoms are detected using the Cl 2p transition at ~ 198.5 eV.[28] The LEED diagnostic is of a reverse view variety (Princeton Scientific Instruments). The quadrupole mass filter and electron bombardment ionizer (Extrel) are mounted in a chamber differentially pumped by a cryopump. The mass dependent signal from the Channeltron particle multiplier (Galileo) is recorded in a pulse counting mode. The individual pulses are amplified and converted to TTL pulses by a discriminator (MIT) and routed to 4 MHz counters on a LabMaster data acquisition board (Scientific Solutions) interfaced with an 80286 personal computer. The LabMaster board is also used to control the setting of the mass filter and monitor the temperature of the diamond samples.

In a typical experiment, the annealed diamond sample is exposed to the halogen atom flux for a given amount of time. Dose levels are calculated assuming effusive flow. The chamber pressure is ≈10^{-7} - 10^{-6} Torr during exposure (primarily argon or helium). After sample exposure, the beam source is pumped out and the reaction chamber evacuated to 10^{-9} Torr. The sample is then transferred to the analysis chamber where XPS and LEED spectra are taken. When surface coverage as a function of substrate temperature is being measured, the sample is heated to a given temperature for approximately five minutes and then allowed to cool to room temperature before analysis. (The duration of the heating period did not seem to affect the results.) In the temperature desorption experiments, the sample was placed in front of the opening to the mass spectrometer chamber and the substrate holder temperature was manually ramped.

III. RESULTS

Fluorination

An XPS C 1s spectrum of an annealed diamond (100) surface taken at a substrate temperature of 300 K recorded in a surface sensitive mode is presented in Figure 1. This spectrum consists of a bulk peak at 285.0 eV and a shoulder at lower binding energy associated with a diamond surface state.[23,29] Figure 1 also shows the effect of exposing this surface to a fluence of 40 ML of F atoms (corresponding to a saturation exposure). (1 monolayer (ML) for the (111) and (100) surfaces is defined as 1.8×10^{15} cm^{-2} and 1.6×10^{15} cm^{-2} respectively; these are the number of carbon atoms per unit area in the topmost layer of each surface. The truncated (111) surface has a dangling bond which lies along the surface normal, while the truncated (100) surface has two off-normal dangling bonds.) The intensity of the peak associated with the surface state is reduced and a new peak at high binding energy is formed as a result of the fluorination process. Subtracting the annealed surface spectrum from that of the fluorinated surface produces a difference spectrum, also shown in Figure 1, which unambiguously identifies the annealed diamond surface state at 1.1 eV below the binding energy of the bulk peak and the fluorinated diamond state at 1.8 eV above the bulk peak value. This single, narrow peak for fluorinated diamond is consistent with the formation of a carbon-monofluoride moiety on the surface. Morar, et al. have obtained similar results on the (111) surface when using XeF_2 as a fluorine atom precursor [23]. While the distinct C-F peak denotes the formation of a chemical bond, it should be noted that the shift of 1.8 eV from the bulk is far less than is typically observed for C-F bonds [29]; even when the basal plane of graphite is fluorinated, the shift attributable to the formation of a C-F bond is 2.5 eV [30].

If the assignment of these diamond surface peaks is correct, it is clear that the surface is not completely fluorinated at the point at which the F 1s signal levels off. As described previously [26], the saturation coverage can be estimated by simply comparing the integrated surface C 1s XPS intensities of the surface and fluorinated peaks; in this way, a coverage of three-quarters of a monolayer is obtained. Virtually identical carbon 1s spectra are obtained on the (111) surface (although the C 1s intensity of the (111) surface is 1.5 times that recorded for the (100) surface) indicating a similar surface coverage. These results are in general agreement with experiments using XeF_2 dosing of the (111) surface using backfilling techniques.[23,24] However, Yamada et al. state that at extremely high XeF_2 exposures (>10^4 ML), they observe coverages exceeding a monolayer of fluorine [24]. Their estimates of surface coverage, though, based on the attenuation of the C 1s signal by the fluorine overlayer, are highly uncertain.

Fluorine uptake curves for both the (100) and (111) surfaces for substrates at room temperature as a function of exposure to atomic fluorine are presented in Figure 2. The integrated intensity of the fluorine 1s peak at 685.5 eV has been normalized to the integrated intensity of the carbon peak. Note that the (111) and (100) uptake curves have much different shapes. Although saturation of both surfaces did not occur until 40 ML exposure, the data presented are limited to the

6

initial doses in order to highlight the difference in uptake at low exposures. The fits presented in Figure 2 represent a simple geometric model of the uptake process in which the rate of fluorine uptake is a function of the fluorine surface coverage,θ. The rate of (111) surface uptake, as expected, exhibits a simple first order dependence on fractional fluorine coverage (d θ /dt $\propto$ 1-θ). But, the (100) surface is best fit by a second order rate dependence (d θ /dt $\propto$ [1-θ]^2) - a result which implies that, initially, neighboring reactive sites are affected by an adsorbed fluorine atom. This indicates that the uptake of fluorine atoms on the (100) surface is sterically constrained even at low coverages. In comparison, the uptake on the (111) surface proceeds as expected up to the saturation level as predicted by Harris and Belton [26].

This difference in adsorption mechanism of the two surfaces is reflected in the LEED patterns obtained after fluorination. Figure 3 presents LEED patterns obtained from the (111) surface before and after fluorination. Fluorination decreases the intensity of the half order spots suggesting that the surface dimers of the annealed surface are being broken to form domains of a fluorine terminated 1x1 reconstruction. The half order spots never entirely disappear which is in accordance with the fact that the saturation coverage determined above is less than the monolayer required to completely terminate the surface. Upon desorption of the fluorine atoms, the surface reverts to the 2 x 1 reconstruction. This behavior is quite different from that found on the (100) surface where fluorine addition results in a disordered surface - no LEED pattern can be obtained [25]. To some extent, fluorine atoms on the (111) surface behave in a manner similar to that of hydrogen atoms whose desorption and adsorption to form ordered surfaces are quite reversible. Similar results have been obtained by Yamada et al.on the (111) surface using XeF$_2$ [24] . They interpret these LEED patterns, though, as indicating that the fluorine atoms interact with the π-bonds which form the surface dimer rows without breaking them; they also speculate that F atoms might penetrate into cavities formed between the top two rows. This behavior is highly unlikely; F atoms are known to attack carbon-carbon π -bonds to form C-F sigma bonds. For instance, self-assembled monolayers of vinyl-terminated alkylthiolates have been shown to fluorinate upon exposure to F atoms [31]. Furthermore, given the small distances between atoms in the diamond lattice, it would require an enormous expenditure of energy to distort the diamond lattice to allow fluorine penetration.

The variations in the observations for the (111) and (100) diamond surfaces may be attributable to the differences in surface geometry. The hydrogenated (111) surface contains surface carbon atoms which are bonded to three bulk carbon atoms; the hydrogen-carbon bond axis lies parallel to the surface normal. Upon heating, the surface exhibits a 2 x 2 LEED pattern indicative of the formation of equivalent rotated domains of 2 x 1 symmetry and the XPS spectrum shows characteristic evidence of hydrogen loss[14,32]. This reconstruction satisfies the valence of carbon by forming a hydrogen-free π-bonded carbon chain. Any reaction of incoming halogen atoms with this 2 x 1 reconstruction requires the breaking of carbon-carbon bonds. As the fluorine atoms react with this dimer surface, a reconstruction to the bulk-like configuration occurs, allowing

7

further reaction to proceed without hindrance until a saturation coverage of almost one fluorine atom per carbon is reached is reached.

On the other hand, the (100) surface contains surface carbon atoms which are bonded to only two bulk carbon atoms; there are two bonds at tetrahedral angles above the surface which are nominally terminated by hydrogen atoms. Yang and D'Evelyn have shown, using molecular mechanics calculations, that the fully hydrogenated (100) surface may be thermodynamically unstable with respect to the mono-hydrogen symmetric dimer reconstruction due to large steric repulsions between neighboring hydrogen atoms.[20] They suggest that a plausible equilibrium hydrogenated structure is one of 3 x 1 symmetry in which mono-hydrogenated carbon dimer pairs alternate with dihydrogenated carbons. Replacement of hydrogen atoms by halogen atoms would induce even more strain which may explain the unusual uptake behavior observed here- i.e.-the formation of a completely disordered surface, an uptake rate which is second order in vacancy site concentration, and a saturation coverage which is only a third of the possible value .

The thermal stability of the carbon monofluoride species is exhibited in Figure 4 which presents XPS measurements of the residual fluorine on the (100) and (111) surface as a function of substrate temperature. The results are normalized to the integrated F 1s intensity obtained for a saturated substrate at 300 K. The results are qualitatively similar for both surfaces in that fluorine coverage steadily decreases as a function of temperature, but does not reach zero until 1100 - 1200 K. This indicates that the binding sites exhibit a wide range of bond energies. This is in contrast to the behavior of hydrogenated surfaces which desorb molecular hydrogen over a comparatively narrow range of temperature (1000 - 1300 K) [18,19]. Again, the difference in the shapes of the curves on the two surfaces should be noted. While the (111) surface exhibits a steadily declining residual fluorine concentration, the (100) surface shows evidence of two different desorption regimes with a break at ≈ 700 K. The behavior of the (111) surface upon heating is qualitatively similar to that observed by Yamada, et al.,[24] except that they observe some residual fluorine concentration at a temperature of 1500 K. They state that the fluorine could only be removed upon repeated or prolonged heating of the substrate, a result that differs from that obtained here. This discrepancy is hard to explain even given the difficulty in obtaining accurate temperature measurements on diamond substrates [33]. Both their experiment and ours use thermocouples attached to the molybdenum heater plate to monitor the temperature (the optical pyrometer used in the Yamada experiment will, of course, only measure the Mo surface temperature), so that poor thermal contact between diamond and molybdenum will lead to an overestimate of the diamond temperature.

Identification of the desorption products and measurement of a temperature desorption spectrum was hindered by several experimental problems. First, the signal levels were limited by the small solid angle of collection, a function of the sample-detector geometry. Second, the need to distinguish between peaks at mass-to-charge ratios of 19 (F), 20 (HF), and 18 (background water) required that the quadrupole mass filter be set to greater than unit resolution with a concomitant

8

reduction in mass filter throughput. And third, the wide range of temperature over which fluorine desorbs effectively lowers the rate at which signal is collected at the spectrometer. The molybdenum mask used to hold the sample to the holder also caused a problem since it also adsorbed and desorbed fluorine, thus interfering with the desorption from the diamond sample. Fortunately, desorption experiments carried out without a diamond sample present, using both the XPS diagnostic and mass spectrometer, indicated that most of the fluorine desorption from the molybdenum occurred below 500 K. We did find a desorption signal from the mask, though, at higher temperatures, but did not attempt to subtract it from the diamond spectrum. The temperature desorption spectrum as a function of time and temperature for a fluorinated (111) surface at mass 19 shown in Figure 5 was taken after the substrate had been initially heated to 500 K to minimize the interference from the fluorinated molybdenum. The mass 19 signal has been smoothed. Note the desorption of F atoms over the entire 500 - 1200 K range in accordance with the results shown in Figure 3. We believe that the lack of a well defined falloff at high temperature and a rising baseline can be ascribed to fluorine desorption from the mask.

Our assignment of F atoms as the major desorption product is based on the fact that no signal could be observed at mass peaks corresponding to F_2, CF_4, CF_3, CF_2, CF, or HF. (The mass spectrometer resolution was degraded at the fluorocarbon mass peaks to include possible contributions from hydrogenated fluorocarbons). This result cannot be easily dismissed on the grounds that these species will undergo dissociative ionization to produce a signal at mass 19 in the mass spectrometer. We have experimentally determined that molecular fluorine is primarily observed at its parent peak. Also, cross sections for the production of parent ion peaks from both CF and CF_2 [34] are comparable to that of atomic fluorine[35]. The cross section for dissociative ionization of CF_4 to produce CF_3^+ is several times larger than that of the atomic fluorine ionization cross section[36]. Only the cross section for production of the parent ion of CF_3 is significantly smaller[34]. Coupled with the fact that background noise is significantly lower at masses above 20, we would expect to observe an alternative desorption pathway if its quantum yield were 25%. In view of this, we cannot completely rule out the desorption of halocarbon radicals. The diamond surfaces can be subjected to a limited number (<10) of fluorination and desorption cycles before repolishing of the diamond surface is required to produce a good LEED pattern. However, given that the 2x1 surface can be recovered upon heating, it is unlikely that a significant amount of etching occurs.

Insight into the bonding of fluorine atoms on diamond surfaces can be gained from the work of Pederson and Pickett involving surface cluster calculations of F atom addition to the diamond (100) surface.[37] They find that the addition of two fluorine atoms per surface carbon atom (an ideal 1x1 surface) results in an F-F separation that is less than is found in the diatomic fluorine molecule resulting in an adsorbate-induced strain that rules out a completely fluorinated bulk reconstruction. They have studied three reasonable ideal structures: a 1x1 surface with a physisorbed layer of fluorine atoms adsorbed above the pseudo four-fold hollows present on the

surface; a chemisorbed layer of fluorine atoms bound to the carbon atoms orthogonal to the surface (also 1x1); and a 2x1 surface with bond angles more acute than those found on the 1x1 surface. They find that the first structure (that of a physisorbed layer) gives results that are inconsistent with the observed F 1s binding energy shift observed in the XPS spectra presented in Figure 1. Using calculations on ten-layer diamond slabs (instead of clusters), they observe that the fluorinated 1x1 reconstruction is unstable with respect to the 2x1 dimerized reconstruction. But by comparing the cluster and slab calculations, they also find that significant Coulomb repulsion is introduced due to the charge transfer (estimated to be ≈ 0.25 eV) from the surface carbon atoms to the adsorbed fluorine atoms. This energetically unfavorable situation can be alleviated if the adlayer coverage is reduced to less than a monolayer and the carbon-fluorine bond energy is reduced to less than is found in gas phase fluorocarbon molecules. In addition, one might expect to find co-existing phases of 1x1 and 2x1 fluorinated regions and areas of non-fluorinated carbon with dangling bonds. All this conjecture is consistent with the experimental evidence presented above. The XPS spectra indicate the presence of less than a monolayer of adsorbed fluorine as well as the presence of dangling bonds on the surface. In addition, the absence of a LEED pattern on the fluorinated (100) surface indicates the existence of a largely disordered surface. Furthermore, given that thermal desorption data indicate a range of fluorine-carbon binding energies and the fluorine uptake curve shows a highly unusual behavior, it is reasonable to assume that the diamond surface must continually respond to fluorine addition by minimizing the surface free energy .

Chlorination

In order to ascertain the possible effects of using an impure atomic chlorine source, a diamond (100) surface was first exposed to molecular chlorine. No uptake of chlorine could be observed at either the Cl 2p or C 1s XPS transitions. Thus when the diamond was exposed to the atomic chlorine source, the presence of molecular chlorine in the beam could be ignored. After the (100) surface had been exposed to 40 ML of chlorine atoms, the carbon 1s spectrum remained indistinguishable from that of an annealed surface, indicating different behavior from that of fluorine atoms. The uptake of chlorine as a function of Cl atom exposure is shown in Figure 6; the quality of these data is limited by the poor signal levels and fluctuations in chlorine beam intensity. Note that after a highly efficient initial uptake at low exposures (< 1ML), the uptake rapidly levels off. In order to obtain a value for the saturation coverage, the integrated Cl 2p signal was compared to that obtained for fluorine atoms. After correcting for differences in photo-ionization cross sections and spectrometer detection efficiencies, the chlorine atom saturation coverage at room temperature can be estimated at less than half a monolayer. No LEED pattern could be obtained for the chlorinated surface.

The fact that the carbon spectra of the annealed and chlorinated samples are quite similar would seem to indicate that the chlorine atom-diamond surface interaction is fairly weak. This hypothesis is confirmed by the data shown in Figure 7 which show the residual chlorine left on a

(100) surface as a function of temperature. Note that in this figure, the initial dosing was performed at 223 K; at temperatures below this, there is a possibility that molecular chlorine would physisorb. The residual coverage decreases monotonically with temperature, almost reaching zero at 400 K. The small residual chlorine concentration between 400 and 600 K may be entirely due to adsorption at defect sites. Thus it is clear that chlorine atoms would be totally desorbed at temperatures used in diamond film processing. It is possible that Cl atoms will abstract surface hydrogen since the H-Cl bond strength is slightly higher than the diamond C-H bond strength, although steric constraints may limit this process.

IV. DISCUSSION

These results, in concert with results presented elsewhere, indicate that the presence of fluorine atoms in diamond deposition systems may promote higher quality growth at lower deposition temperatures. Harris and Goodwin [38], following the work of others[39-41], have noted that the deposition rate in conventional diamond deposition systems is limited by three factors. The first factor is the propensity of diamond surfaces to reconstruct at growth temperatures to form carbon-carbon bonds which prevent the successful completion of a diamond layer during the growth process. The second is the rate of addition of methyl radicals to the surface which is proportional to the number of surface free radical sites created by hydrogen atom abstraction. And the third is the accommodation of these methyl radicals on the surface before desorption can take place. This step requires the formation of a second carbon-carbon bond from the methyl group to the surface, a process abetted by the abstraction of a methyl hydrogen by an incoming hydrogen atom.

The evidence presented here indicates that atomic fluorine will attack carbon dimer bonds and cause the surface to reconstruct to a bulk-like configuration. This process stops the formation of growth-inhibiting carbon-carbon dimer species. Furthermore, fluorine atoms can efficiently play the same role as hydrogen atoms in both abstraction processes by abstracting hydrogen atoms from the surface [42] and from methyl groups [31]. Moreover, gas phase data indicate that the rate constants of fluorine atom reactions with carbon-carbon and carbon-hydrogen bonds are greater than that of hydrogen atom reactions at a given temperature. Thus, it may be possible to maintain sufficient diamond deposition rates at lower temperatures. An added benefit of the presence of atomic fluorine is the propensity of fluorine atoms to attack olefinic species [43], inhibiting the buildup of non-diamond species that would propagate through the formation of π-bonded species.

Chlorine atoms, on the other hand, will have a more limited effect on the surface chemistry of diamond deposition systems. They do not form strong surface bonds and desorb from the surface at temperatures well below that found in diamond deposition systems. Furthermore, they do not effect surface reconstruction. But they may play a significant role as part of chlorocarbon free radicals which can be used to deposit carbon on diamond surfaces. Initial reports of diamond

11

growth using hydrogen atoms and CCl_3 radicals have been made by D'Evelyn and co-workers.[8] Bai et al. have also suggested that chlorocarbon radicals such as CH_2Cl may act as more efficient growth species than the methyl radical.[4] Evidently, once sp^3 carbon-carbon bonds have been formed, both thermal desorption of chlorine and the abstraction of chlorine by hydrogen atoms is efficient, allowing for further diamond growth. In addition, chlorine atoms may effectively remove surface hydrogen, opening up potential growth sites. Gas phase rate constants for the abstraction of hydrogen atoms from hydrocarbon molecules are only slightly less than gas kinetic, although the effective rate constant on diamond surfaces may be considerably reduced due to steric interference. [44]

Diamond surfaces show a varying behavior with different first row elements of the Periodic Table. Fluorine and hydrogen atoms exhibit noticeable differences in behavior on diamond surfaces notwithstanding a shared propensity to open carbon dimer bonds and cause surface reconstruction. Fluorine atoms simply do not fit as well on the diamond surface; the (100) fluorinated surface is disordered and the (111) surface is only partially reconstructed to the bulk-like configuration. Furthermore, fluorine atoms are present at much lower coverages than hydrogen on both the (100) and (111) surfaces and are not as stable thermally. Fluorine coverage has decreased to less than half a monolayer at temperatures at which hydrogen is just starting to desorb. The absence of molecular fluorine as a desorption product may also indicate the lack of surface mobility that exists for hydrogen. It is possible that this temperature sensitivity and lack of mobility can be utilized to better control the nucleation process by limiting the number of growth sites; this might promote epitaxial as compared to polycrystalline growth. It should also be noted that atomic oxygen displays a behavior different from either fluorine or chlorine. LEED and thermal desorption studies indicate that oxygen atoms readily attack sp^2-bonded carbon on the (100)-(2x1) diamond surface leading to an ordered oxygen terminated 1x1 surface.[19] The divalent oxygen can be bonded in a bridging configuration involving single bonds to neighboring carbon atoms, or directly doubled-bonded with a single carbon atom on the surface. Upon heating of the oxygenated surface above 400 °C, carbon monoxide desorbs indicating that atomic oxygen will etch diamond at fairly low temperatures.

One question whose answer is only hinted at in these studies is why diamond surfaces exhibit such limited reactivity. As noted before, both silicon and gallium arsenide surfaces are far more reactive with respect to chemical attack by halogen atoms; furthermore, they are also reactive towards halogen molecules as well. But diamond, which has the same lattice structure, is reactive towards halogen atoms only up to a submonolayer coverage in spite of the fact that gas-phase carbon-fluoride and chloride bonds strengths are typically 105 and 80 kcal mole^{-1} respectively.[45] Moreover, it is virtually unreactive at room temperature to gaseous closed shell molecules.[12]

We speculate that the overriding factor is the extremely tight lattice structure of diamond and the rigidity of the bonding that is associated with it. In order to etch diamond, more than one carbon-halogen bond must be formed simultaneously before an energetically allowed etch product

12

can be formed. On silicon and gallium arsenide, this process is enhanced by the ability of fluorine atoms to penetrate the topmost lattice layer. Weakliem and Carter have used ab initio techniques to show that the maintenance of surface *disorder* may be required to promote steady state etching of silicon.[46] Saturation of surface dangling bonds otherwise leads to the termination of reaction. On diamond, as we have seen in the results presented here, there are severe steric constraints to the formation of even one carbon-halogen bond, much less two; penetration of the lattice would be blocked by enormous electron repulsion. The nominal atomic fluorine covalent diameter is comparable to the carbon-carbon bond distance in the diamond lattice. Chlorine atoms are so large, at least one-third larger than fluorine, that they cannot even form a strong interaction with dangling bonds on the dehydrogenated diamond surface. In contrast to the behavior of halogen atoms, atomic oxygen, which readily forms double bonds with carbon, etches diamond.

There are also enormous energetic barriers to deformation of the diamond lattice to overcome this steric hindrance. This structural rigidity is mirrored in diamond's extremely high Debye temperature (2230 K) which is over three times that of silicon, for example. Even the presence of two hydrogen atoms per carbon atom on the (100) surface presents a situation which is energetically unstable with respect to further reconstruction. The importance of these structural barriers to reaction on diamond surfaces is made more clear by comparison to the reactivity of self-assembled monolayers of alkane thiolates [31]. These are ordered arrays of oriented close-packed sp^3-bonded alkane chains chemisorbed on coinage metal surfaces. While the nearest-neighbor distances in many of these systems are comparable to that found in the diamond lattice, the chains are quite flexible at room temperature. Thus, upon exposure of these films to atomic fluorine under ultrahigh vacuum conditions, reaction readily occurs, leading to substantial production of di-fluorinated carbon atoms. These alkane chains exhibit fluorination cross sections that are within two orders of magnitude of gas phase reaction cross sections, indicating that the comparatively open structure and flexibility of their lattice structure compared to that of the diamond lattice enhances reactivity.

This picture of diamond surface reactivity poses a challenge to synthetic organic chemists to develop approaches to the chemical modification of diamond surfaces. Diamond is extremely unreactive to acids and bases except those which are very strong oxidizing agents at high temperatures; molecular oxygen itself does not attack diamond at atmospheric pressure until a temperature of 900 K. Except for metals which are actually solvents at high temperatures (e.g.- iron, cobalt, nickel), the only other reactive species are metals which form carbides (e.g.- tungsten, tantalum, titanium). The fact that a normally highly reactive free radical like atomic chlorine only weakly chemisorbs makes it unlikely that any stable gas phase molecules can adsorb at substantial coverages, much less react at low pressures and normal deposition temperatures.

In summary, halogen beam dosing of diamond surfaces indicates that diamond is surprisingly unreactive towards both fluorine and chlorine atoms. Fluorine atoms efficiently adsorb as a carbon-monofluoride moiety at a saturation level of three-quarters of a monolayer at room

temperature. The adlayer is ordered on the (111) surface but disordered on the (100) surface. Fluorine desorbs primarily as atomic fluorine over a broad temperature range (500-1200 K), indicating that diamond etching is not a major desorption process. Chlorine atoms bond much more weakly, saturating at a sub-monolayer coverage which is stable to a temperature of only 423 K. These results are ascribed to the severe steric crowding on the diamond surface and the inability of the diamond lattice to deform to accommodate the formation of multiple carbon-halogen bonds.

ACKNOWLEGMENTS

REFERENCES

1.   F.G. Celii and J.E. Butler, Ann. Rev. Phys. Chem. 42, 643 (1991)

2.   W.A. Yarbrough, J. Am. Ceram. Soc., 75, 3179 (1992)

3.   D.E. Patterson, R.H. Hauge, J.C. Chu, and J.L. Margrave, U.S. Patent 5,071,677 (December 12, 1991)

4.   B.J. Bai, C.J. Chu, D.E. Patterson, R.H. Hauge, and J.L. Margrave, J. Mat. Res. 8, 233(1993)

5.   R.J. Graham, J.B. Posthill, R.A. Rudder, and R.J. Markunas, Appl. Phys. Lett. 59, 2463 (1991)

6.   R.A. Rudder, G.C. Hudson, J.B. Posthill, R.E. Thomas, and R.J. Markunas, Appl. Phys. Lett. 59, 791 (1991)

7.   M. Kadono, T. Inoue, A. Miyanaga, and S. Yamazaki, Appl. Phys. Lett. 61, 772 (1992)

8.   T.I. Hukka, R.E. Rawles and M.P. D'Evelyn, Thin Sol. Films, 225, 212 (1993)

9.   D.E. Ibbotson, Pure Appl. Chem. 60, 703 (1988)

10. D.L. Flamm in *Plasma Etching*; D.M. Manos, D.L. Flamm Eds.; Academic Press: San Diego, 1989; Chapter 2

11. A. Freedman and C.D. Stinespring, J. Phys. Chem. 96, 2253 (1992)

12. C.D. Stinepring and A. Freedman, Appl. Phys. Lett. 48, 718 (1986)

13. JANNAF Thermochemical Tables, 2nd edition, D.R. Stull and H. Prophet, Eds., NSRDS-NBS 37 (1971)

14. B.D. Pate, Surf. Sci. 165, 83 (1986)

15. G.D. Kubiak and K.W. Kolasinski, Phys. Rev. B39, 1381 (1989)

16. A.V. Hamza, G.D. Kubiak and R.H. Stulen, Surf. Sci. 206, L833 (1988); 237, 35 (1990)

17. Y. Mitsuda, T. Yamoda, T.J. Chuang, H. Seki, R.P. Chin, J.Y. Huang, and Y.R. Shen, Surf. Sci. 257, L633 (1991)

18. Y.L. Yang, L.M. Struck, L.F. Sutcu, and M.P. D'Evelyn, Thin Sol. Films, 225, 203 (1993)

19. R.E. Thomas, R.A. Rudder, and R.J. Markunas, J. Vac. Sci. Technol. A10, 2451 (1992)

20. Y.L. Yang and M.P. D'Evelyn, J. Am. Chem. Soc. 114, 2796 (1992)

21. J.E. Lowther, Solid State. Commun. 56, 243 (1985)

22. X.M. Zheng and P.V. Smith, Surf. Sci. 253, 395 (1991); 256, 1 (1991); 261, 394 (1992)

23. J.F. Morar, F.J. Himpsel, G. Hollinger, J.L. Jordan, and F.R. McFeely, Phys. Rev. B33, 1340 (1986)

24. T. Yamada, T.J. Chuang, H. Seki, and Y. Mitsuda, Mol. Phys. 76, 887 (1991)

25. A.Freedman and C.D. Stinespring, Appl. Phys. Lett. 57, 1194 (1990)

26. S. J. Harris and D.N. Belton, Appl. Phys. Lett. 57, 1194 (1991)

27. C.D. Stinespring, A. Freedman and C.E. Kolb, J. Vac. Sci. and Technol. A4, 1947 (1986)

28. J.F. Moulder, W.F. Stickle, P.E. Sobol, and K.D. Bomben, *Handbook of X-ray Photoelectron Spectroscopy* , Perkin-Elmer Corp., Physical Electronics Division (Eden Prairie, MN 1992)

29. B.B. Pate, M. Oshina, J.A. Silberman, G. Rossi, I. Lindau and W.E. Spicer, J. Vac. Sci. Technol. A2, 957 (1984)

30. I. Palchan, M. Crespin, H. Estrade-Szwarckopf. and B. Rousseau, Chem. Phys. Lett. 157,321 (1989)

31. G.N. Robinson, A. Freedman and R.L. Graham, submitted to J. Phys. Chem.

32. T. Derry, L. Smit, and J.F. van der Veen, Surf. Sci. 167, 502 (1986)

33. V.S. Smentkowski and J.T. Yates, submitted to J. Vac. Sci. Technol.

34. V. Tarnovsky and K. Becker, J. Chem. Phys. 98, 7868 (1993)

35. M.A. Lennon, K.L. Bell, H.B. Gilbody, J.G. Hughes, A.E. Kingston, M.J. Murray, and F.J. Smith, J. Phys. Chem. Ref. Data 17, 1285 (1988)

36. C. Ma, M.R. Bruce, and R.A. Bonham, Phys. Rev. A44, 2921 (1991)

37. M.R. Pederson and W.E. Pickett, Materials Research Society Symp. Proc. 270, 389 (1992)

38. S.J. Harris and D.G. Goodwin, J. Phys. Chem. 97, 23 (1993)

39. M. Zhu, R.H. Hauge, J.L. Margrave, and M.P. D'Evelyn, MRS Symp. Proc. 280 (in press)

40. B.J. Garrison, E.J. Dawnkaski, D. Srivastava, and D.W. Brenner, Science $\underline{255}$, 835 (1992)

41. D. Huang and M. Frenklach, J. Phys. Chem. $\underline{96}$, 1868 (1992)

42. A. Freedman, unpublished results

43. G.N. Robinson, R.E. Continetti, and Y.T. Lee, J. Chem. Phys. $\underline{92}$, 275 (1990)

44. NIST Chemical Kinetics Database (Standard Reference Database 17, Version 4.0), F. Westley, J.T. Herron, R.F. Hampson, and W.G. Mallard, eds. (U.S. Department of Commerce, 1992)

45. S.W. Benson, *Thermochemical Kinetics*, Wiley (New York, 1968)

46. P.C. Weakliem and E.A. Carter, J. Chem. Phys. $\underline{98}$, 737 (1993)
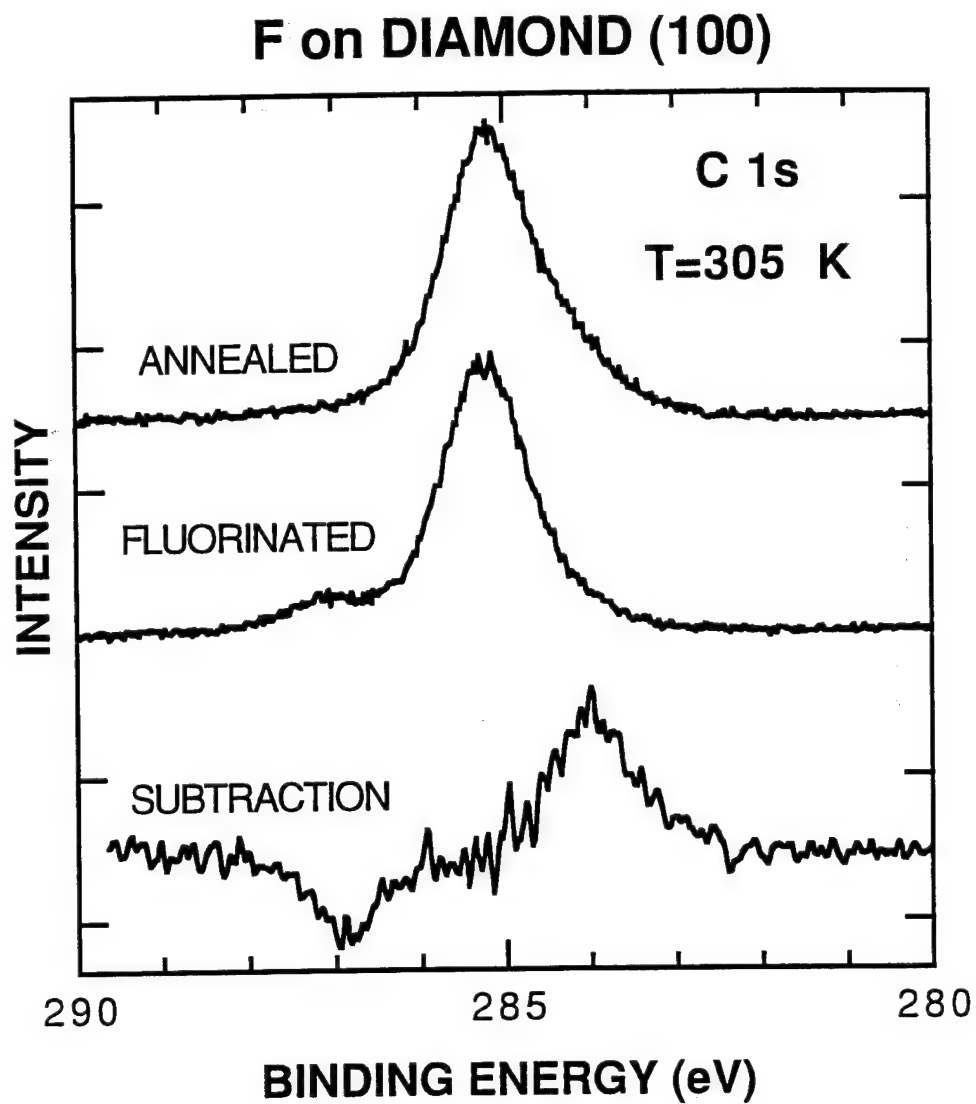
Figure 1. XPS spectra of the C 1s transition of a diamond (100) surface after: (top) annealing at 1200 K; and (middle) exposure to a saturation dosage (40 monolayers) of F atoms . The bottom spectrum represents the remainder after one spectrum has been subtracted from the other, demonstrating the existence of peaks at binding energies lower and higher than the bulk carbon peak due to the annealing and fluorination processes respectively.

17

F ATOMS ON DIAMOND
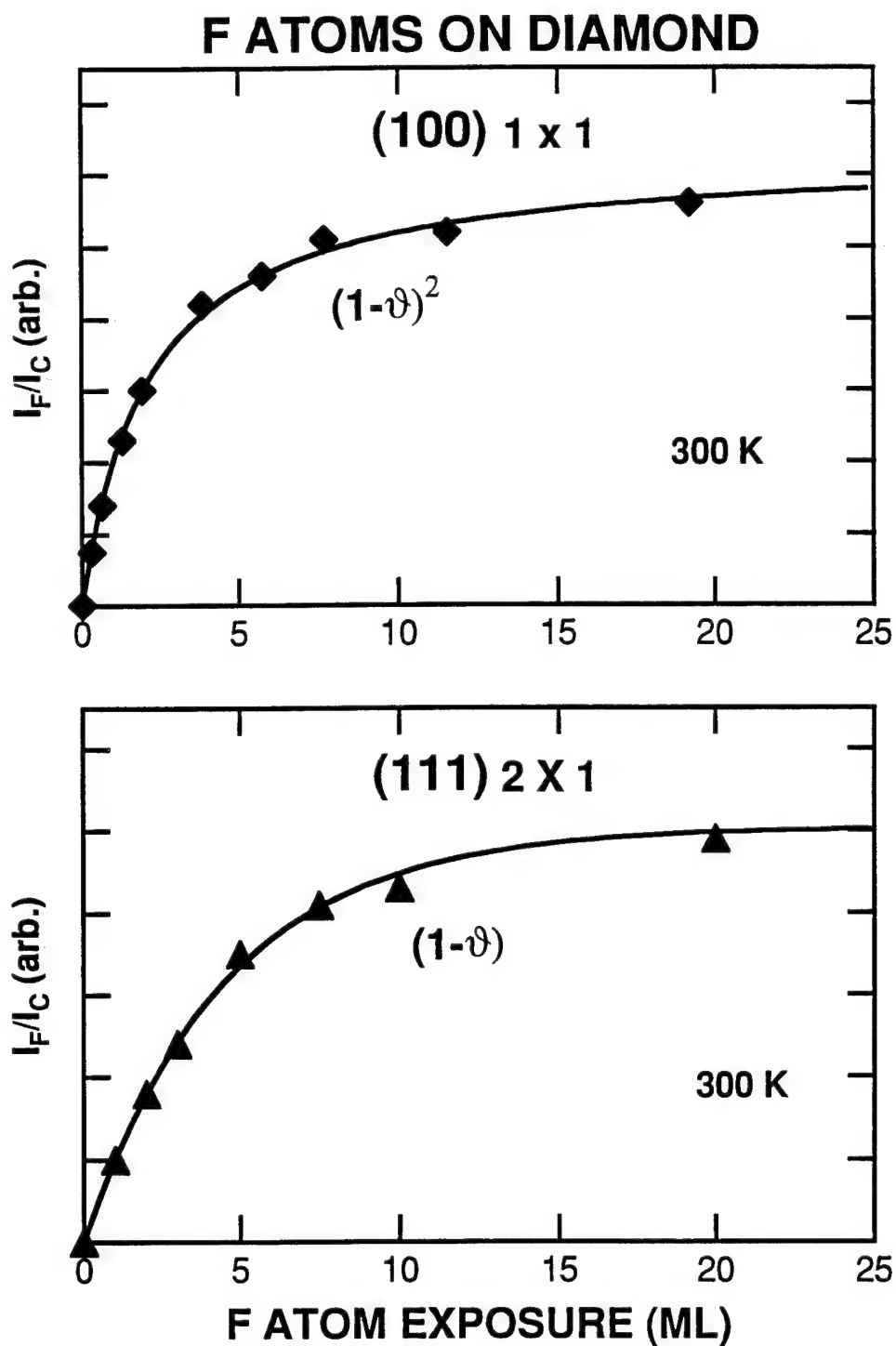
Figure 2. Uptake of fluorine atoms on the (100) and (111) surfaces as a function of F atom exposure at 300 K. (1 ML is the equivalent of one fluorine atom per surface carbon.) The integrated fluorine signal from the XPS F 1s spectra have been normalized to the integrated carbon 1s spectra. The fits to the data (represented by solid curves) assume a model in which the uptake rate of fluorine atoms is proportional to some order to the number of unoccupied sites, $1-\theta$, where θ is the fractional fluorine atom coverage.

18
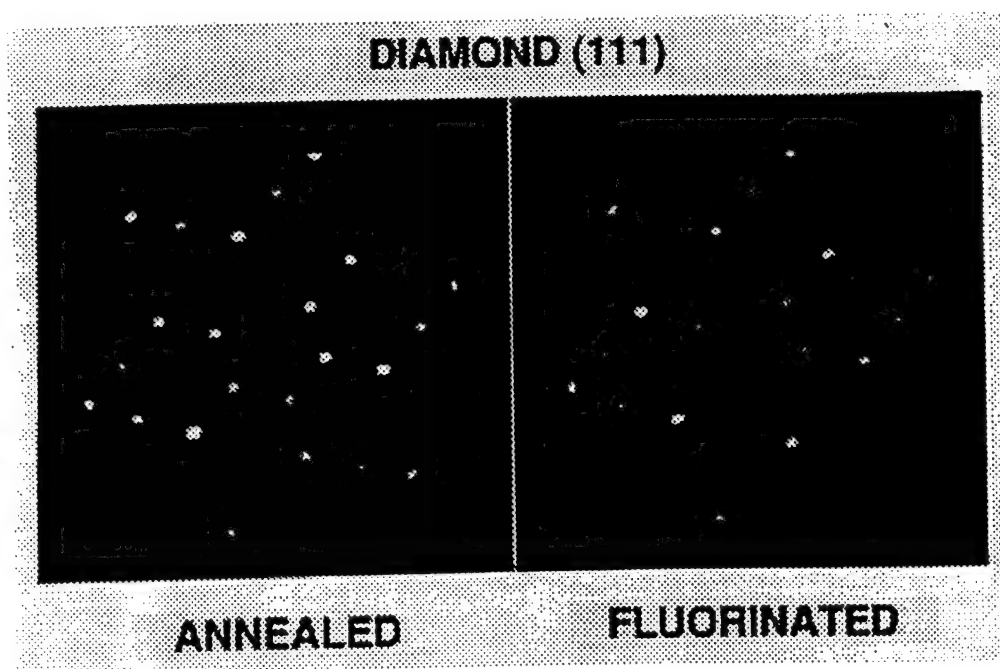
Figure 3. Low energy electron diffraction (LEED) patterns of a diamond (111)-(2x1) surface before and after fluorination. Note the relative decrease in the intensity of the half-order spots on the fluorinated surface. The total atomic fluorine exposure was 40 ML.

FLUORINE ON DIAMOND
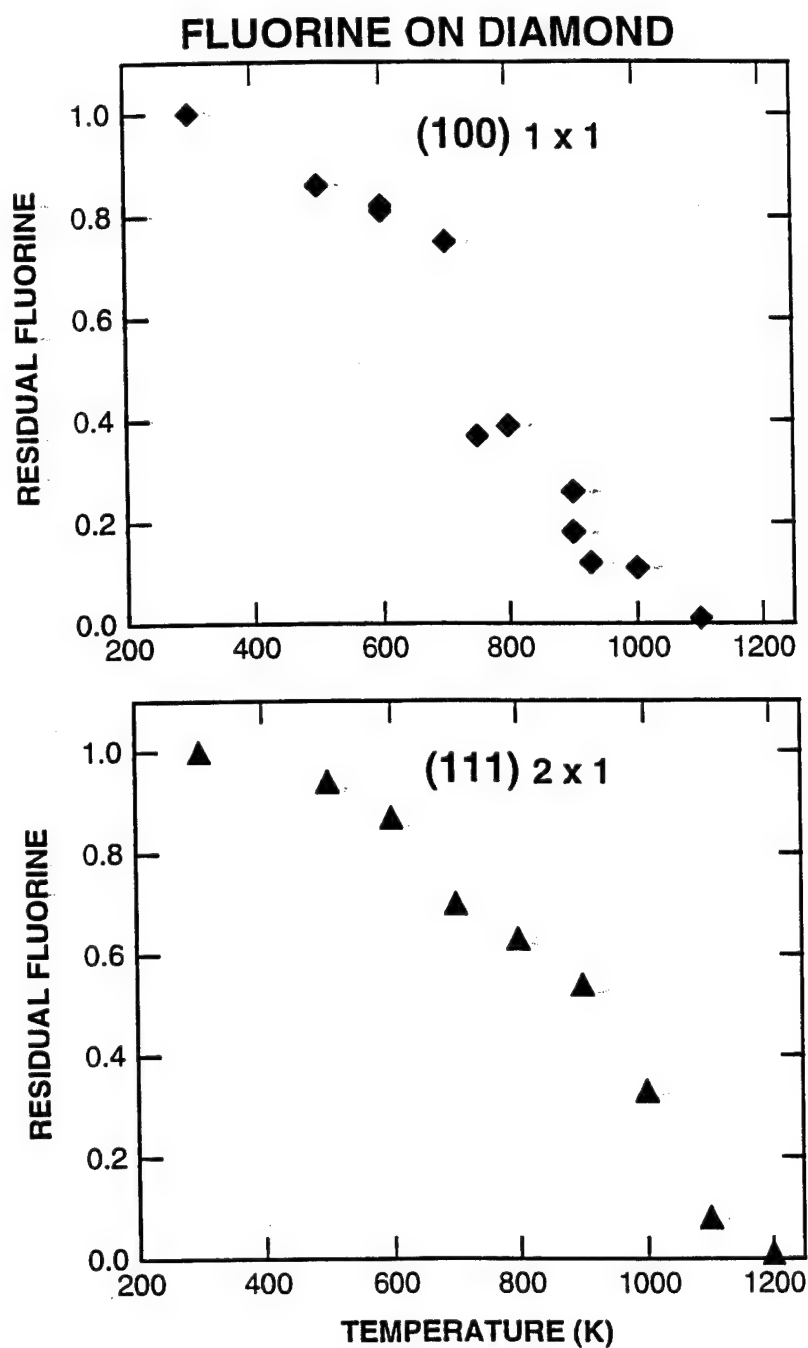
Figure 4. Residual fluorine on the diamond (100) and (111) surfaces as a function of substrate temperature. The substrate was fluorinated to saturation at room temperature before heating.
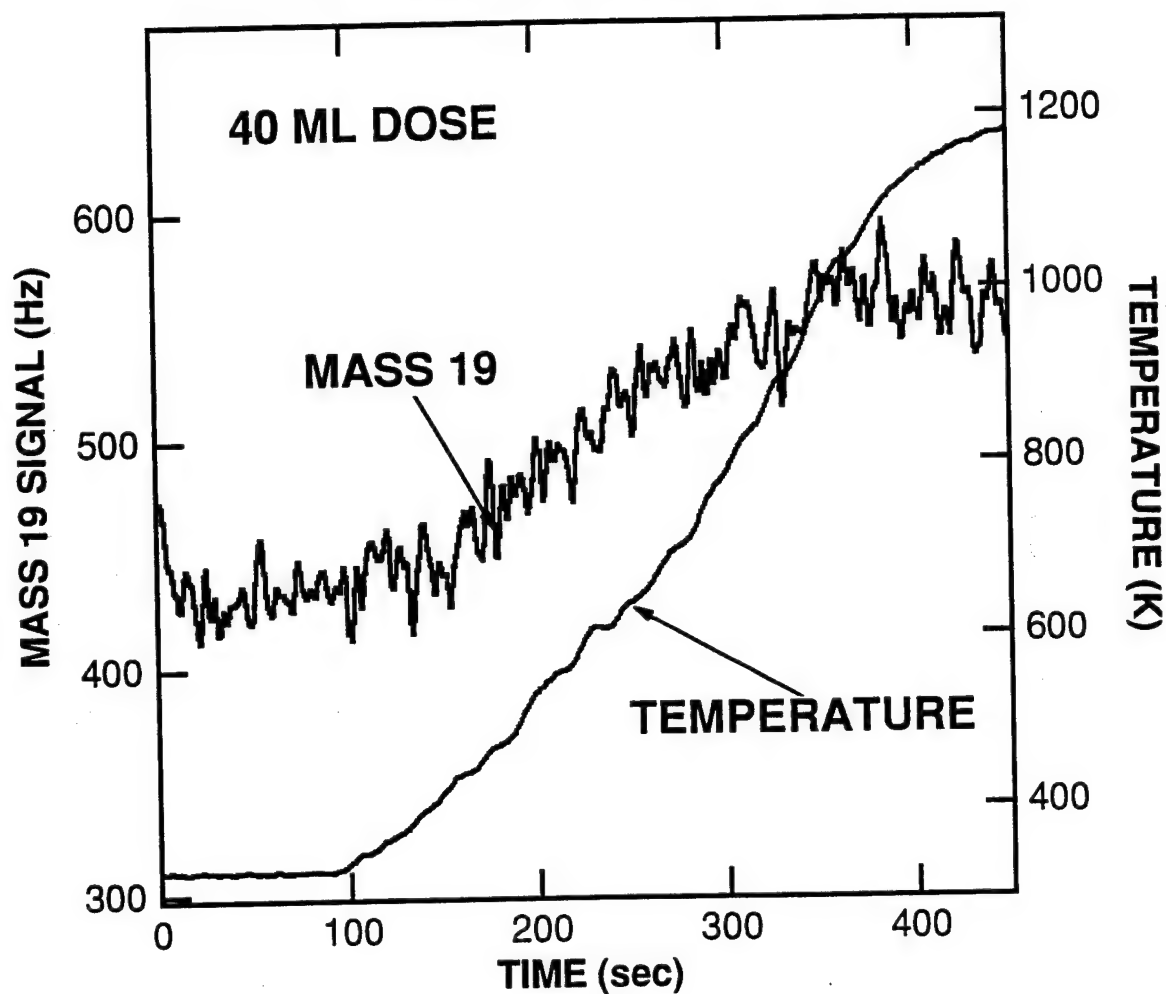
Figure 5. Thermal desorption of a fluorinated (111) diamond surface. The mass spectrometer signal at mass 19 (atomic fluorine) and the substrate temperature as a function of time are displayed.

21

Cl ATOMS ON DIAMOND (100)
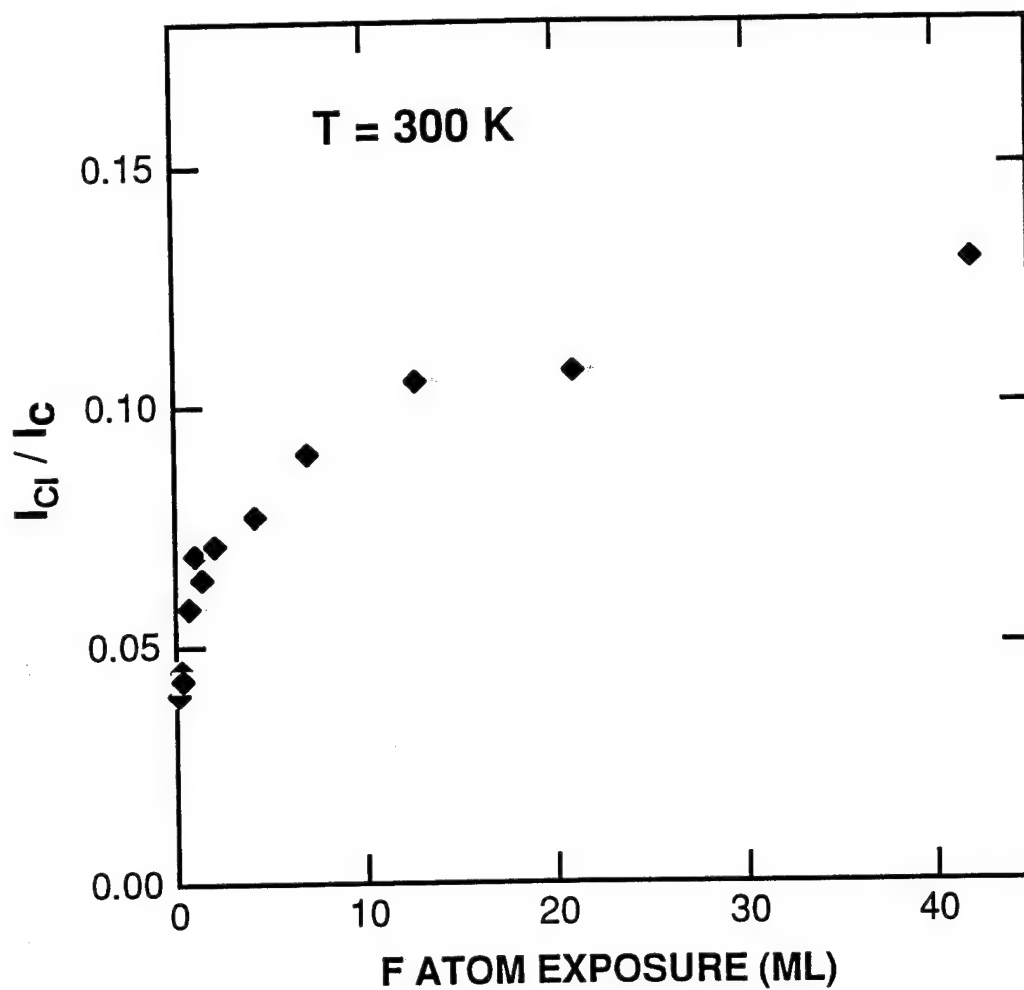
Figure 6. Uptake of chlorine atoms on the diamond (100) surface as a function of Cl atom exposure at 300 K. The integrated chlorine signal from the XPS Cl 2p spectra have been normalized to the integrated carbon 1s spectra.
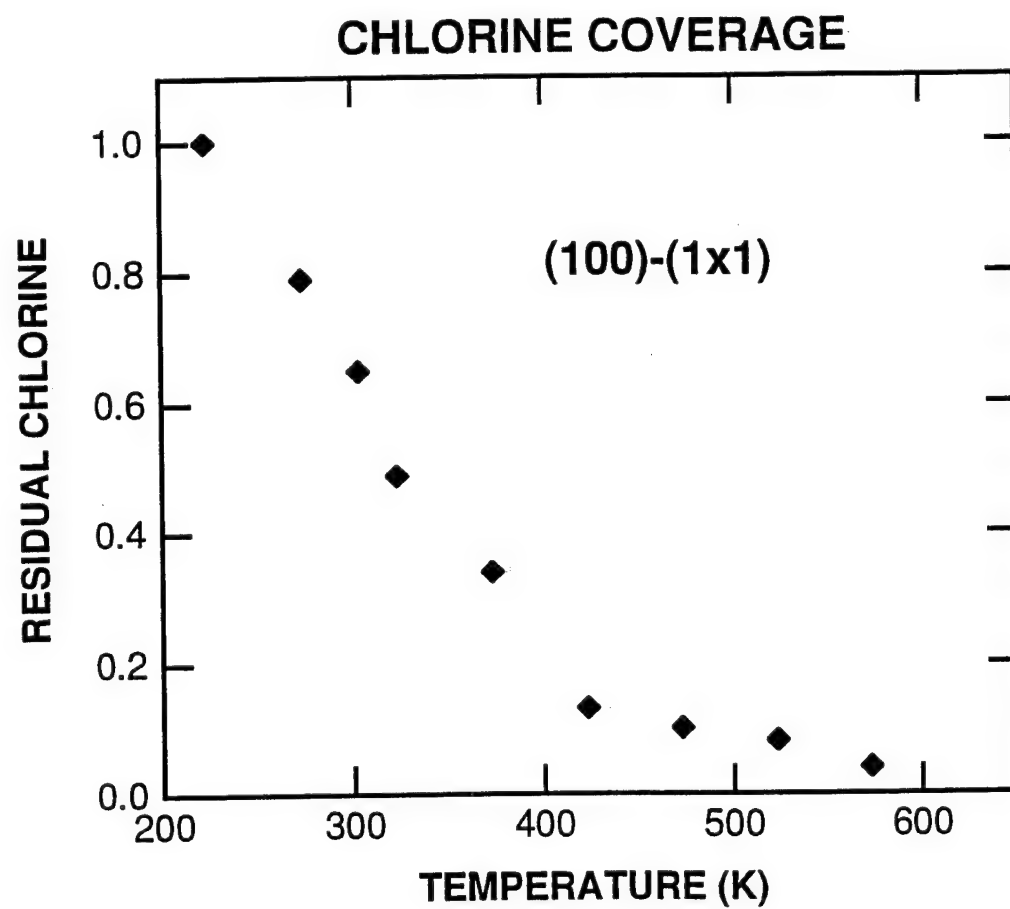
Figure 7. Residual chlorine on a diamond (100) surface as a function of substrate temperature. The substrate was chlorinated to saturation at room temperture before heating.

HALOGENATION OF CARBON SURFACES BY ATOMIC BEAMS: HOPG GRAPHITE

Andrew Freedman
Center for Chemical and Environmental Physics
Aerodyne Research, Inc.
45 Manning Road, Billerica, MA 01821
(508)663-9500, ext. 296
Fax: (508)663-4918
e-mail: af@aerodyne.com

ABSTRACT

Highly oriented pyrolytic graphite (HOPG) surfaces (basal plane) have been exposed to beams of atomic and molecular fluorine and chlorine in an ultrahigh vacuum environment. X-ray photoelectron spectroscopy and low energy electron diffraction techniques have been used to elucidate the chemistry involved. Atomic fluorine adsorption on HOPG graphite produces an ionically bound C-F species. The ordered fluorine adlayer saturates at a coverage of approximately a quarter of a monolayer at 300 K. This adlayer is stable as the surface is heated to 550 K, whereupon it desorbs. No adsorption of either atomic or molecular chlorine or molecular fluorine could be observed. These results are in accord with high pressure data that indicate that graphite etching by fluorine occurs primarily by attack at the edge (prism planes) of graphite.

INTRODUCTION

We have performed a short investigation in an ultrahigh vacuum environment involving the interaction of the basal plane of highly oriented pyrolytic graphite (HOPG) graphite with atomic and molecular fluorine and chlorine. We will present data that indicates that this graphite surface is surprisingly unreactive in view of the high exoergicity of the etching reaction to produce gas phase carbon halide molecules:

$$\text{Graphite} + 4X \rightarrow CX_4 \ \ (X = F, Cl) .$$
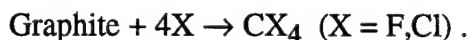
In addition, the chemical reactivity of graphite will be compared to that of diamond; this is instructive in view of the vastly different surface bonding and structure. The graphite basal plane is planar; its extended hexagonal ring structure is held together by carbon-carbon sigma bonding and is stabilized by aromatic π-bonding which extends over the entire surface. Furthermore, its atomic surface density is greater than that of diamond. Diamond bonding is tetrahedral; depending on the surface reconstruction, the surface is terminated with easily broken carbon-carbon bonds or hydrogen atoms. We will present results that indicate that the graphite basal plane is even less reactive than the diamond surfaces previously studied [1,2].

EXPERIMENTAL

Studies were performed in an ultrahigh vacuum apparatus comprising a turbomolecular pumped, liquid nitrogen-trapped ultrahigh vacuum reaction chamber (ultimate vacuum - 3×10^{-10} Torr) interfaced to an ion-pumped analysis chamber. The diagnostics available in the analysis chamber are x-ray photoelectron spectroscopy (XPS) and low energy electron diffraction (LEED); a quadrupole mass spectrometer, which enables identification of the desorption products, is located in another differentially pumped chamber orthogonal to the reaction chamber. The sample is transferred between chambers using a linear motion feedthrough with sample heating (1200 K) and cooling (120 K) capabilities.

The highly oriented pyrolytic graphite (HOPG) samples, intended for use as a monochromator material in x-ray and neutron analysis, were obtained from Union Carbide. It should be noted that these samples are not single crystals, having a mosaic spread of 0.8° (grade ZYB). The sample, cleaved perpendicular to the basal plane, was cleaned in vacuo by heating it to 700 K. Chromel-alumel thermocouples were placed in contact with the substrate holder at both ends of the substrate. A measurable temperature gradient exists across the holder, amounting to 50-75 K at 1200 K; we expect the actual temperature of the graphite sample to be within the range of the thermocouples. The temperatures reported in this paper are the lower of the two thermocouple readings. The LEED pattern produces a hexagonal array of triplets at a beam energy of 70 eV indicating that the basal plane of the graphite was being viewed although multiple edge plane sites are undoubtedly exposed during sample preparation.

The fluorine atom source has been described in detail elsewhere.[3] Briefly, it consists of a miniature fast flow tube whose output is sampled by a small aperture (40 μm), which produces an effusive atomic or molecular beam. A 5% fluorine in argon gas mixture (2 Torr) flows (500 sccm) through an alumina tube which is surrounded by an Evenson-type microwave discharge cavity, past the aperture, and exhausts through a co-annular passage. Operating the discharge at 70 W power produces nearly 100% dissociation of the fluorine. The alumina flow tube is readily passivated and no recombination of F atoms in the gas or on the walls is seen when the beam is sampled by a mass spectrometer. In order to produce chlorine atoms, the source is modified by replacing the alumina tube with a halocarbon wax-coated quartz tube [4]. The coating reduces wall-induced recombination. Chlorine atom recombination is further reduced by replacing the flat aperture plate with a nickel skimmer (Beam Dynamics) with a 140 μm aperture. The skimmer wall thickness is only 30 μm at the aperture, minimizing boundary layer effects. Typical dissociation fractions of 50-75 % are reached when using 5% Cl_2 in Ar gas mixtures.

The XPS analyses were performed using a PHI 15 keV, Mg K_α x-ray source and a PHI 15-255 GAR double pass cylindrical mirror electron energy analyzer operated at a bandpass energy of 25 eV. All spectra presented here are referenced to the C ls peak (284.6 eV binding energy). This peak has a full width at half maximum (FWHM) of 1.4 eV and its assignment is never ambiguous. Fluorine atom concentrations are measured using the F 1s transition at 685.5 eV and chlorine atoms are detected using the Cl 2p transition at ~ 198.5 eV.[5] The LEED diagnostic is of a reverse view variety (Princeton Scientific Instruments).

In a typical experiment, the cleaned graphite sample is exposed to the halogen atom flux for a given amount of time. Dose levels are calculated assuming effusive flow. The chamber pressure is $\approx 10^{-7}$ - 10^{-6} Torr during exposure (primarily argon or helium). After sample exposure, the beam source is pumped out and the reaction chamber evacuated to 10^{-9} Torr. The sample is then transferred to the analysis chamber where XPS and LEED spectra are taken. When surface coverage as a function of substrate temperature is being measured, the sample is heated to a given

temperature for approximately five minutes and then allowed to cool to room temperature before analysis. (The duration of the heating period did not seem to affect the results.)

RESULTS AND DISCUSSION

The carbon 1s XPS spectra of both annealed and halogenated HOPG graphite surfaces which have been exposed to atomic fluorine and chlorine are shown in Figure 1. (Exposure of the HOPG substrates to molecular fluorine and chlorine produced no evidence of any uptake of halogen.) Note that the spectrum of the basal plane that has been exposed to atomic chlorine is identical to that of the annealed sample. Furthermore, only an extremely small quantity (barely above the noise) of chlorine could be measured monitoring the Cl 2p peak. This small quantity of adsorbed chlorine could be entirely the result of the presence of edge planes exposed during the cleaving process; as discussed below, the edge plane of graphite is much more reactive than the basal plane. On the other hand, upon exposure to atomic fluorine, the carbon 1s XPS spectrum of the graphite exhibits a distinct peak, shifted to a binding energy 2.5 eV higher than that found for the bulk peak. The binding energy of this C-F peak is virtually identical to that observed with bulk graphite fluoride intercalation compounds (also known as the ionic form of graphite fluoride)[6]. By integrating the F 1s XPS spectra at 685 eV and comparing the observed intensity to that found with diamond [1], it is determined that the fluorine atom coverage saturates at approximately 1/4 of a monolayer at 300 K, comparable to what is found in an early stage of ionic graphite fluoride formation.[7] A LEED pattern of basically hexagonal symmetry could be obtained from the fluorinated graphite sample, indicating the formation of an ordered adlayer, although the pattern is quite complex due to scattering from multiple domains of the non-single crystal sample.

The residual fluorine on the surface as the substrate is heated as determined using XPS is presented in Figure 2. The adlayer is quite stable until a temperature of 550 K is reached. Given that Rosner and Strakey found a sharp falloff in fluorine induced etching of graphite below 1050 K,[8] it is likely that the fluorine simply desorbs as opposed to etching the graphite to form fluorocarbon radicals. The combination of the desorption data, LEED patterns, and the small saturation coverage at room temperature indicates that the fluorine has not penetrated the graphite lattice. We note that samples of non-aligned graphite substrates fluorinated in various discharge environments have shown evidence of multiply fluorinated surface and bulk carbon. Substrates exposed to the products of low power density RF discharges of nitrogen trifluoride and sulfur hexafluoride at 200 m Torr show evidence of surface difluoride species and monofluorinated bulk species.[9] Studies of exposures to higher power microwave discharges of sulfur hexafluoride at a pressure of 10^{-3} Torr have shown production of thick films of highly fluorinated species.[10] It is possible, if not probable, that the production of ultraviolet photons, ionic species, and /or energetic metastable species in the discharge and substantial exposure of edge planes to fluorinated radicals is responsible for the more vigorous reaction (compared to that observed in the present experiments) of the graphite surface.

27

The comparison of the C 1s XPS spectra presented above to that of the ionic form of graphite fluoride bears more discussion. Graphite fluoride can be prepared in two forms: ionic and covalent.[7] The former is considered to be a fairly stable intercalation compound which is formed by the penetration of fluorine between the graphite planes. The covalent form, formed at high pressures and temperatures, involves a true reaction between the carbon and fluorine atoms. The aromatic nature of the graphite structure is lost and sp^3 bonding results; it can be considered as an infinite cyclohexafluoro-hexane structure. Sato has suggested that the transformation of aromatic to tetrahedral bonding in the formation of covalent graphite fluoride might provide a model for the possible role of hetero-atoms (especially fluorine) in diamond deposition systems.[11] Sato's suggestion was based on the concept that the mechanism for fluorine atom attack on sp^2-bonded carbon on growing diamond surfaces might be similar to that observed on graphite. But, in our experiments, direct attack on a carbon-carbon bond in the graphite substrate was not observed; the carbon 1s XPS spectrum would have shown a much greater binding energy shift as is seen in covalent graphite fluoride. The stabilization effect of both the infinite two-dimensional ring structure of graphite (fluorine addition would induce out-of-plane distortion) and the delocalized π electron cloud (the π-electron stabilization energy in graphite is larger than in any aromatic molecule) is too great to overcome under the conditions of low beam energy and surface temperature encountered in this experiment.

The diamond (111) and (100) surfaces are more reactive towards fluorine atoms than the basal plane of graphite. Fluorine atoms attack both surfaces, breaking carbon-carbon dimer bonds to form a carbon monofluoride moiety. A saturation coverage of three-quarters of a monolayer is observed at 300 K. In addition, fluorine atom desorption is observed over a wide range of temperatures implying a range of carbon-fluorine bond energies. Weakly adsorbed atomic chlorine is observed at much lower coverages. This comparative non-reactivity of the graphite basal plane compared to diamond is also observed in attempts to grow diamond on graphite by CVD techniques. Experiments by Ong, et al.[12], Dubray, et al.[13], and Suzuki and co-workers [14] have shown that diamond nucleates preferentially on the edge planes of graphite. Calculations by Lambrecht et al. [15] support these findings; in addition, they argue that the act of scratching substrate surface provides a better diamond nucleation environment due to the production of graphitic nucleation sites. This large difference in reactivity between basal and edge planes is also observed with both hydrogen and oxygen.[12, 13] The fluorine-carbon species found here is probably a weakly ionic one, involving the delocalized π electron cloud. We also note that the surface density of the graphite basal plane is greater than that of any diamond plane and the C-C bond distances are smaller, imposing severe steric constraints on the formation of multiple carbon-halogen atom bonds.

CONCLUSIONS

We have shown that the basal plane of graphite is nonreactive towards thermal energy beams of atomic chlorine and molecular chlorine and fluorine. Atomic fluorine forms an adlayer

which saturates at a coverage of ~1/4 of a monolayer . This adlayer is stable to a temperature of 550 K whereupon the fluorine desorbs. The observed low reactivity of the graphite basal plane is in accord with high pressure observations involving reaction with fluorine, oxygen, and hydrogen. We ascribe this low reactivity to a combination of stearic and energetic factors which mitigate against the disruption of the infinite two-dimensional ring structure of the basal plane. The edge (prism) plane of graphite, on the other hand, contains dangling bonds which are readily available for reaction. In this respect, it is similar to the diamond (100) and (111) surfaces, which form stable hydrogen, fluorine and oxygen adlayers.

ACKNOWLEDGMENTS

REFERENCES

1. A.Freedman and C.D. Stinespring, Appl. Phys. Lett., 57 (1990) 1194

2. A. Freedman, J. Appl. Phys., 75 (1994) 3112

3. C.D. Stinespring, A. Freedman and C.E. Kolb, J. Vac. Sci. and Technol., A4 (1986) 1947

4. A. Freedman and C.D. Stinespring, J. Phys. Chem., 96 (1992) 2253

5. J.F. Moulder, W.F. Stickle, P.E. Sobol, and K.D. Bomben, *Handbook of X-ray Photoelectron Spectroscopy* , Perkin-Elmer Corp., Physical Electronics Division, Eden Prairie, MN, 1992

6. I. Palchan, M. Crespin, H. Estrade-Szwarckopf. and B. Rousseau, Chem. Phys. Lett., 157 (1989) 321

7. T. Nakajima and N. Watanabe, *Graphite Fluorides and Carbon-Fluorine Compounds*, CRC Press, Boca Raton, 1991

8. D.E.Rosner and J.P. Strakey, J. Phys. Chem., 77 (1973) 690

9. G.D. Merfeld and M.A. Petrich, J. Vac. Sci. Technol., A12 (1994) 365

10. P. Cadman, J.D. Scott, and J.M. Thomas, Carbon, 15 (1977) 75; Surface and Interface Analysis, 1 (1979) 115

11. Y. Sato, in *Japan Reviews in New Diamond*, Japan New Diamond Forum, Tokyo, 1990, p4

12. T.P. Ong, F. Xiong, R.P.H. Chang, and C.W. White, J. Mat. Res., 7 (1992) 2429; Appl. Phys. Lett. 60 (1992) 2083

13. J.J. Dubray, C.G. Pantano and W.A. Yarbrough, J. Appl. Phys., 72 (1992) 3136

14. T. Suzuki, M. Yagi, K. Shibuki and M. Hasemi. Appl. Phys. Lett., 65 (1994) 540

15. W.R.L. Lambrecht, C.H. Lee, B. Segall, J.C. Angus, Z. Lee and M. Sunkara, Nature, 364 (1993) 607.
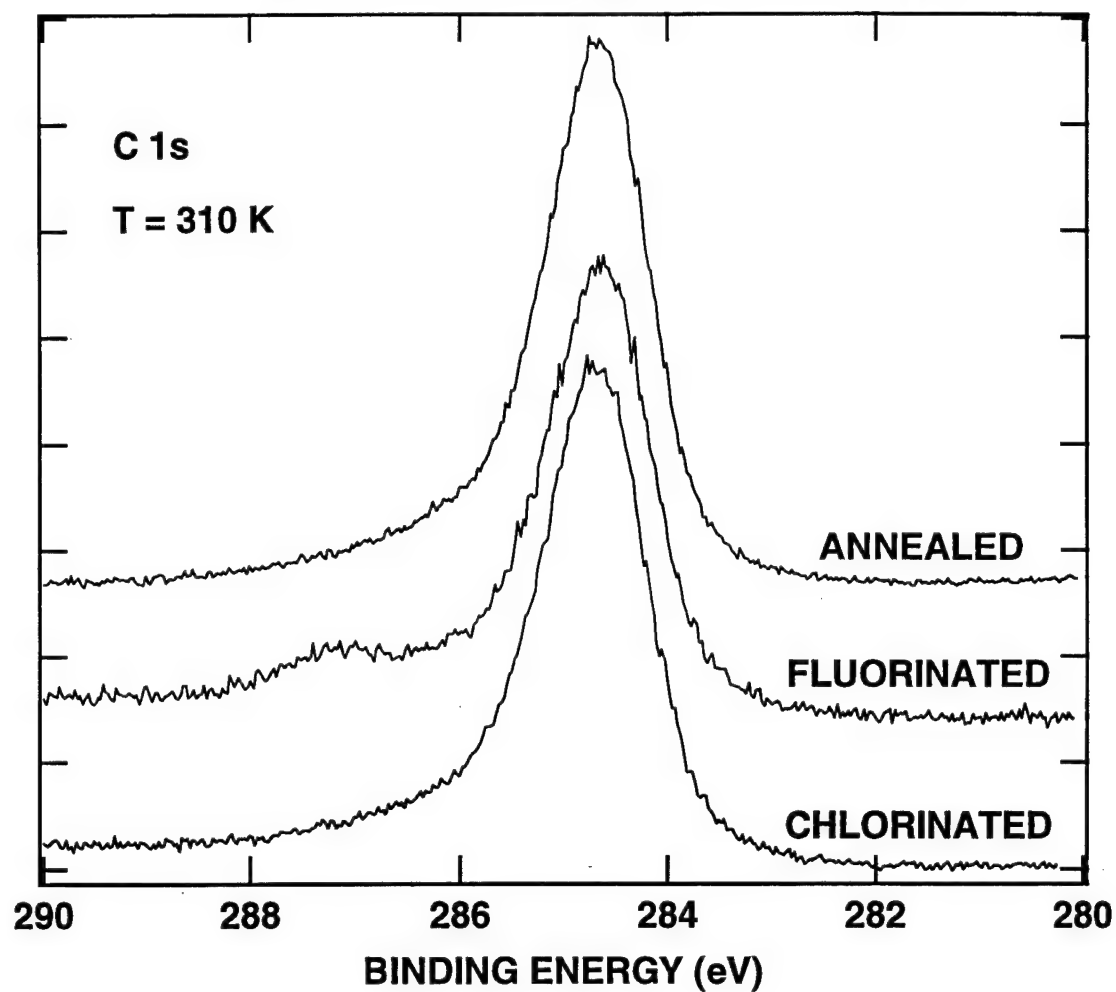
HALOGEN ATOMS ON GRAPHITE

Figure 1. XPS spectra of the C 1s transition for the basal plane of a highly oriented pyrolytic graphite (HOP(sample which has been: (top) annealed at 700 K; (middle) fluorinated to saturation (40 monolayer dose) at 300 K using atomic fluorine; and (bottom) exposed to a 40 monolayer dose of atomic chlorine at 300 K.
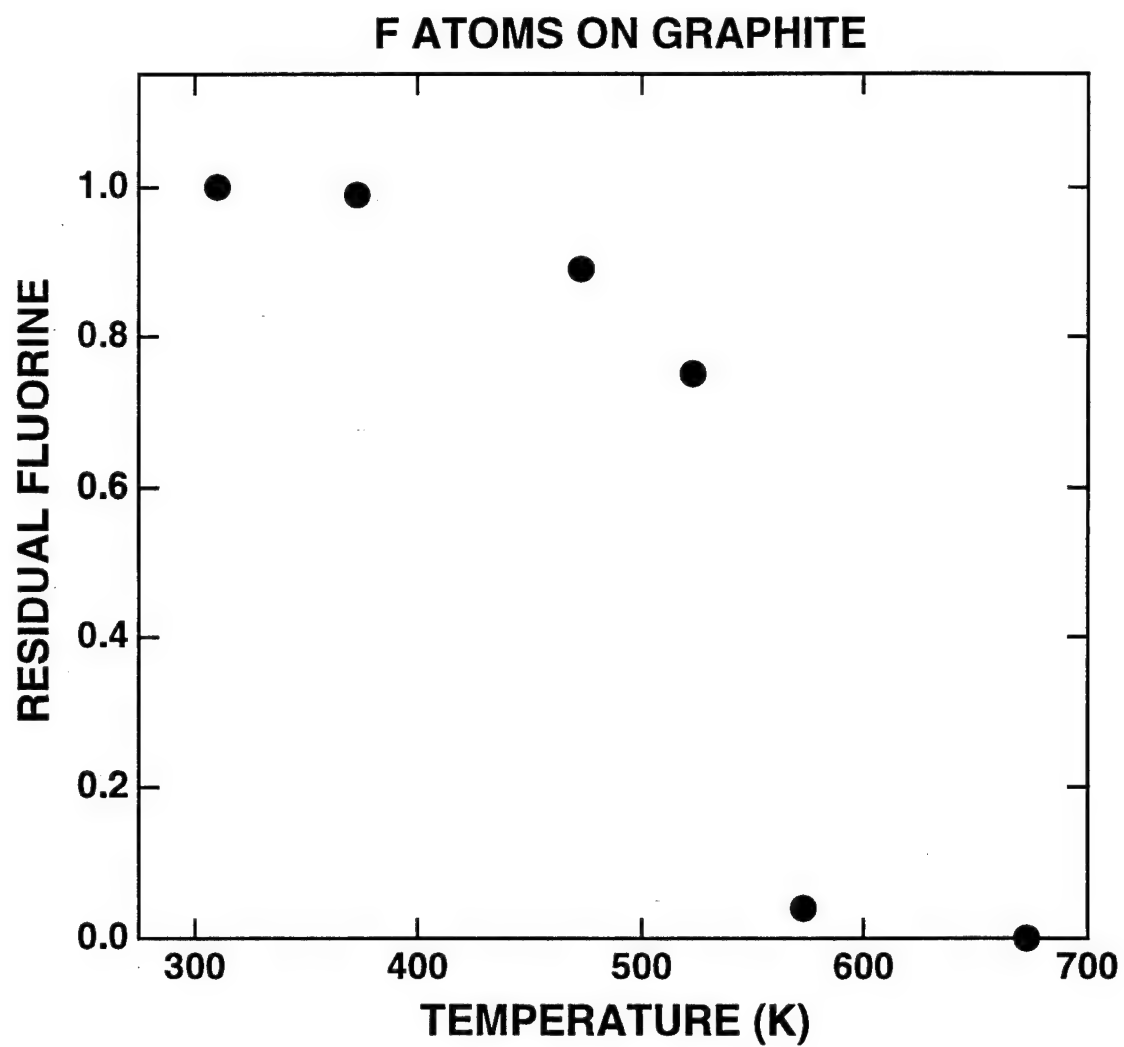
F ATOMS ON GRAPHITE

Figure 2. Residual fluorine on a HOPG graphite surface measured using XPS as a function of substrate temperature. The substrate was fluorinated to saturation at 300 K before heating.

REACTIONS OF FLUORINE ATOMS
WITH SELF-ASSEMBLED MONOLAYERS
OF ALKANETHIOLATES

Gary N. Robinson* and Andrew Freedman
Center for Chemical and Environmental Physics
Aerodyne Research, Inc.
45 Manning Road
Billerica, MA 01821
and
Robert L. Graham
Department of Chemistry
Harvard University
Cambridge, MA 02138

* To whom correspondence should be addressed;

PHONE: (508) 663-9500; FAX: (508) 663-4918; E-MAIL: robinson@aerodyne.com

ABSTRACT

Self-assembled monolayers (SAMs) of methyl- and vinyl-terminated n-alkanethiolates on gold have been exposed at 305 K to beams of atomic fluorine in an ultrahigh vacuum environment. *In situ* x-ray photoelectron spectroscopy of the resulting monolayers indicates that the incoming fluorine atoms penetrate the close-packed chains and react to form mono- and difluorinated methylene groups without fluorination of the gold substrate and with little or no loss of carbon atoms. No reaction was observed with molecular fluorine. After a cumulative dose of ~680 fluorine atoms per carbon chain, approximately seven of the twenty chain carbon atoms have been fluorinated. The fluorination most likely occurs by a mechanism in which an incoming fluorine atom abstracts a chain methylene hydrogen atom creating a radical site for subsequent addition of a fluorine atom. Kinetic modeling of the fluorine atom uptake indicates that the cross sections for hydrogen abstraction and fluorine addition are somewhat smaller than their gas phase counterparts, suggesting that steric crowding limits the overall fluorine atom uptake. No significant differences between the reactivities of the two differently terminated SAMs could be discerned. Our results indicate that C_{20}-alkanethiolate SAMs are effective coatings for preventing oxidation of metallic surfaces by gas phase reactants.

INTRODUCTION

The reactions of gas phase species, such as radicals and ions, with organic films are of considerable importance in such diverse fields as optoelectronic device fabrication,[1] synthesis of carriers for tissue specific drug delivery,[2] corrosion chemistry,[3] and surface analytical chemistry.[4-7] Since the purity as well as the internal and translational energies of gas phase reagents can often be controlled, these reactants should enable much more selective chemical modification of thin films than would be possible in solution. In this paper, we report results recently obtained in our laboratory on the reactions of thermal energy fluorine atoms with one type of thin organic film, self-assembled monolayers of alkanethiolates on gold.

Self-assembled monolayers (SAMs) of chemisorbed n-alkanes are unique among thin organic films in their robustness and high degree of intrinsic order and uniformity. Typical examples of such monolayers are alkylsiloxanes on silicon and alkanethiolates on gold. It is their inherent order that makes SAMs potentially useful materials for, among other applications, nonlinear optical devices. Although numerous experiments have probed the physical and structural properties of SAMs,[8] to our knowledge there have been only a few published studies of the reactions of gas phase reactants with these monolayers. Most of these studies have focused on the reactions of metal atoms,[9] oxygen atoms,[10] and low energy ions.[4-7] Further experiments are needed to elucidate the mechanisms of gas phase radical reactions with such organic films in order to enhance our ability to tailor their chemical and physical properties to suit specific applications.

From a more fundamental perspective, the uniformity and order at the surfaces of SAMs make these monolayers ideal systems for studying the dynamics of radical-adsorbate reactions. Since the spatial orientation of the chains can often be determined from experiments or from theoretical calculations,[11-13] the orientation dependence of the radical-adsorbate reaction cross

section can, in principle, be obtained. In addition, one can ascertain the effect on the reaction cross section of intramolecular energy transfer from the reactive site through the alkane chain.

In the present study, an effusive beam of F atoms was directed at two different types of SAMs consisting of alkanethiolates adsorbed on gold, $Au/S-(CH_2)_{17}CH=CH_2$ and $Au/S-(CH_2)_{19}CH_3$ (see Figure 1 for a schematic representation of the experiment). In order to evaluate the effect of substituents on SAM reactivity, the alkanethiolates had nearly identical chain lengths but different terminal groups. The time dependent uptake of F atoms by the chains at 305 K was monitored using *in situ* x-ray photoelectron spectroscopy (XPS). From these results, we have been able to obtain approximate rate constants for the chain fluorination reactions and insights into the mechanism of radical-SAM reactions.

EXPERIMENTAL

Sample Preparation

The substrates were prepared by vapor depositing ~2000 Å of gold onto silicon (100) wafers pre-coated with ~100 Å of titanium to promote adhesion. Well-ordered self-assembled monolayers were formed by immersing the wafers overnight in solutions of ~1 mM $CH_3(CH_2)_{19}SH$ in oxygen-free ethanol or 0.5 mM $(CH_2=CH(CH_2)_{17}S)_2$ in percolated iso-octane. The synthesis procedures for these compounds are given in ref. 14.

Water and hexadecane contact angles were measured on the SAMs at room temperature and ambient humidity before and after fluorination. A Rame-Hart Model 100 goniometer was used along with a Matrix Technologies electro-pipette for dispensing/removing the liquids onto/from the SAMs (~1 µL/s). Advancing and receding contact angles were measured on both sides of 3 drops of each liquid per sample.[14]

Fluorination

The fluorination experiments were carried out in an ultrahigh vacuum apparatus consisting of a reaction chamber and an analysis chamber. The reaction chamber is pumped by a turbomolecular pump and a liquid nitrogen cooled cryopanel. Atomic fluorine is produced in a microwave discharge plasma source consisting of a miniature alumina flow tube surrounded by an Evenson-type microwave cavity.[15] A mixture of 5% F_2 in helium at 2 Torr flows through the tube; running the discharge at 70 W produces 100% dissociation of the F_2. The output of the tube is sampled by a 40 µm aperture resulting in an effusive F atom beam while the remainder of the gas flows through a co-annular passage and is pumped by a mechanical pump. Assuming the F atom source to be effusive, we calculate a flux of 9 x 10^{13} atoms cm^{-2} s^{-1} at the sample surface. The error in this calculation, including uncertainties in pressure, aperture size, and aperture-substrate distance, is estimated to be ~25%.

The samples were rinsed thoroughly with hexane and ethanol prior to mounting on a linear motion manipulator with heating and cooling capabilities. They were maintained at a temperature of ~320 K under vacuum prior to fluorinating. Fluorine dosing experiments were performed at a

sample temperature of 305 K. The base pressure in the apparatus during these experiments was $\sim 2 \times 10^{-9}$ Torr; the pressure in the reaction chamber with the beam on was $\sim 1 \times 10^{-7}$ Torr.

XPS Analysis

After exposure to a timed dose of F atoms, the samples were transferred under vacuum to the ion-pumped analysis chamber. XPS analysis was performed using a PHI 15 keV Mg Kα x-ray source at a photon energy of 1256.3 eV and a PHI double pass cylindrical mirror energy analyzer operated at a bandpass energy of 50 eV. Spectra were recorded at each level of dosing for the C(1s), F(1s), and Au(4f) transitions. In addition, survey spectra were periodically recorded to check for contamination by water, oxygen, etc. All binding energies are referenced to the Au(4f$_{7/2}$) peak at 84.0 eV. The spectra are fit using a combination of Gaussian and Lorentzian functions.[16] The fractional contribution of the Lorentzian component was held constant for a given element and was in the range of 10-20%. The integrated C(1s) and F(1s) intensities are normalized to the integrated Au(4f$_{7/2}$) signal in order to account for small changes in x-ray flux and the position of the surface in the spectrometer from run to run. The Au(4f$_{7/2}$) signal remained roughly constant during the experiments.

A small amount of x-ray induced photoelectron damage to the monolayer was observed in the form of carbon and fluorine loss. Most of these photoelectrons are produced by the gold substrate but some are likely produced by the aluminum window over the Mg anode. To minimize this damage, the x-ray flux and exposure time were reduced as much as possible within signal-to-noise constraints. The anode power used for the data presented below was 200 W although results obtained with 300 W anode power and longer x-ray exposure times agreed with the 200 W data within 10-20%.
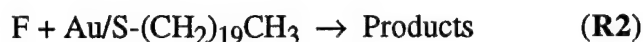
RESULTS AND ANALYSIS

Before reporting results on the reactive uptake of fluorine atoms by alkanethiolate SAMs, a brief description of the likely reaction mechanism is appropriate. More detail on the reaction kinetics will be given in the next subsection. Fluorine atoms react with alkanes at low pressures in the gas phase by first abstracting hydrogen atoms to form HF and alkyl radicals, $F + C_nH_{2n+2} \rightarrow HF + C_nH_{2n+1}$. These abstraction reactions typically have very small activation energies (0 - 2 kcal/mol).[17] Following abstraction, F atoms can add to the alkyl radical to form fluorinated alkanes, $F + C_nH_{2n+1} \rightarrow C_nH_{2n+1}F$. Subsequent abstraction and radical association reactions lead to difluorination of the carbon atoms. Although the F atom + alkyl radical association reaction has no activation energy,[17] it becomes kinetically feasible only when the fluoroalkane adduct can dissipate the ~110 kcal/mol of energy released in forming the carbon-fluorine bond in a time shorter than its unimolecular lifetime. This is possible in the gas phase when *(1)* the pressure is sufficiently high that third body collisions deactivate the energized adduct or *(2)* the reactant molecule has a sufficiently large number of atoms that the unimolecular lifetime of the adduct is longer than its radiative lifetime. It is also possible when the alkane is adsorbed on a solid surface, in which case the reaction exothermicity can be quickly accommodated by the lattice modes of the substrate. A schematic of the likely reaction mechanism is shown in Figure 1.

35

a) Fluorination Results

The reactions of fluorine atoms with monolayers of vinyl- and methyl-terminated alkanethiolates:

$$F + Au/S\text{-}(CH_2)_{17}CH=CH_2 \rightarrow Products \quad (\textbf{R1});$$

and

$$F + Au/S\text{-}(CH_2)_{19}CH_3 \rightarrow Products \quad (\textbf{R2})$$

were monitored using *in situ* x-ray photoelectron spectroscopy. The F(1s) XPS spectra for **R1** at three different F atom exposures are plotted in Figure 2a. The binding energies peak between 686.8 and 687.5 eV depending on the extent of fluorination. No F atom uptake was observed when the room temperature monolayers were exposed to up to 200×10^{15} molecule cm^{-2} of F_2.

C(1s) spectra for **R1** at the same exposures are shown in Figure 2b. Gaussian-Lorentzian fits to the data are also displayed. The main peak at 285.0 eV binding energy in each of the spectra arises from methylene and terminal methyl and vinyl carbon atoms. The peak at ~2.5 eV higher binding energy at an exposure of 30×10^{15} cm^{-2} is due to carbon atoms bonded to single fluorine atoms.[18,19] Given the limited energy resolution of the data and the number of parameters in the fits, the widths of the monofluorinated carbon peaks were fixed when fitting the C(1s) data. At higher exposures, a second peak appears at ~5 eV higher binding energy from carbon atoms bonded to two fluorine atoms.[19] The peak at 285.0 eV is found to broaden towards higher energy with increased F atom exposure. This is likely due to the growth of an additional, unresolved peak from non-fluorinated carbon atoms that are bonded to monofluorinated carbon atoms.[19,20] A similar feature should also appear on the monofluorinated carbon peak from neighboring difluorinated carbon atoms; however, no broadening was detected for these peaks. The XPS spectra recorded for **R2** have similar peak shapes and binding energies. No peak is observed from trifluorinated carbon at ~293 eV.[19] From the carbon detection sensitivity of our spectrometer, if any -CF$_3$ groups are present their coverage must be less than ~75% of a monolayer ($~3.5 \times 10^{14}$ cm^{-2}).

The integrated intensities of the F(1s) spectra normalized to the integrated Au(4f$_{7/2}$) XPS signal at 84.0 eV are plotted on an absolute scale in Figure 3 as a function of F atom exposure for **R1** and **R2**. The Au(4f) signal did not change as a function of exposure. In order to quantify any x-ray induced fluorine loss, F(1s) spectra were recorded and the beginning an end of each XPS analysis run. The circles and diamonds in Figure 4 represent, respectively, the integrated F(1s) data at the start and end of each XPS run for one of the **R1** experiments. Over the 7 - 9 minute x-ray exposure period, 5 - 10% of the fluorine is lost as a result of x-ray induced photoelectron damage.[22,23] Similar results were obtained for **R2**. A series of experiments performed on identical monolayers using 300 W of anode power and longer x-ray exposure times yielded results that agree with those in Figure 3 within 10% at short exposures (0 -100 x 10^{15} cm^{-2}) and within 20% at longer exposures (~300 x 10^{15} cm^{-2}).

36

The F atom uptake per unit area in both experiments is calibrated with reference to the corresponding C(1s) spectra. The integrated C(1s) peak intensities for both reactions are plotted in Figure 5 as a fraction of the total C(1s) signal. The surface coverage of carbon atoms is known from the alkanethiolate coverage (4.6×10^{14} cm^{-2}; the lattice parameters for the vinyl-terminated SAM are unknown but should be similar to those for the methyl-terminated monolayer)[24,25] and the number of carbon atoms per chain. Thus, from the carbon atom coverage we can determine the absolute number of F atoms bonded to the chain carbon atoms from the relative monofluorinated and difluorinated carbon signals, i.e.,

$$(\text{F atoms/cm}^2)_i = R \cdot [\, F(1s) / Au(4f) \,]_i \,,$$

where, R is the ratio of the absolute fluorinated carbon coverage to the relative fluorine signal averaged over all of the data,

$$R = \sum_{i=1}^{n} \left\{ \frac{\left(CF_{rel,\,i} + 2 \cdot CF_{2,\,rel,\,i} \right) \cdot N \cdot 4.6 \times 10^{14}\,\text{cm}^{-2}}{\left[F(1s)_i / Au(4f)_i \right]} \right\} \cdot n^{-1} \,.$$

Here, $CF_{rel,\,i}$ and $CF_{2,\,rel,\,i}$ are the relative mono- and difluorinated carbon XPS signals at each exposure (Figure 5), n is the number of data points, and N is the number of carbon atoms per chain. There is an uncertainty of 10 - 15% in the F atom coverage calculated in this manner as a result of uncertainties in the integrated C(1s), F(1s), and Au(4f) signals.

The calculated F atom coverage will be an upper limit to the true coverage because of the overestimate of the number of carbon atoms that are fluorinated that results from attenuation of the photoelectron signal from sub-surface carbon atoms through inelastic scattering. This overestimate amounts to 1-2 carbon atoms at all exposures. The consequent overestimate in the F atom coverage will decrease with increasing F atom exposure since the relative uncertainty in the number of carbon atoms that are fluorinated will decrease with increasing F atom coverage. We determine this error in the coverage by equating the fractional contribution of each carbon atom to the total C(1s) signal to $[e^{-(d_i / \lambda \sin\theta)} / \sum_i e^{-(d_i / \lambda \sin\theta)}]$ for an all-trans chain configuration (Figure 1). Here λ is the attenuation length, or escape depth, of C(1s) photoelectrons from alkanethiolate SAMs (~30 Å for Mg Kα anode)[26], d_i is the distance from the i-th carbon atom to the top of the SAM, and θ is the angle between the surface normal and the detector (taken to be 45°). The sums of the fractional contributions are compared to the measured values of CF_{rel} and $CF_{2,rel}$ to determine the error in the F atom coverage. This calculation assumes that the attenuation length is not changed as a result of fluorination of the chains. However, as noted above, the Au(4f) XPS signal does not change as a result of fluorination so this is not an unreasonable assumption. The result of this calculation is that the F atom coverages determined from Figure 5 for **R1** and **R2** are ~15% higher than the actual coverage after an exposure of ~315 $\times$ 10^{15} cm^{-2}. (The y-axes in Figures 3 - 5 are not corrected for this uncertainty.) Assuming that the monolayer is fluorinated from the top down and accounting for photoelectron attenuation, approximately seven out of

nineteen carbon atoms are fluorinated in the vinyl-terminated SAM after an exposure of ~315 x 10^{15} cm^{-2} (equivalent to ~680 incident F atoms per carbon chain). Approximately two of those seven are difluorinated assuming that the difluorinated carbon atoms are closest to the vacuum-monolayer interface.

The aforementioned photoelectron attenuation calculation can also be used to justify the assumption of top-down fluorination. Following the same procedure, the relative attenuated C(1s) signal from non-fluorinated carbon atoms, CH$_{rel}$, can be calculated by summing the contributions of the individual carbon atoms, starting from the bottom and moving upward. We find that after summing the contributions of the bottom 12-13 carbon atoms CH$_{rel}$ is ~50%, the experimentally observed limit in Figure 5. Thus, fluorination of the seven topmost carbon atoms yields a calculated value of CH$_{rel}$ that agrees with experiment. This is not a direct proof that the monolayers are fluorinated from the top-down; angle-resolved XPS measurements as a function of F atom exposure would be necessary to conclusively determine this. However, along with the fact that the very reactive F atoms penetrate the SAM from the vacuum-monolayer interface, this calculation supports the assumption of top-down fluorination.

In one of the **R1** (vinyl-terminated SAM) experiments, the F atom exposure was extended to 650 x 10^{15} atoms cm^{-2}. The data indicate that the fluorine uptake levels off above ~300 x 10^{15} atoms cm^{-2} (Figures 3 - 5). Thus, from above, a maximum of ~35% of the chain carbon atoms are fluorinated under thermal beam exposure. Also shown in Figures 3 - 5 are data obtained when a C$_{19}$ vinyl-terminated SAM is exposed to an uninterrupted dose of 660 x 10^{15} atoms cm^{-2} with XPS measurements made only once at the end of the exposure. The F(1s) and C(1s) data are essentially identical to those for the experiment where the monolayer was incrementally exposed to F atoms and probed with XPS at the end of each exposure. Thus, although x-ray induced photoelectrons do cause fluorine loss through C-F bond rupture, the rate of F atom uptake by the resulting carbon centered radicals is sufficiently large that repeated x-ray exposures do not severely distort the overall rate of F atom uptake. It should be noted that fluorine loss most likely occurs at the ends of the chains (vacuum-monolayer interface).[22] Therefore re-fluorination of the x-ray damaged chains should be facile after re-exposure to F atoms.

Our finding that room temperature alkanethiolate SAMs are partly permeable to gas phase fluorine atoms is consistent with other studies that have shown that aqueous ions, metal atoms, and molecules[27-31] penetrate these close-packed monolayers. However, the leveling off of the fluorine uptake at high F atom exposures suggests a kinetic limitation to complete fluorination of the alkanethiolate chains. This is most likely due to increased steric crowding of the methylene hydrogen and carbon atoms located further down the chain.[32] This crowding, which is a result of the increased order in the interior of the SAM relative to its surface[12,33] as well as the presence of F atoms bonded to the chains, makes it difficult for gas phase F atoms to penetrate the layer and to react. Those atoms that do penetrate will be moving more slowly and may lack sufficient translational energy or the proper orientation to overcome the small but finite activation barrier to reaction (see below). Thus, both the concentration of free F atoms and the rate constants for fluorination should decrease with distance down the chain. In this context, it should be noted that

none of the Au(4f) spectra show evidence of Au-F bonding suggesting that F atoms do not penetrate to the gold substrate at the highest exposures in our experiment. These results indicate that C_{20}-alkanethiolate SAMs act as effective barriers to oxidation of metallic surfaces by gas phase reactive species.[29]

Radical induced interchain crosslinking should also be considered as a source of the limited F atom uptake by these monolayers. Crosslinking can reduce the number of F atoms that react with the SAM both by preventing atoms from penetrating the monolayer and by allowing alkyl radicals to react with one another rather than with incoming atoms. An extensive amount of work has been performed on the photodimerization of organic molecules in thin films and crystals.[34-37] In an empirical model proposed by Schmidt,[37] monomers will dimerize if the separation between the reacting carbon atoms in the lattice is no more than 4.2 Å. Although the lattice parameter of methyl-terminated SAMs on gold is 5.0 Å at 35 K,[24,25] the enhanced mobility of the chains at room temperature may allow radicals at the chain termini to approach each other more closely than 4 Å. Sub-surface alkyl radicals may also react with each other, considering that the distance between the n-th carbon atom on one chain and the $(n-1)$-th carbon atom on an adjacent chain is less than 4 Å for all-trans alkanethiolate chains on gold. Nevertheless, we do not expect radical induced crosslinking to be a significant reaction channel in these experiments since the rate of radical + radical association for alkyl radicals on neighboring chains will always be lower than the rate of F atom + radical association because of both the larger concentration of F atoms relative to radicals and the higher rate constant (less negative entropy of activation) for atom + radical reactions.
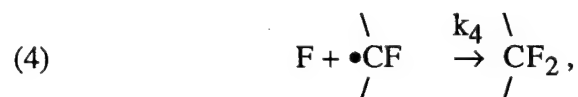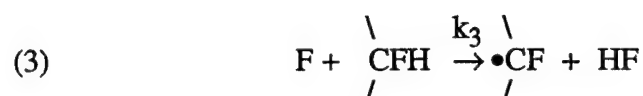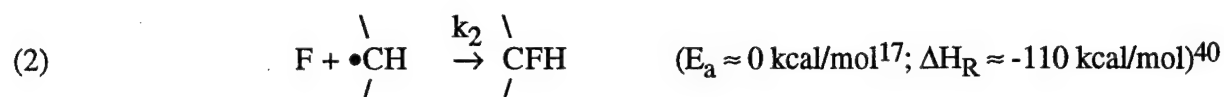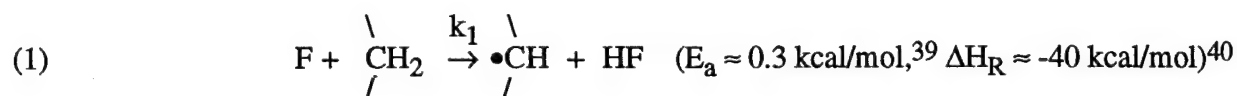
The integrated C(1s) XPS signal normalized to the $Au(4f_{7/2})$ signal for both the $-CH_3$ and $-C_2H_3$ terminated SAMs remains roughly constant with F atom exposure (Figure 6). The near constancy of the carbon signal with exposure indicates that C-C bond scission is not a significant reaction channel after C-F bond formation despite the large exothermicities of the carbon-fluorine bond formation reactions (reactions (2) and (4) below). Thus, stabilization of the incipient C-F bond through intramolecular vibrational energy redistribution is quite efficient. However, uncertainties in our C(ls) XPS data limit the accuracy of the chain length determination to ±1 carbon atom.[38]

The drop in C(1s) signal at low F atom exposures is caused by x-ray induced photoelectrons. Integrated C(1s) intensities for methyl- and vinyl-terminated monolayers that were continuously exposed to x-rays are plotted in Figure 7. These experiments were repeated several times at different x-ray source powers and the drop in C(1s) signal for the methyl terminated monolayer is consistently greater than that for the vinyl terminated monolayer. The reason for this not clear. Interchain cross-linking reactions which might limit electron induced carbon loss are more likely for the vinyl terminated monolayer but such cross-linking would probably affect the rates of F atom uptake and there are no significant differences between the uptake rates for the two monolayers. In any case, we find that once the chain carbon atoms are fluorinated, C-F bonds break more readily as a result of x-ray exposure than C-C bonds.

Contact angle measurements for water and hexadecane were performed on both SAMs before and after fluorination. The wetting results are reported in Table 1. The fluorinated SAMs used in these experiments had been exposed to x-rays from a 300 W anode. As a result of their macroscopic nature, wetting measurements are often difficult to interpret rigorously in terms of molecular level phenomena. However, the similarity between the contact angles for both SAMs after fluorination does suggest that the two fluorinated monolayers have similar surface compositions. The decrease in contact angles after gas phase fluorination in the present experiments reflects an increase in the surface free energies of the monolayers as a result of fluorination. This suggests the presence of polar substituents at the SAM-liquid interface.
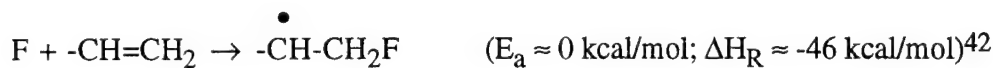
b) Kinetic Modeling

In an effort to model the kinetics of **R1** and **R2**, we have considered the F atom uptake process to follow a mechanism involving four sequential hydrogen atom abstraction and fluorine atom + alkyl radical association reactions:[32]

(1) $\quad$ F + $\overset{\backslash}{\underset{/}{CH_2}}$ $\overset{k_1}{\to}$ $\overset{\backslash}{\underset{/}{\bullet CH}}$ + HF $\quad$ ($E_a \approx 0.3$ kcal/mol,[39] $\Delta H_R \approx -40$ kcal/mol)[40]

(2) $\quad$ F + $\overset{\backslash}{\underset{/}{\bullet CH}}$ $\overset{k_2}{\to}$ $\overset{\backslash}{\underset{/}{CFH}}$ $\quad\quad$ ($E_a \approx 0$ kcal/mol[17]; $\Delta H_R \approx -110$ kcal/mol)[40]

(3) $\quad$ F + $\overset{\backslash}{\underset{/}{CFH}}$ $\overset{k_3}{\to}$ $\overset{\backslash}{\underset{/}{\bullet CF}}$ + HF

(4) $\quad$ F + $\overset{\backslash}{\underset{/}{\bullet CF}}$ $\overset{k_4}{\to}$ $\overset{\backslash}{\underset{/}{CF_2}}$,

where $\overset{\backslash}{\underset{/}{CH_2}}$ represents a chain methylene group, k_i is rate constant for reaction i, and E_a and ΔH_R are the gas phase activation energies and heats of reaction respectively.[41] Note that the 110 kcal/mol exothermicity of the F atom + radical association reactions is sufficient to break either a C-H (~100 kcal/mol) or a C-C (~90 kcal/mol) bond.[40]

F atoms can react with vinyl-terminated SAMs by either abstracting methylene or vinyl H atoms or by adding to the terminal double bond:

$$F + \text{-CH=CH}_2 \rightarrow \overset{\bullet}{\text{-CH-CH}_2F} \qquad (E_a \approx 0 \text{ kcal/mol}; \Delta H_R \approx -46 \text{ kcal/mol})[42]$$

The resulting energized fluoroalkyl radicals can either be stabilized via intramolecular energy transfer or can emit a hydrogen atom to form a vinyl fluoride group, i.e.,

$$\overset{\bullet}{\text{-CH-CH}_2F} \rightarrow \text{-CH=CFH} + H \qquad (\Delta H_R \approx 35 \text{ kcal/mol})[42]$$
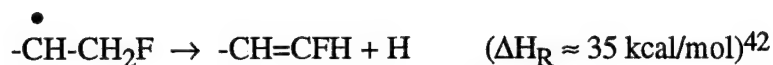
To simplify the modeling of the observed F atom uptake, we ignored the differences between the two different terminal groups and treated both as if they were methylene groups. This is a fair approximation in the case of the methyl-terminated SAM since the rate constants for F atom abstraction of primary and secondary H atoms from linear alkanes differ by only ~10%.[38] As far as the vinyl-terminated SAMs are concerned, however, the rate constants for F atom abstraction of olefinic H atoms and for F atom addition to double bonds are 10 - 20 times higher than the the rate constant for F atom abstraction of a methylene H atom.[43] Nonetheless, for both monolayers the observed uptake will be dominated by reactions with the more numerous chain methylene groups. Differences between the reactivities of the two terminal groups should show up at low F atom exposures if at all.

The observed F atom uptake kinetics were assumed to be pseudo-first order with respect to methylene coverage:

$$\frac{d[\overset{\bullet}{\text{-CH-}}]}{dt} = \sigma_1 \, [\text{-CH}_2\text{-}] \cdot J(F) \qquad \text{(E.1)};$$

$$\frac{d[\text{-CFH-}]}{dt} = \sigma_2 \, [\overset{\bullet}{\text{-CH-}}] \cdot J(F) \qquad \text{(E.2)};$$

where [X] is the coverage of X in cm^{-2}, σ_i is a reaction cross section with units of cm^2, and $J(F)$ is the F atom flux in units of $cm^{-2}s^{-1}$. The assumption of pseudo-first order kinetics is valid since the experiments were carried out with a constant flux of F atoms. As noted in the previous section, the F atom flux is 9×10^{13} $cm^{-2}s^{-1}$ at the surface (with an uncertainty of ~±25%).

Since our results suggest that the fluorination rate constants decrease with distance down the chain, it would be necessary to calculate about 80 cross sections for R1 and R2 (four per methylene group) in order to model the kinetics of this system properly. This is not feasible in the absence of some *a priori* means of determining how the cross sections change with distance down the chain. In order to simplify matters, we have (*1*) focused on modeling the two monofluorination reactions only and (2) assumed a set of two average cross sections for these

reactions. An advantage of this approach is that since reactions (1) and (2) are consecutive first order reactions, there exists an analytical solution to the differential equations representing the rate of appearance of -CFH-:[44]

$$[\text{-CFH-}] = [\text{-CH}_2\text{-}]_0 \cdot \{1 - \frac{\sigma_2}{\sigma_2 \text{-} \sigma_1} \exp(-\sigma_1 \cdot J(F) \cdot t) + \frac{\sigma_1}{\sigma_2 \text{-} \sigma_1} \exp(-\sigma_2 \cdot J(F) \cdot t)\} \qquad \text{(E.3)}.$$

Thus, one can obtain the monofluorination cross sections, σ_1 and σ_2, and an effective initial -CH$_2$-coverage, $[\text{-CH}_2\text{-}]_0$, from a non-linear least squares fit of the data using E.3. $[\text{-CH}_2\text{-}]_0$ represents the coverage of methylene groups available for monofluorination. This approach makes the incorrect assumption that all of these methylene groups are equally reactive. However, limiting the reactant coverage greatly simplifies modeling the limited uptake of fluorine by the monolayer. The resulting cross sections represent, in a general sense, the average reactivity of the available methylene groups.

A property of the solution to E.3 is that transposing the values of σ_1 and σ_2 has no effect on the time dependence of $[\text{-CFH-}]$. Thus, in cases where the values of σ_1 and σ_2 differ from one another, one must rely on kinetic data for analogous gas phase reactions in order to determine which of the calculated cross sections is k_1 and which is k_2. In the gas phase at room temperature, hydrogen abstraction reactions generally have smaller rate constants than atom + radical association reactions in the high pressure limit (see next section).

The optimum non-linear least squares fits to the fluorine uptake data for **R1** and **R2** obtained using E.3 are plotted in Figure 8. The plotted data represent the monofluorination reaction only; above an exposure of ~30 x 10^{15} cm^{-2}, where difluorination starts, the data are obtained from the relative monofluorinated carbon signal (Figure 5). As the inset figures show, the data comprise at least two exponentials. For **R1**, the best-fit parameters are $\sigma_1 = 0.27$ Å^2 and $\sigma_2 = 1.8$ Å^2 per methylene group and $[\text{-CH}_2\text{-}]_0 = 2.9$ x 10^{15} cm^{-2}.[45] Acceptable fits are obtained for $\sigma_1 = 0.25 - 0.30$ Å^2, $\sigma_2 = 1.3 - 2.5$ Å^2. These uncertainties were determined by inspecting the quality of the fits and comparing χ^2 values. As E.3 demonstrates, when σ_1 is lowered σ_2 must be raised to maintain the quality of the fit. For **R2**, the best-fit parameters are $\sigma_1 = 0.20$ Å^2 and $\sigma_2 = 1.0$ Å^2 per methylene group and $[\text{-CH}_2\text{-}]_0 = 3.1$ x 10^{15} cm^{-2}. Acceptable fits are obtained for $\sigma_1 = 0.17 - 0.24$ Å^2, $\sigma_2 = 0.6 - 1.9$ Å^2. Note that the photoelectron induced carbon loss observed for **R2** at low exposures (Figure 6) will introduce a small error in the calculated cross sections since the fluorine signal will be smaller at low exposures than it would have been without the carbon loss. Also, as discussed above, the F atom coverage is overestimated when it is calculated directly from the relative C(1s) signals in Figure 5. The magnitude of this overestimate depends on the extent of fluorination and will therefore introduce an error into the cross section calculations. We estimate this error to be on the order of 10-30%. An additional source of error in these calculations is the ~±25% uncertainty in the F atom flux.

Although the kinetic modeling suggests that the cross sections for **R1** are greater than those for **R2**, the experimental uncertainties are sufficiently large that differences observed between the

42

calculated rate parameters for the two reactions are not likely to be significant. This is not unexpected since, as suggested above, the uptake of fluorine is dominated by reactions with the more numerous chain methylene groups. Therefore, we are unable to determine conclusively the relative reactivities of the terminal methyl and vinyl groups at 305 K.

DISCUSSION

Summarizing our results, our data clearly show that F atoms penetrate alkanethiolate SAMs at room temperature to partially fluorinate the chain methylene groups. However, the uptake of fluorine appears to be subject to kinetic constraints which are steric in origin. The uptake mechanism most likely involves sequential H atom abstraction and F atom-alkyl radical association reactions. Cross sections for H atom abstraction and F atom + alkyl radical association for the two SAMs have been obtained from kinetic modeling of the F atom uptake data. No evidence of F atom induced C-C bond scission was observed and no significant differences between the reactivities of the two SAMS were found. In the following sections, we discuss the significance of the rate constants extracted from our model calculations and draw some conclusions regarding the chemical composition of the SAM surface after beam fluorination.

a) Fluorination Kinetics

The fluorination rate constants obtained from our model calculations are somewhat smaller than those for comparable gas phase reactions. For example, the hydrogen abstraction reaction $F + C_3H_8 \rightarrow n\text{-}C_3H_7 + HF$ has a rate constant of 7.26×10^{-12} cm^3 molecule^{-1} s^{-1} between 213 and 293 K.[39] Assuming a relative reactant velocity of 5×10^4 cm/s, this rate constant is equivalent to a cross section of 1.5 Å^2 ($k = \sigma/v$, where v = relative reactant velocity). The rate constant for the reaction $F + C_3H_8 \rightarrow i\text{-}C_3H_7 + HF$ in the same temperature range is 8.52×10^{-12} cm^3 molecule^{-1} s^{-1}, equivalent to a cross section of 1.7 Å^2 at the same relative velocity.[39] Fluorine atom reactions with longer alkanes have comparable rate constants. The cross section that we obtain for hydrogen abstraction from the SAMs, σ_1, is about six times smaller than the gas phase cross section. We attribute this decrease to steric crowding of the chain hydrogen atoms in the SAM which lessens the probability that incoming F atoms will have the proper orientation for reaction.

There appear not to be any data on the gas phase kinetics of F atom + alkyl radical association reactions. The rate constants for other atom + radical association reactions span a wide range of values. The reaction $Cl + C_2H_5 \rightarrow C_2H_5Cl$ has a high pressure rate constant of 4.55×10^{-10} cm^3 molecule^{-1} s^{-1} in the temperature range 298 - 423 K.[46] This is equivalent to a cross section of 91 Å^2 for a relative velocity of 5×10^4 cm/s. In the high pressure limit where the adduct molecule is stabilized by collisions with the bath gas, the reactions $H + C_2H_5 \rightarrow C_2H_6$ and $H + i\text{-}C_3H_7 \rightarrow C_3H_8$ have room temperature rate constants (cross sections) of 6.0×10^{-11} cm^3 molecule^{-1} s^{-1} (12 Å^2)[47] and 2.5×10^{-10} cm^3 molecule^{-1} s^{-1} (50 Å^2)[48] respectively.

As in the case of hydrogen abstraction, the smaller value of the atom-radical association cross section on the surface, σ_2, relative to the gas phase is probably due, in part, to steric effects. However, it may also result partly from a competition between stabilization of the newly formed C-F bond through vibrational energy redistribution and C-F bond fission. Thus, it is possible that the energy in the newly formed C-F bond may not be dissipated as quickly as it might as a result of collisions at high pressure in the gas phase and there is a higher probability that the F atom is re-emitted.

b) Surface Composition

As noted in the Introduction, one of the practical goals of this research was to develop techniques for the selective modification of SAM surfaces. As such, we would like to determine the chemical composition of the SAM surface that results from beam fluorination. Our XPS results indicate that ~2 of the 19 or 20 chain carbon atoms are difluorinated after an exposure of ~300 x 10^{15} atoms cm^{-2}. Since fluorination most likely proceeds downward from the top of the monolayer, we would conclude from the XPS results that most of the chains are -CF$_2$H or =CF$_2$ terminated. We have no XPS evidence for trifluorinated carbon; from the carbon detection sensitivity of our spectrometer, if any -CF$_3$ groups are present their coverage must be less than ~75% of a monolayer. The absence of observable -CF$_3$ may be due in part to x-ray induced C-F bond breakage at the terminal carbon atom; however, only 5-10% of the C-F bonds are broken as a result of x-ray exposure during an analysis run.

Our wetting results (Table 1) indicate that water and hexadecane (HD) advancing contact angles (θ_a) decrease as a result of beam fluorination. This decrease is correlated with an increase in the surface free energies.[49] There have been a number of studies on the influence of terminal and chain substituents on contact angles.[8] Work by Bain et al.[14] has shown that the θ_a(H$_2$O) and θ_a(HD) on alkanethiolate SAMs terminated with polar groups are considerably smaller than those on methyl-terminated SAMs (e.g., θ_a(H$_2$O) = 83° and θ_a(HD) = 0° for both CH$_2$Cl- and CH$_2$Br-terminated SAMs whereas θ_a(H$_2$O) = 116° and θ_a(HD) = 51° for a CH$_3$-terminated SAM (Table 1). In fact, HD was found to wet any surface containing polar terminal groups. In the present experiments, the low values of θ_a(H$_2$O) and θ_a(HD) observed as a result of fluorination are therefore consistent with the presence of polar fluorinated groups at the liquid-monolayer interface.

Ideally, the surface functional groups on the beam-fluorinated SAMs could be identified by comparing our measured contact angles with those for SAMs synthesized with different numbers of terminal F atoms. Unfortunately, it is very difficult to synthesize alkanethiols having monofluoromethyl or difluoromethyl terminal groups. On the basis of the HD contact angles, however, we can rule out the presence of an appreciable amount of -CF$_3$ at the surfaces of the beam-fluorinated monolayers. Unlike θ_a(HD) on the beam-fluorinated monolayers, θ_a(HD) on a CF$_3$-terminated SAM (Table 1) is considerably larger than θ_a(HD) on Au/S-(CH$_2$)$_{19}$CH$_3$ and Au/S-(CH$_2$)$_{17}$CH=CH$_2$. Similar results were obtained by Shafrin and Zisman for the contact angle of HD on stearic acid and trifluorostearic acid monolayers on platinum.[50]

Graham[51] has synthesized and obtained wetting data for a series of alkanethiolate SAMs whose methyl amide-terminal groups have been progressively fluorinated (Table 1). The trend in θ_a(HD) with increasing fluorination of the terminal methyl group is instructive. θ_a(HD) decreases dramatically when one fluorine atom is bonded to this group and then increases beyond the value for the nonfluorinated SAM when two F atoms are bonded. Zisman and co-workers also found that θ(HD) on a CF_2H-terminated monolayer is larger than θ(HD) on a CH_3-terminated monolayer.[52] In addition, Ellison and Zisman[53] showed that θ(HD) on the fluorinated polymers polytrifluorethylene (CF_3-CH_2-), polyvinylidene fluoride (-CF_2-CH_2-), and polyvinyl fluoride (-$CFH-CH_2$-) are 37°, 24°, and 0° respectively. Based on these observations, our value of θ_a(HD) ≈ 10° for both beam-fluorinated SAMs seems to be consistent with the presence of monofluoro groups at the liquid-monolayer interface in our systems.

When comparing our wetting results to those for "pristine" monolayers, it is important to realize that penetration of fluorine atoms into the SAMs will undoubtedly induce some disorder by causing the chains to spread apart. (Fluorinated alkanethiolates pack less densely on gold that unsubstituted alkanethiolates.)[54] In addition, electrostatic repulsion between adjacent terminal fluorinated alkyl groups will contribute to disorder near the surface of the monolayer.[55] Thus, the HD contact angles observed on our fluorinated SAMs may be influenced by contact between the liquid and -CF- groups below the chain termini that are exposed as a result of disorder near the surface. These polar groups would tend to raise the surface free energy of the SAMs and reduce θ_a(HD). In the case of water, hydrogen bonding interactions with exposed polar groups will tend to decrease θ_a(H_2O).[52] In addition, because of its small size, water can penetrate and interact with sub-surface polar groups.[56] Thus, the surfaces of the beam-fluorinated SAMs, as probed by wetting measurements, may be composed of fluorinated terminal and sub-terminal carbon atoms.

No wetting measurements were made on beam-fluorinated SAMs that were not exposed to x-rays. X-ray photoelectron induced C-F bond cleavage creates radicals which can then react with oxygen, water, and contaminants in the air when the SAMs are removed from vacuum. These adsorbed impurities can change the surface free energy of the monolayers. However, the effects of x-ray induced damage on the wetting results should be minimal since only ~10% of the C-F bonds are broken as a result of x-ray exposure during an analysis run.

The XPS and wetting measurements indicate the presence of -CF_2- and -CF- groups at the surfaces of the beam-fluorinated monolayers. Surface disorder may influence the measured contact angles by exposing polar groups below the chain termini to the wetting liquid. Infrared reflectance absorption and angle-resolved XPS measurements would help to quantify the degree of disorder in these monolayers.

CONCLUSIONS

The most striking result of the present studies is the limited uptake of fluorine atoms observed for the two alkanethiolate SAMs at room temperature. The leveling off of the F atom uptake after an exposure of ~3 x 10^{17} atoms cm^{-2}, where only about 7 of the 19 or 20 carbon atoms per chain are fluorinated, indicates that there is a kinetic constraint to complete fluorination

of the monolayer. This constraint is probably steric in nature, arising from the close-packing of the chains and worsened by the additional crowding that results from F atom penetration and reaction with chain methylene groups. From our results we can conclude that C_{20}-alkanethiolate SAMs are effective coatings for inhibiting gas phase oxidation of metallic surfaces.

No significant differences were apparent between the rates of F atom uptake for methyl- and vinyl-terminated monolayers. In addition, C-C bond scission seems not to be an important product channel for these reactions. Kinetic modeling of the reactions responsible for F atom uptake by the SAMs has yielded approximate cross sections for the H atom abstraction and F atom + alkyl radical association reactions that are significantly smaller than those for comparable gas phase reactions. Steric blocking of the chain carbon atoms is likely responsible for the lowering of these cross sections.

The XPS and wetting measurements on the beam-fluorinated SAMs are consistent with the presence of polar $-CF_2-$ and $-CF-$ groups at the SAM surface. The wetting results may also reflect disorder near the surface of the monolayer. The degree of disorder in the fluorinated monolayers cannot be definitively determined with the techniques used in the present studies. Infrared reflection-absorption and angle-resolved XPS measurements would help to address these issues.

ACKNOWLEDGEMENTS

REFERENCES

1. See, for example: *Metallization of Polymers*; Sacher, E.; Pireaux, J.J.; Kowalczyk, S.P., Eds.; ACS Symposium Series; American Chemical Society: Washington, DC, **1990**; Vol. 440.

2. Müller, R.H. *Colloidal Carriers for Controlled Drug Delivery and Targeting*; CRC Press: Boca Raton, FL, **1991**; p 36.

3. (a) Bregman, J.I. *Corrosion Inhibitors*, Macmillan: New York, **1963**, p 191;

   (b) Barton, K. *Protection Against Atmospheric Corrosion*, Wiley: London, **1976**, p 106.

4. Winger, B.E.; Julian, R.K., Jr.; Cooks, R.G.; Chidsey, C.E.D. *J. Am. Chem. Soc.* **1991**, *113*, 8967.

5. Wysocki, V.H.; Jones, J.L.; Ding, J.-M. *J. Am. Chem. Soc.* **1991**, *113*, 8969.

6. Burroughs, J.A.; Hanley, L. *Anal. Chem.* **1994**, *66*, 3644.

7. Pradeep, T.; Ast, T.; Cooks, R.G.; Feng, B. *J. Phys. Chem.* **1994**, *98*, 9301

8. For an overview, see: Ulman, A. *An Introduction to Ultrathin Organic Films from Langmuir-Blodgett to Self-Assembly*; Academic Press: San Diego, CA, **1991**.

9. (a) Czanderna, A.W.; King, D.E.; Spaulding, D. *J. Vac Sci. Technol.* **1991**, *A9*, 2607;
   (b) Jung, D.R.; King, D.E.; Cznaderna, A.W. *Appl. Surf. Sci.* **1993**, *70/71*, 127;
   (c) Jung, D.R.; King, D.E.; Cznaderna, A.W. *J. Vac. Sci. Technol.* **1993**, *A11*, 2382;
   (d) Jung, D.R.; Czanderna, A.W. *J. Vac. Sci. Technol.* **1994**, *A12*, 2402.

10. (a) Paz, Y.; Trakhtenberg, S.; Naaman, R. *J. Phys. Chem.* **1992**, *96*, 10964;
    (b) Paz, Y.; Trakhtenberg, S.; Naaman, R. *J. Phys. Chem.* **1993**, *97*, 9076;
    (c) Paz, Y.; Trakhtenberg, S.; Naaman, R. *J. Phys. Chem.* **1994**, *98*, 13517.

11. (a) Nuzzo, R.G.; Fusco, F.A.; Allara, D.L. *J. Am. Chem. Soc.* **1987**, *109*, 2358;
    (b) Nuzzo, R.G.; Dubois, L.H.; Allara, D.L. *J. Am. Chem. Soc.* **1990**, *112*, 558.

12. a) Hautman, J.; Klein, M.L. *J. Chem. Phys.* **1989**, *91*, 4994;
    b) Hautman, J.; Bareman, J.P.; Mar, W.; Klein, M.L. *J. Chem. Soc. Faraday Trans.* **1991**, *87*, 2031.
    c) Sprik, M.; Delamarche, E.; Michel, B.; Rothlisberger, U.; Klein. M.L.; Wolf, H.; Ringsdorf, H. *Langmuir* **1994**, *10*, 4116.

13. Ulman, A.; Eilers, J.E.; Tillman, N. *Langmuir* **1989**, *5*, 1147.

14. Bain, C.D.; Troughton, E.G.; Tao, Y.-T.; Evall, J.; Whitesides, G.M.; Nuzzo, R.G. *J. Am. Chem. Soc.* **1989**, *111*, 321.

15. Stinespring, C.D.; Freedman, A.; Kolb, C.E. *J. Vac. Sci. Technol.* **1986**, *A4*, 1946.

16. *Spectra Calc* software package; Galactic: 1989.

17. Benson, S.W. *Thermochemical Kinetics, 2nd ed.*; Wiley: New York, **1976**; p 160.

18. Freedman, A.; Stinespring, C.D. *Appl. Phys. Lett.* **1990**, *57*, 1194.

19. Clark, D.T.; Feast, W.J.; Kilcast, D.; Musgrave, W.K.R. *J. Polym. Sci.: Polym. Chem. Ed.* **1973**, *11*, 389.

20. The C(ls) binding energy for non-fluorinated carbon atoms in polyvinylfluoride,($-CH_2CHF-)_n$, is 1.3 eV higher in energy than that for the carbon atoms in polyethylene.[19,21]

21. *Handbook of X-ray Photoelectron Spectroscopy*; Wagner, C.D.; Riggs, W.M.; Davis, L.E.; Moulder, J.F.; Muilenberg, G.E. (Ed.); Perkin-Elmer: Eden Prairie, MN, **1979**.

22. Graham, R.L.; Bain, C.D.; Biebuyck, H.A.; Laibinis, P.E.; Whitesides, G.M. *J. Phys. Chem.* **1993**, *97*, 9456.

23. Rieke, P.C.; Baer, D.R.; Fryxell, G.E.; Engelhard, M.H.; Porter, M.S. *J. Vac. Sci. Technol.* **1993**, *A11*, 2292.

24. Strong, L.; Whitesides, G.M. *Langmuir* **1988**, *4*, 546.

25. Camillone, N., III; Chidsey, C.E.D.; Liu, G.-Y.; Putvinski, T.M.; Scoles, G. *J. Chem. Phys.* **1991**, *94*, 8493.

26. Laibinis, P.E.; Bain, C.D.; Whitesides, G.M. *J. Phys. Chem.* **1991**, *95*, 7017. The angle between the surface normal and the detection axis was taken to be 45° for the attenuation calculation although the angular resolution of our detector is poor.

27. Chidsey, C.E.D.; Loiacono, D.N. *Langmuir* **1990**, *6*, 682.

28. Tarlov, M.J. *Langmuir* **1992**, *8*, 80.

29. Laibinis, P.E.; Whitesides, G.M. *J. Am. Chem. Soc.* **1992**, *114*, 9022.

30. Herdt, G.C.; Czanderna, A.W. *J. Vac. Sci. Technol.* **1994**, *A12*, 2410.

31. Maoz, R.; Sagiv, J. *Langmuir* **1987**, *3*, 1034.

32. Results very similar to those reported here were obtained for the gas phase chlorination of polyethylene: Elman, J.F., Gerenser, L.J.; Goppert-Berarducci, K.E.; Pochan, J.M. *Macromolecules* **1990**, *23*, 3922.

33. Fenter, P.; Eisenberger, P.; Li, J.; Camillone, N., III; Bernasek, S.; Scoles, G.; Ramanarayanan, T.A.; Liang, K.S. *Langmuir* **1991**, *7*, 2103.

34. *Organic Phototransformations in Nonhomogeneous Media;* Fox, M.A., Ed.; ACS Symposium Series; American Chemical Society: Washington, DC, **1985**; Vol. 278.

35. Bloor, D. *Mol. Cryst. Liq. Cryst.* **1983**, *93*, 183.

36. Bubeck, C. *Thin Solid Films* **1988**, *160*, 1.

37. Schmidt, G.M.J. *Pure Appl Chem.* **1971**, *27*, 647.

38. Ex-situ measurements of the attenuation of the Au(4f) XPS signal by the monolayers using an SSX-100 spectrometer (Surface Science Instruments) with a hemispherical electron energy analyzer and monochromatic Al Kα x-rays confirmed that the thicknesses of the SAMS did not change appreciably as a result of fluorination.

39. Fettis, G.C.; Knox, J.H.; Trotman-Dickenson, A.F. *J. Chem. Soc.* **1960**, 1064.

40. *Handbook of Chemistry and Physics, 73rd ed.*; Lide, D.R., Ed.; CRC Press: Boca Raton, FL, **1992**.

41. The heats of reaction and rate constants for reactions (3) and (4) will not differ dramatically from those for reactions (1) and (2). See, Reference 40 and:

(a) Zhang, Z.; Saini, R.D.; Kurylo, M.J.; Huie, R.E. *J. Phys. Chem.* **1992**, *96*, 9301;

(b) Senkan, S.M.; Quam, D. *J. Phys. Chem.* **1992**, *96*, 10837.

42. Robinson, G.N.; Continetti, R.E.; Lee, Y.T. *J. Chem. Phys.* **1990**, *92*, 275, and references therein.

43. Nesbitt, F.L.; Monks, P.S.; Scanlon, M.; Stief, L.J. *J. Phys. Chem.* **1994**, *98*, 4307.

44. Boudart, M.; Djèga-Mariadassou, G. *Kinetics of Heterogeneous Catalytic Reactions*; Princeton University Press: Princeton, NJ, **1984**; p 31.

45. As noted above, we are treating the vinyl and methyl terminal groups as if they were methylene groups.

46. Timonen, R.; Kalliorinne, K.; Koskikallio, J. *Acta Chem. Sin.* **1986**, *40*, 459.

47. Kurylo, M.J.; Peterson, N.C.; Braun, W. *J. Chem. Phys.* **1970**, *53*, 2776.

48. Munk, J.; Pagsberg, P., Ratajczak, E.; Sillesen, A. *Chem. Phys. Lett.* **1986**, *132*, 417.

49. Zisman, W.A. In *Contact Angle, Wettability and Adhesion*; Fowkes, F.M., Ed.; American Chemical Society, Washington, DC, **1964**; p 1.

50. Shafrin, E.G.; Zisman, W.A. *J. Phys. Chem.* **1957**, *61*, 1046.

51. Graham, R.G.; Whitesides, G.M., unpublished results.

52. Ellison, A.H.; Fox. H.W.; Zisman, W.A. *J. Phys. Chem.* **1953**, *57*, 622.

53. Ellison, A.H.; Zisman, W.A. *J. Phys. Chem.* **1954**, *58*, 260.

54. Liu, G.-Y.; Fenter, P.; Chidsey, C.E.D.; Ogletree, D.F.; Eisenberger, P.; Salmeron, M. *J. Chem. Phys.* **1994**, *101*, 4301.

55. Shafrin, E.G.; Zisman, W.A. *J. Phys. Chem.* **1962**, *66*, 740.

56. Chau, L.-K.; Porter, M.D. *Chem. Phys. Lett.* **1990**, *167*, 198.

Table 1. Advancing contact angles on alkanethiolate SAMs (degrees).[a]

Monolayer	θ_a (H_2O)	θ_a(HD)[b]	Reference
Au/S-$(CH_2)_{19}CH_3$	116	51	this work, 14
Au/S-$(CH_2)_{17}CH=CH_2$	106	36	this work, 14
Au/S-$(CH_2)_{19}CH_3$ + F	82	9	this work
Au/S-$(CH_2)_{17}CH=CH_2$ + F	75	11	this work
Au/S-$(CH_2)_{11}$NH-C-CH_3 $\overset{\|}{O}$	68	30	50
Au/S-$(CH_2)_{11}$NH-C-CH_2F $\overset{\|}{O}$	77	0	50
Au/S-$(CH_2)_{11}$NH-C-CHF_2 $\overset{\|}{O}$	91	44	50
Au/S-$(CH_2)_{11}$NH-C-CF_3 $\overset{\|}{O}$	108	68	50
Au/S-$(CH_2)_2(CF_2)_5CF_3$	118	71	14

a: Uncertainty is ~±3°. b: Hexadecane

50
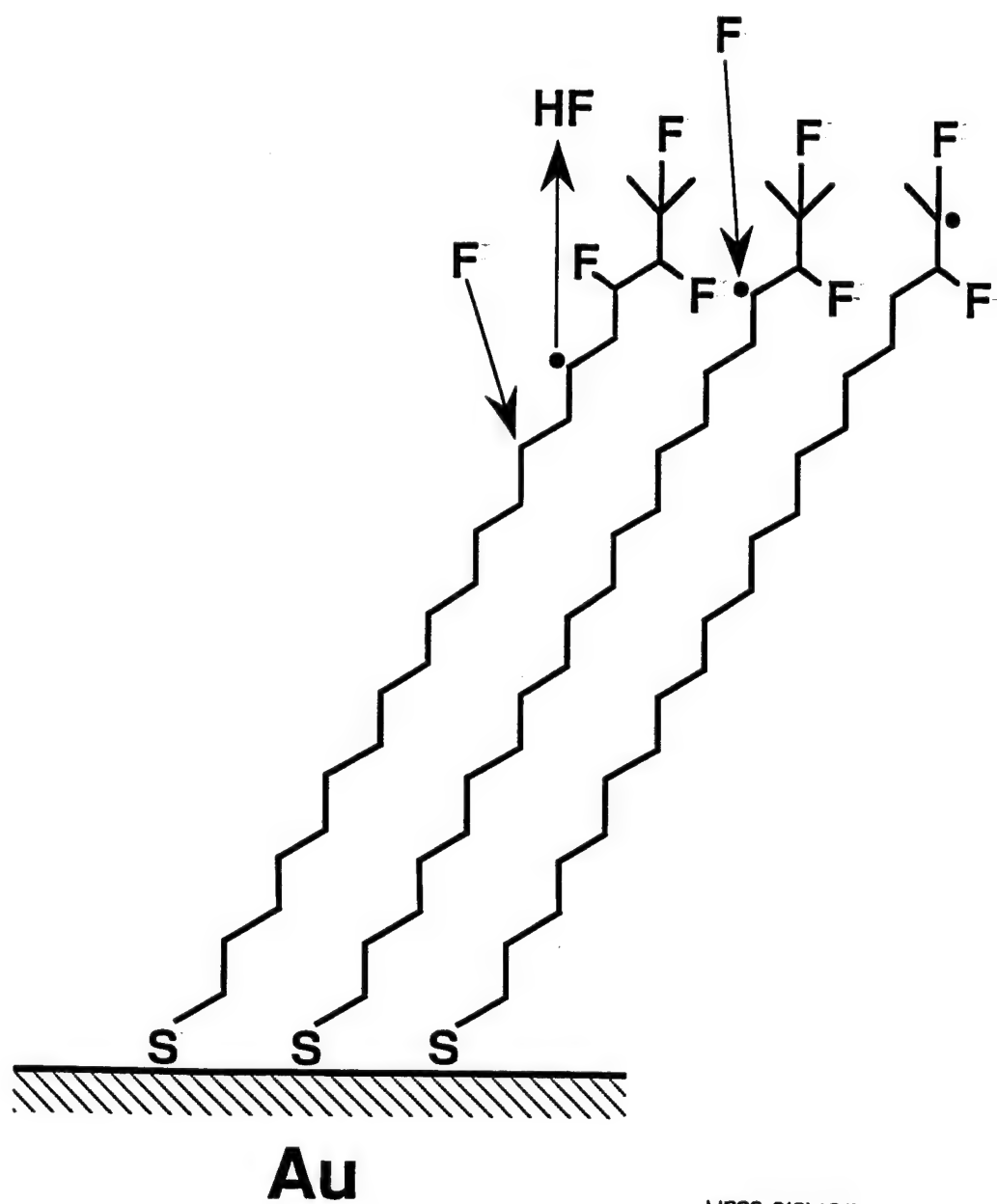
Figure 1. Schematic illustration of the interaction of gas phase F atoms with a methyl-terminated 20 carbon alkanethiolate SAM. Reactions are described in text.

51
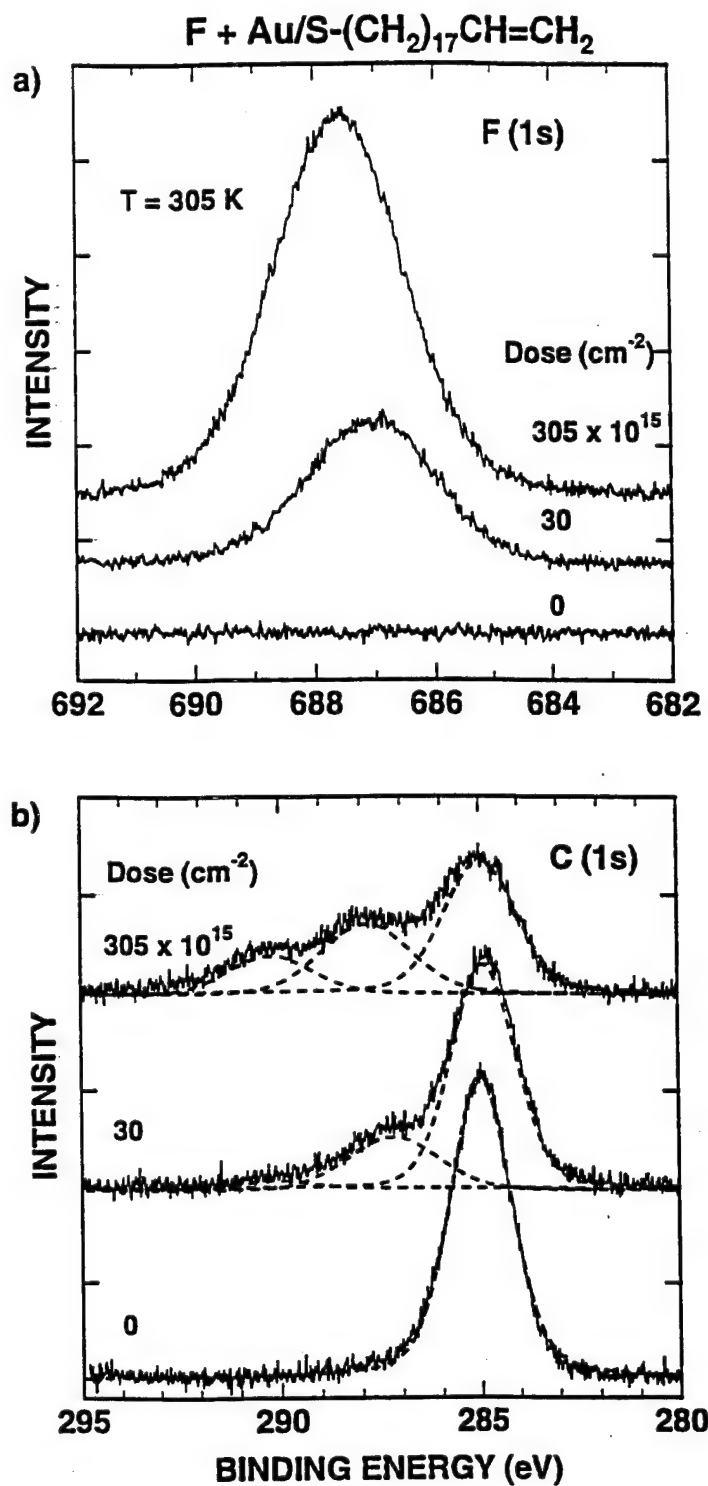
Figure 2. (a) F(1s) and (b) C(1s) XPS spectra for **R1** after different F atom exposures. Lines are Gaussin-Lorentzian fits to the data.
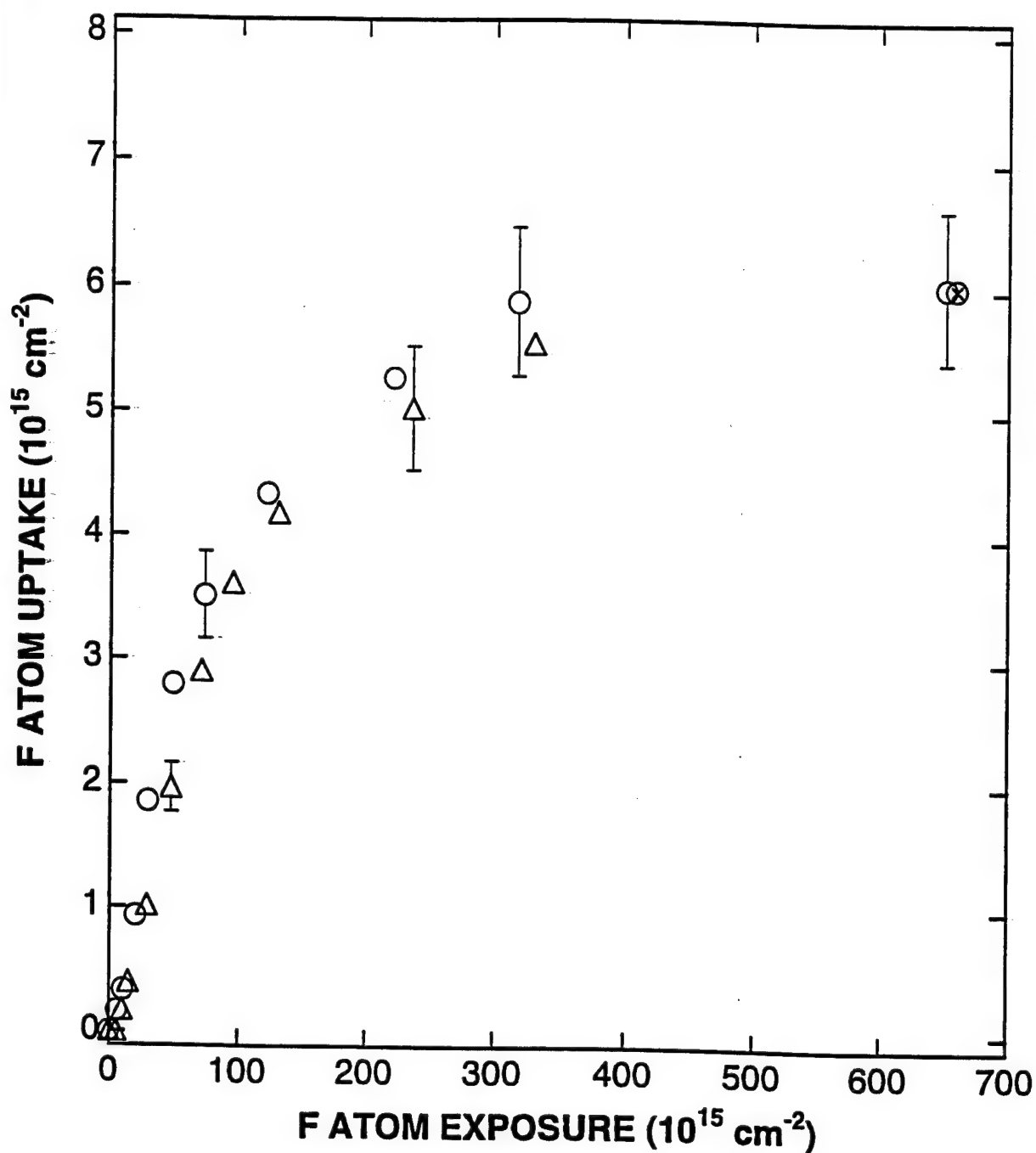
Figure 3

Figure 3. Integrated F(1s) XPS spectra for **R1** (O) and **R2** (△) normalized to the integrated Au(4f$_{7/2}$) XPS signal plotted as a function of F atom exposure. (⊗): Data for **R1** from an extended F atom dose with XPS analysis at the end of the total dose. Error bars reflect uncertainties in the integrated F(1s), C(1s) and Au(4f$_{7/2}$) intensities as described in text.

53
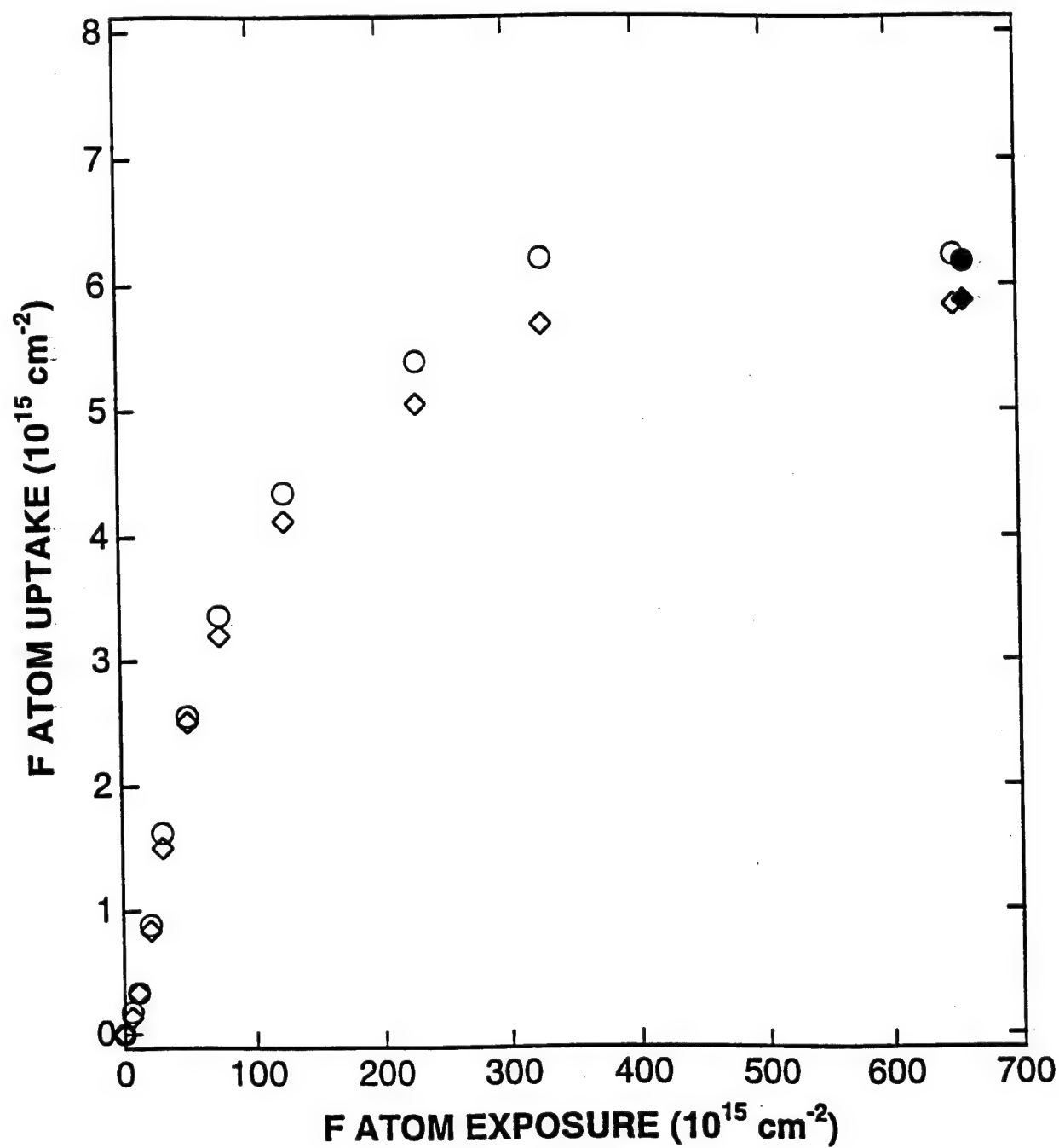
Figure 4. One set of F atom uptake data for **R1**. (o) and (◊): Integrated F(1s) spectra from start and end of XPS analysis run respectively. (●) and (◆): Data for **R1** from an extended F atom dose (see Figure 3).
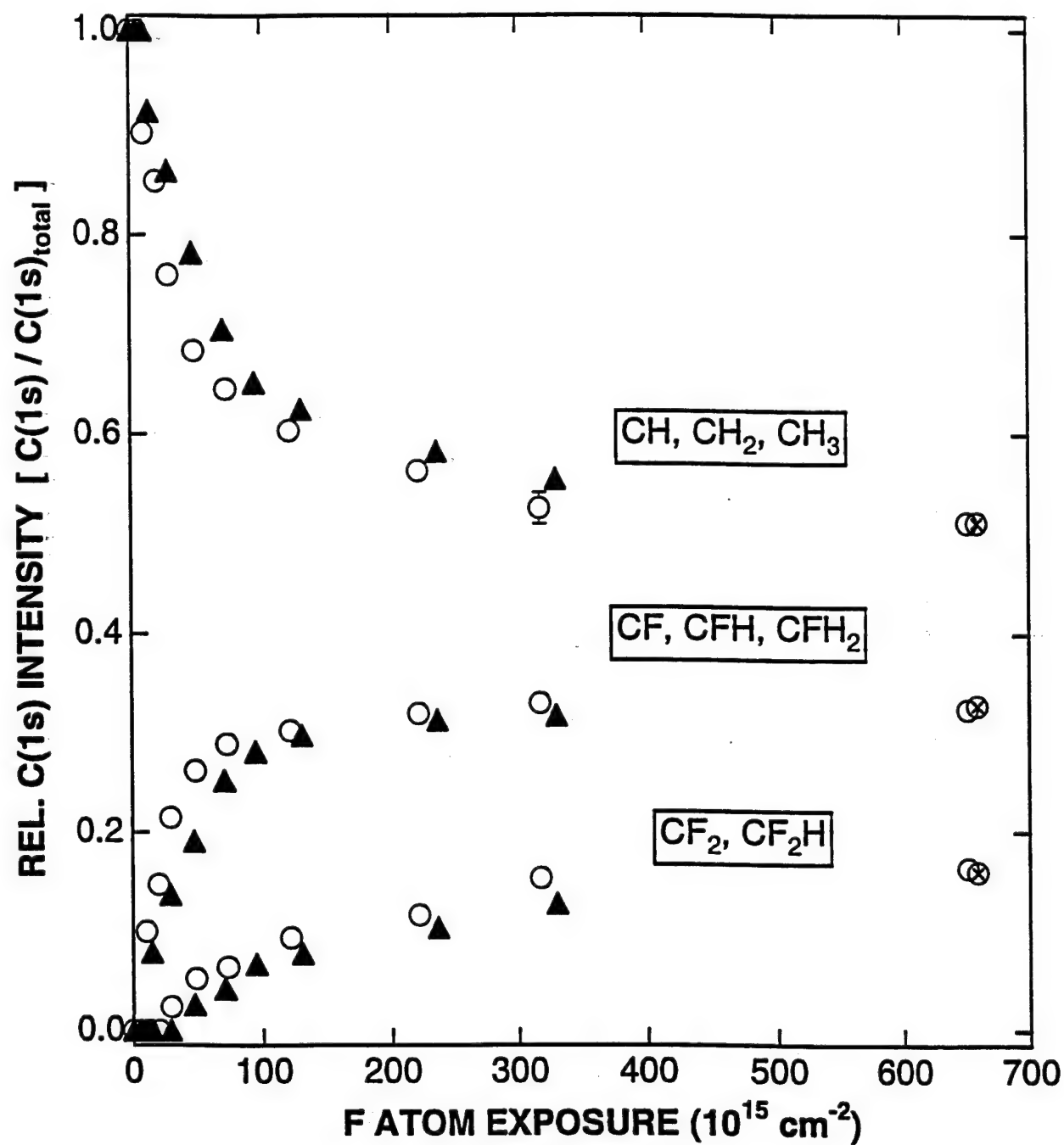
Figure 5. Integrated C(1s) XPS spectra for **R1**(○) and **R2** (▲) for different carbon species normalized to the total integrated C(1s) signal. (⊗): Data for **R1** from an extended F atom dose (see Figure 3).
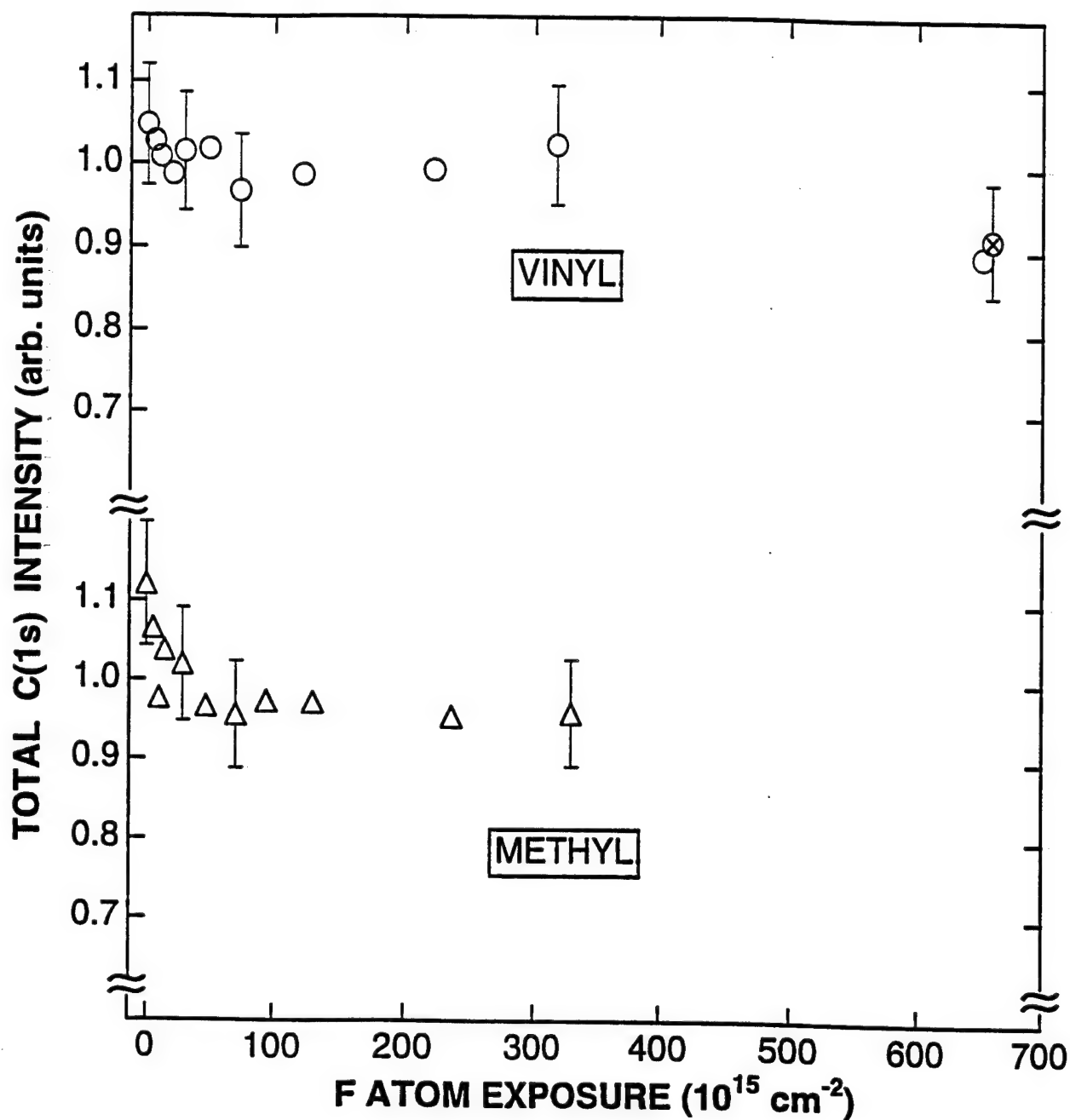
Figure 6. Total integrated C(1s) XPS signal for **R1** (vinyl) and **R2** (methyl) normalized to average of integrated C(1s) signals. Points represent ratio of C(1s) to Au($4f_{7/2}$) divided by average value of C(1s)/Au($4f_{7/2}$) for all points. ($\otimes$): Data for **R1** from an extended F atom dose (see Figure 3).
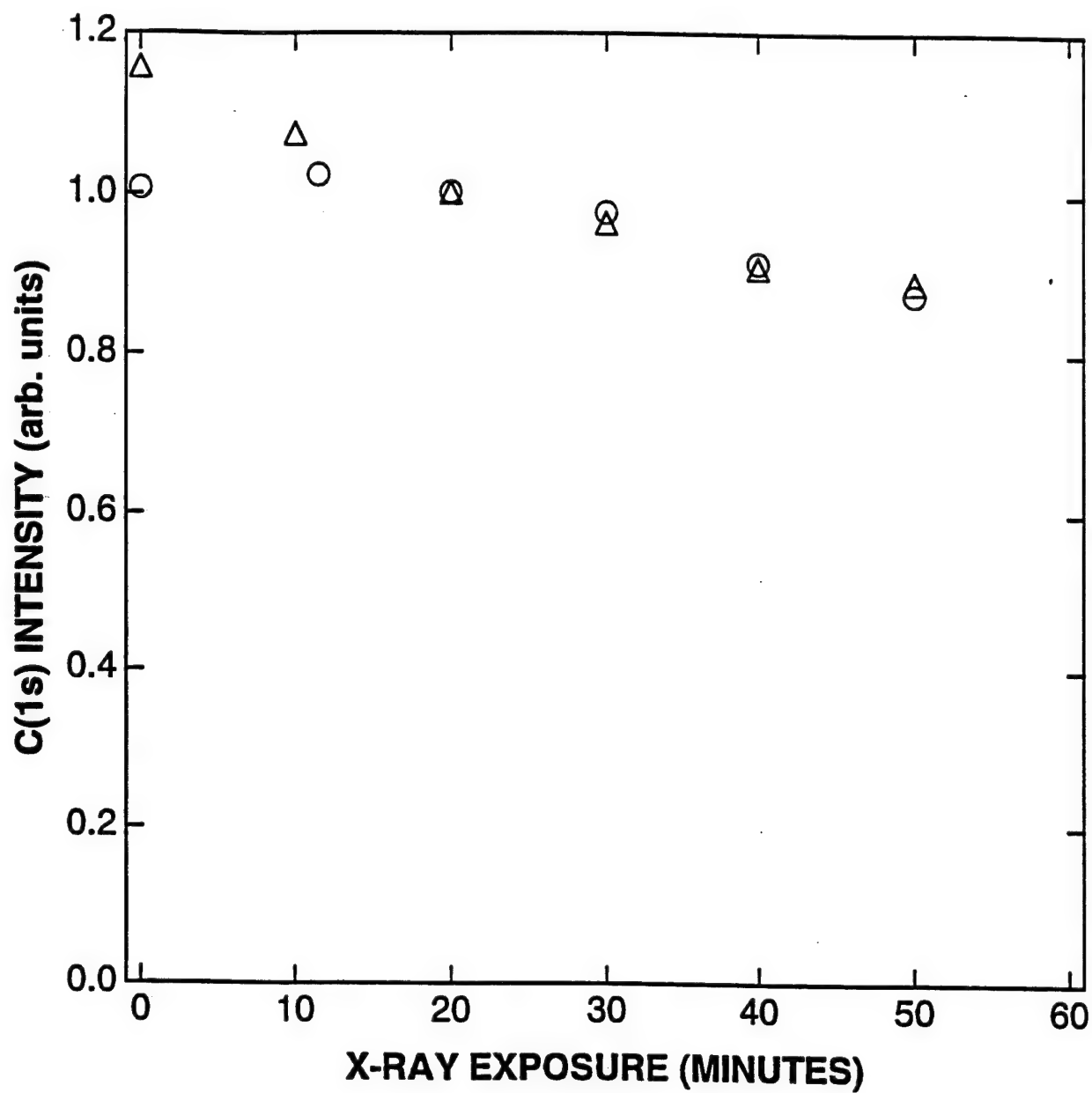
Figure 7.   Total C(1s) signal for vinyl (o) and methyl (Δ) terminated SAMs as a function of x-ray exposure. SAMs were not exposed to F atoms. (See Figure 6.)
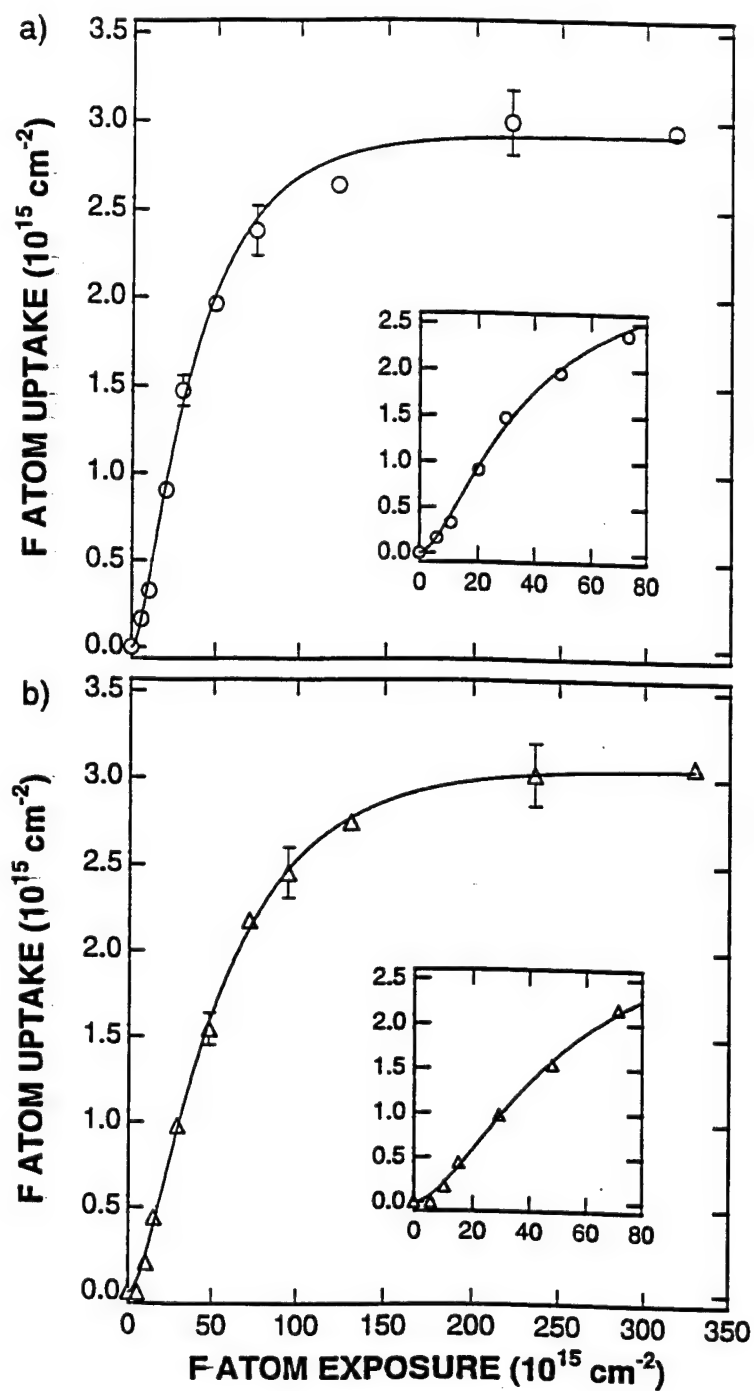
Figure 8

Figure 8. Non-linear least squares fits to monofluorination data for (a) **R1** and (b) **R2**. Fits are for best-fit parameters given in text. Insets show uptake at low exposures.

PRESSURE-BROADENED LINEWIDTH MEASUREMENTS IN THE ν_2 BAND OF THE CH$_3$ RADICAL

Gary N. Robinson, Mark S. Zahniser, Andrew Freedman, and David D. Nelson, Jr.

Center for Chemical and Environmental Physics
Aerodyne Research, Inc.
45 Manning Road
Billerica, MA 01821-3976

8 pages (including abstract)

4 Figures

ABSTRACT

Pressure broadening coefficients for an infrared transition of the methyl radical have been measured for the first time. CH_3 radicals, generated by pyrolyzing di-tert-butyl peroxide in a flow of either N_2 or Ar, were probed using a tunable diode laser and a multipass absorption cell. The Lorentz half-width of the Q(6,6) line of the v_2 band of CH_3 at 607.024 cm^{-1} was measured as a function of pressure at 295 K. The broadening coefficients (HWHM) are b(Ar) = 0.0310 $\pm$ 0.0012 cm^{-1} atm^{-1} and b(N_2) = 0.0390$\pm$0.0020 cm^{-1} atm^{-1}. These coefficients are lower than those for CH_4-Ar, N_2 broadening. This may be due to a lower polarizability or smaller effective hard collision diameter for CH_3 relative to CH_4.

INTRODUCTION

Methyl radicals play a key role in the chemistry of semiconductor processing and combustion and are believed to be abundant in the interstellar medium. In the chemical vapor deposition of diamond, for example, CH_3 is the principal reactive hydrocarbon species (1-3). Thus, the development of quantitative spectroscopic probes of methyl radicals in the gas phase can benefit several fields of research. In this regard, tunable diode laser (TDL) infrared absorption spectroscopy offers a high degree of species specificity and an absolute calibration standard.

Several groups have utilized TDL spectroscopy to measure methyl radical concentrations in semiconductor processing plasmas (4-7). In addition, there has been interest in applying TDL spectroscopy to the measurement of CH_3 in combustion systems (e.g., flames) although, to date, the only radicals that have been measured in such systems with this technique are NO and OH (8,9). In order to quantify radical concentrations using TDL spectroscopy and to determine minimum detectable radical concentrations, it is necessary to know accurately the frequencies, line strengths and pressure-broadened linewidths of the infrared transitions being probed. Pressure-broadened linewidths also provide information about intermolecular interactions and, in planetary studies, the composition of the atmosphere under investigation.

The rovibrational frequencies and transition dipole moments of the v_2 and v_3 bands of the CH_3 radical have been studied by Hirota and co-workers (10,11), Tanarro and co-workers (12,13), and Bethardy and Macdonald (14) using TDL, difference frequency, and F-center laser techniques. Wormhoudt and McCurdy (15) have employed TDL spectroscopy to obtain the v_2 band strength. To our knowledge, however, there have been no measurements of the pressure broadening coefficients of any of the infrared transitions of the methyl radical. In the present study, we have used tunable diode laser spectroscopy to measure the pressure broadened linewidth of the Q(6,6) line (607.024 cm^{-1}) of the v_2 band of CH_3 at 295 K in argon and nitrogen.

EXPERIMENTAL

Methyl radicals were generated by bubbling either argon or nitrogen at ~770 Torr through di-tert-butyl peroxide (Aldrich) (DTBP; $(CH_3)_3$C-O-O-C$(CH_3)_3$) at 263 K (vapor pressure $\approx$ 6 Torr) and flowing the resulting mixture through a 1 cm inner diameter quartz tube that was heated

to 700 K over its last 2 cm with a co-axially wrapped nichrome wire. At this temperature, each molecule of DTBP decomposes to yield two methyl radicals and two acetone molecules. The gas mixture then flowed into a multipass absorption cell where it was interrogated with 16 μm radiation from a tunable Pb-salt diode laser (Laser Photonics). The multipass cell was pumped by a 1420 l/min rotating vane pump. A schematic diagram of the experimental setup is shown in Figure 1.

The pressure in the multipass cell, p_{cell}, was varied by throttling the pump and changing the total gas flow. A needle valve positioned downstream of the bubbler controlled the flow rate of the carrier gas through the pyrolysis tube. This flow rate was 2.4 - 3.1 slpm for N_2 and 4.0 slpm for Ar. For measurements above $p_{cell} = 10$ Torr, an additional gas flow of ~5.5 slpm was added just downstream of the pyrolysis tube. High gas flow rates were used to maximize the flow velocity and thereby minimize the residence time of the radicals in the system. This minimized the loss of CH_3 as a result of wall reactions and radical recombination. Pressures were measured with capacitance manometers and flow rates were measured with a thermal conductivity-type flowmeter and by measuring the change in pressure with time in a vessel of known volume. The temperature of the multipass absorption cell was 295 K.

The diode laser output was collected with an off-axis paraboloidal mirror, focused into the multiple pass absorption cell, passed through a 0.25 m monochromator for mode selection and finally focused onto a HgCdTe detector (Figure 1). Optical alignment was facilitated by co-aligning the infrared beam with a visible beam from a helium-neon laser using a dichroic mirror which reflects the infrared and transmits the visible radiation. The multiple pass cell utilizes astigmatic mirrors to minimize the cell volume for a given path length. Details of the cell design have been given in previous publications (16 - 18). The diode laser beam traversed the 55 cm long absorption cell 182 times yielding a total absorption path length of 100 m. The gas flow enters the multipass cell through a tube that passes over the top of one mirror and exits around the perimeter of the other mirror.

The data acquisition method employed is based on rapid sweep integration over the full transition lineshape (17). This is accomplished by scanning the laser frequency under computer control and synchronously measuring the transmitted infrared radiation intensity. Typically a 2000 step scan was used and the laser current was dropped below threshold for the last 10 steps of each scan to provide a baseline for measuring the laser radiation intensity. The spectral information can be analyzed in real time with a nonlinear least-squares fitting routine which returns both the spectral line profile and the laser intensity spectrum. The area under the absorption line together with the line strength can be used to calculate the average number density of the species being observed.

The nonlinear least-squares fitting routine is crucial for measuring absolute absorbances and lineshapes. The fitting routine uses the Levenberg-Marquardt approach (19). The diode laser intensity spectrum is represented as a slowly varying polynomial of adjustable order; typically a fourth order polynomial is used. The absorption lineshape may be fit to either a Gaussian, pressure-broadened Lorentzian, or Voigt profile. The position, width, and height of the line are fit

61

simultaneously with the diode laser polynomial baseline. The absolute accuracy of the area under the peak determined by the fit is a few percent.

In order to calibrate the infrared laser frequency for the pressure broadening measurements, a small flow of CO_2 was periodically added to the secondary gas flow. CO_2 has several regularly spaced rovibrational lines near the Q(6,6), v_2 band transition of CH_3 at 607.02 cm^{-1}. The frequencies of these lines were obtained from the HITRAN database ([20]). The frequency calibration was determined from a linear least-squares fit to a straight line of frequency vs. peak position for the CO_2 lines. The regression coefficients for these fits were typically >0.999 indicating that the frequency tuning of the laser was linear in the region of the Q(6,6) CH_3 line. No CO_2 was added when the pressure-broadened CH_3 spectra were recorded.

RESULTS

A survey spectrum from 606.72 to 607.06 cm^{-1} obtained at 1.5 Torr with argon as the carrier gas is presented in Figure 2. The spectrum shows the Q(6,6) absorption line of the v_2 band of CH_3 at 607.024 cm^{-1} with an absorbance of 0.37 and several CO_2 ro-vibrational lines. From this absorbance and the strength of the Q(6,6) line,[1] we calculate an average number density of 8.0 x 10^{10} CH_3 radicals/cm^3 at 1.5 Torr. The Q(5,5) line of CH_3 at 606.587 cm^{-1} was observable under the conditions of most of these experiments but its absorption cross section is approximately half that of the Q(6,6) line and its pressure broadening coefficient was not studied.

An expanded spectrum of the Q(6,6) line of CH_3 in Ar at 20 Torr is presented in Figure 3 along with a Voigt fit to the spectrum. In fitting the spectra, the Gaussian half-width was fixed at 1.4 x 10^{-3} cm^{-1} which is equal to the half-width of the Q(6,6) line at low pressure (p_{cell} = 1.5 Torr). This linewidth is slightly larger than the calculated Doppler-broadened linewidth ($\Gamma_{Doppler}$ = 9.7 x 10^{-4} cm^{-1} (HWHM)) and implies a laser linewidth, Γ_{laser}, of 1.0 x 10^{-3} cm^{-1}, i.e., $(\Gamma_{low\ pressure})^2 = (\Gamma_{Doppler})^2 + (\Gamma_{laser})^2$. With the Gaussian half-width fixed at its low pressure value, pressure-dependent Voigt profiles were obtained by fitting the peak position, peak height, and Lorentzian half-width.

The Lorentzian component of the observed Q(6,6) linewidth is plotted in Figure 4 as a function of cell pressure for argon and nitrogen carrier gases.[2] The error bars, obtained by averaging several measurements at each pressure, represent 95% confidence limits. Over most of the 5 - 40 Torr pressure range investigated in the pressure broadening experiments, the flow rate was fixed and the pressure was increased by throttling the pump. The methyl radical concentration was observed to decrease with increasing pressure. Modeling calculations of the reaction kinetics indicated that this was due principally to radical recombination.

The observed half-widths were fit to a straight line using a linear least-squares fit weighted by the inverse of the plotted uncertainties. The slopes of the fit lines yield pressure broadening coefficients (HWHM), b, of 3.10 ($\pm$ 0.12) x 10^{-2} cm^{-1} atm^{-1} for argon and 3.90 ($\pm$ 0.20) x 10^{-2} cm^{-1} atm^{-1} for nitrogen. The zero pressure intercepts of the plots are -7.2 ($\pm$4.2) x 10^{-5} cm^{-1} and

-4.6 ($\pm$5.8) x 10^{-5} cm^{-1} for argon and nitrogen respectively. The non-zero intercepts are due to neglect of the small Lorentz contribution (<10%) to the linewidth at 1.5 Torr.

DISCUSSION

Although there are no published values for the pressure broadening coefficients of CH_3 to which to compare our results, there is an abundant literature on the pressure broadening of methane's infrared absorption lines [21,22]. In an effort to put our limited amount of CH_3 data in context, we will briefly summarize some pertinent CH_4 results.

Most line broadening measurements on methane have been made in the v_3 (3019 cm^{-1}) and v_4 (1306 cm^{-1}) bands with helium, hydrogen, nitrogen and air as the broadening gases. The magnitudes of the broadening coefficients for CH_4 appear to have little or no systematic dependence on vibrational or rotational quantum number but do display a modest dependence on tetrahedral symmetry species [23]. In the v_2 (1534 cm^{-1}), v_3 (3019 cm^{-1}), and v_4 (1306 cm^{-1}) bands, the pressure-broadening coefficients (HWHM) are in the range of 0.04 - 0.07 cm^{-1}atm^{-1} for nitrogen [21,22].

In the case of CH_4, the broadening efficiencies of Ar and N_2 have been measured mostly in the v_4 band. The most extensive measurements have been carried out by Varanasi and Chudamani [24,25] and by Rinsland et al. [26,27]. These groups obtained values for b(Ar)/b(N_2) of 0.873 [24], 0.874 [25], and 0.877 [27] which all agree within experimental error. In the $3v_3$ band, Fox et al. found b(Ar)/b(N_2) = 0.910 [23]. Gerritsen and Heller measured b(Ar)/b(N_2) = 0.918 in the v_3 band [28]. The larger broadening efficiency for N_2 relative to Ar has been attributed to the molecule's quadrupole moment. Our value of b(Ar)/b(N_2), 0.795 $\pm$ 0.070, although smaller than the ratios measured for CH_4, also indicates a higher broadening efficiency for N_2.

Assuming a representative value of 0.055 cm^{-1}atm^{-1} for b(CH_4-N_2) for the sake of comparison, the pressure-broadening coefficients that we measure for CH_3 (0.039 and 0.0310 cm^{-1} atm^{-1} for N_2 and Ar respectively) are about 30% smaller than those for CH_4. Although detailed calculations based on the CH_3-M and CH_4-M (M=N_2 and Ar) intermolecular potentials are necessary to explain this difference, the pressure broadened linewidth scales with the leading term in the collision interruption function which, in the traditional formulation of line broadening theory, correlates with the strength of the intermolecular attractive force [29]. In the cases of CH_4-Ar, the dominant contribution to this attractive interaction is the anisotropic dispersion energy which has the form AR^{-7}, where A is the higher polarizability tensor of the molecule and R is the intermolecular separation [30]. The lowest order multipole moment of CH_4 is the octopole moment but the interaction of an octopole with an octopole-induced dipole is significantly weaker than the anisotropic dispersion interaction [29]. Since A scales with the polarizability, α, of the molecule [30], the argon broadening coefficients of CH_4 and CH_3 should scale with their polarizabilities if the anisotropic dispersion interaction also dominates the CH_3-Ar interruption function. However, the lowest order multipole moment of CH_3 is the quadrupole

moment so the quadrupole-induced dipole interaction, whose energy also scales as R^{-7}, should contribute to Ar-broadening of the CH_3 linewidth as well (31). (Note that the methyl radical has D_{3h} symmetry.) To our knowledge, the quadrupole moment of CH_3 has not been determined but it is probably small. Thus, we expect that the interaction of a quadrupole with a quadrupole-induced dipole is weaker than the anisotropic dispersion interaction[3] and we ignore its contribution to the CH_3 linewidth.

$\alpha(CH_3)$ is expected to be smaller than $\alpha(CH_4)$ since hydrocarbon polarizabilities scale with the number of C-H bonds (32). The experimental value for $\alpha(CH_4)$ is 17.50 au^3 (33). There have been no experimental determinations of $\alpha(CH_3)$. However, Wittbrott and Schlegel have recently calculated the polarizabilities of CH_3 and CH_4 using *ab initio* methods (34). These calculations were done with the Gaussian series of programs at the MP2/6-311+G(3df,2p) level of theory using geometries optimized at the same level of theory. The values that they obtained are $\alpha(CH_4)$ = 15.814 au^3 and $\alpha(CH_3)$ = 14.834 au^3. The calculated CH_4 polarizability is somewhat lower than the experimental value but it is the best that conventional *ab initio* methods can do easily at this point. Nevertheless, the ratio of the two values remains roughly constant when one compares different levels of theory. Thus, our observation that the argon broadened linewidth of CH_3 is smaller than that of CH_4 is consistent with a weaker dispersion interaction for CH_3-Ar relative to CH_4-Ar.

Recently Neshyba et al. (35) have calculated pressure-broadened linewidths for the v_3 band of methane using a static intermolecular potential that is described as a sum of electrostatic forces and Lennard-Jones (6-12) atom-atom terms. They conclude that the repulsive part of the intermolecular potential makes the dominant contribution to the linewidth. In this case, the observed differences between the CH_3 and CH_4 broadening coefficients would be attributed to differences in the short range parts of the intermolecular potentials. Our results may therefore imply a smaller effective hard collision diameter for CH_3 relative to CH_4.

SUMMARY

Pressure broadening coefficients for the $Q(6,6)$ line of CH_3 in the v_2 band have been measured in N_2 and Ar at 295 K. These are the first such coefficients to be measured for the methyl radical. The values are 3.10 ($\pm$ 0.12) x 10^{-2} cm^{-1} atm^{-1} in argon and 3.90 ($\pm$ 0.20) x 10^{-2} cm^{-1} atm^{-1} in nitrogen. Our observation that the broadening efficiency of argon is lower than that of nitrogen is consistent with previous work on the v_3 and v_4 bands of CH_4. However, the ratio $b(Ar)/b(N_2)$ is smaller for CH_3 than for CH_4. The magnitudes of the CH_3 broadening coefficients are also lower than those for CH_4. This may be due to a lower polarizability or smaller hard collision diameter for CH_3 relative to CH_4.

ACKNOWLEDGEMENTS

REFERENCES

1.   F.G. Celii and J.E. Butler Annu. Rev. Phys. Chem. 42, 643-684 (1991)

2.   S. Skokov, B. Weiner, and M. Frenklach J. Phys. Chem. 98, 7073-7082 (1994)

3.   S.J. Harris, Appl. Phys. Lett. 56, 2298 (1990).

4.   J. Wormhoudt, J. Vac. Sci. Technol. A8, 1722-1725 (1990).

5.   F. Celii, P. Pehrsson, H. Wang, and J. Butler, Appl. Phys. Lett. 52, 2043 (1988).

6.   S. Naito, M. Ikeda, N. Ito, T. Hattori, and T. Goto, Jpn. J. Appl. Phys. 1 12A, 5721 (1993).

7.   P.B. Davies and P.M. Martineau, J. Appl. Phys. 71, 6125-6135 (1992).

8.   J. Wormhoudt, M.S. Zahniser, D.D. Nelson, J.B. McManus, R.C. Miake-Lye, and C.E. Kolb, "Laser Applications in Combustion and Combustion Diagnostics II," R.J. Locke, ed., Proc. Soc. Photo-Opt. Instrum. Eng. 2122, 49-60 (1994).

9.   B. Rosier, P. Gicquel, D. Henry, and D. Coppalle, Rech. Aerosp. 45, (1988).

10.   C. Yamada, E. Hirota, and K. Kawaguchi, J. Chem. Phys. 75, 5256-5264 (1981).

11.   C. Yamada and E. Hirota, J. Chem. Phys. 78, 669-671 (1983).

12.   I. Tanarro, M.M. Sanz, D. Bermejo, C. Domingo, and J. Santos, J. Chem. Phys. 100, 238-245 (1994).

13.   I. Tanarro, M.M. Sanz, D. Bermejo, C. Domingo, J. Santos, and J.L. Domenech, J. Phys. Chem. 98, 5862-5866 (1994).

14.   G.A. Bethardy and R.G. Macdonald, J. Chem. Phys. 103, 2863 (1995).

15.   J. Wormhoudt and K.E. McCurdy, Chem. Phys. Lett. 156, 47-50 (1989).

16.   D.R. Herriott and H.J. Schulte, Jr., Appl. Optics 4, 883-889 (1965).

17.   D.D. Nelson, Jr. and M.S. Zahniser, J. Mol. Spectrosc. 166, 273-279 (1994).

18.   J.B. McManus, P.L. Kebabian, and M.S. Zahniser, Appl. Optics 34, 3336-3348 (1995).

19.   W.H. Press, B.P. Flannery, S.A. Teukolsky, and W.T. Vetterling, "Numerical Recipes," pp. 521-538, Cambridge University Press, Cambridge, UK, 1986.

20.   L.S. Rothman, R.R. Gamache, A. Goldman, J.-M. Flaud, R.H. Tipping, C.P. Rinsland M.A.H. Smith, R.A. Toth, L.R. Brown, V. Malathy Devi, and D.C. Benner, J. Quant. Spectrosc. Radiat. Transfer 48, 469-507 (1992).

21.   M.A.H. Smith, C.P. Rinsland, B. Fridovich, and K.N. Rao, in "Molecular Spectroscopy: Modern Research, Vol. III," K.N. Rao, ed., pp. 111-248, Academic Press, Orlando, FL, 1985.

22. M.A.H. Smith, C.P. Rinsland, V. Malathy Devi, L.S. Rothman, and K.N. Rao, in "Spectroscopy of the Earth's Atmosphere and Interstellar Medium," K.N. Rao and A. Weber, eds., pp. 153-260, Academic Press, San Diego, CA, 1992.

23. K. Fox, D.E. Jennings, E.A. Stern and R. Hubbard, J. Quant. Spectrosc. Radiat. Transfer 39, 473-476 (1988).

24. P. Varanasi and S. Chudamani, J. Quant. Spectrosc. Radiat. Transfer 41, 335-343 (1989).

25. P. Varanasi and S. Chudamani, J. Quant. Spectrosc. Radiat. Transfer 43, 1-11 (1990).

26. C.P. Rinsland, V.M. Devi, M.A.H. Smith and D.C. Benner, Appl. Optics 27, 631-651 (1988).

27. C.P. Rinsland, V.M. Devi, M.A.H. Smith and D.C Benner, Appl. Optics 28, 2111-2118 (1989).

28. H.J. Gerritsen and M.E. Heller, Appl. Opt., Suppl. 2, 73-77 (1965).

29. P. Varanasi, J. Quant. Spectrosc. Radiat. Transfer 14, 995-1008 (1974); J. Quant. Spectrosc. Radiat. Transfer 15, 255-258 (1975).

30. A.D. Buckingham, Discussions Faraday Soc. 40, 232-238 (1965); Adv. Chem. Phys. 12, 107-142 (1967).

31. A.D. Buckingham, J. Chem. Phys. 48, 3827-3828 (1968).

32. J.O. Hirschfelder, C.F. Curtiss, and R.B. Bird, "Molecular Theory of Gases and Liquids," p. 947, Wiley, New York, 1954.

33. "Handbook of Chemistry and Physics," D.R. Lide, ed., 71st Edition, p. 10-200, CRC Press, Boca Raton, FL, 1990.

34. J.M. Wittbrott and H.B. Schlegel, private communication.

35. S.P. Neshyba, R. Lynch, R. Gamache, T. Gabard, and J.-P. Champion, J. Chem. Phys. 101, 9412-9421 (1994).

FOOTNOTES

1. From the measured strength of the Q(8,8) line at 608.3 cm^{-1} (15) and the relative statistical weight of the Q(6,6) transition, we calculate a Q(6,6) line strength of 9.2 x 10^{-19} cm^{-1} (cm^2/molecule).

2. The initial concentration of DTBP in the flow is sufficiently small that the effect of the acetone by-product on the observed linewidths should be negligible.

3. This is in contrast with the energy of interaction of a quadrupole with an dipole-induced dipole which can be comparable in magnitude to the anisotropic dispersion energy (31).
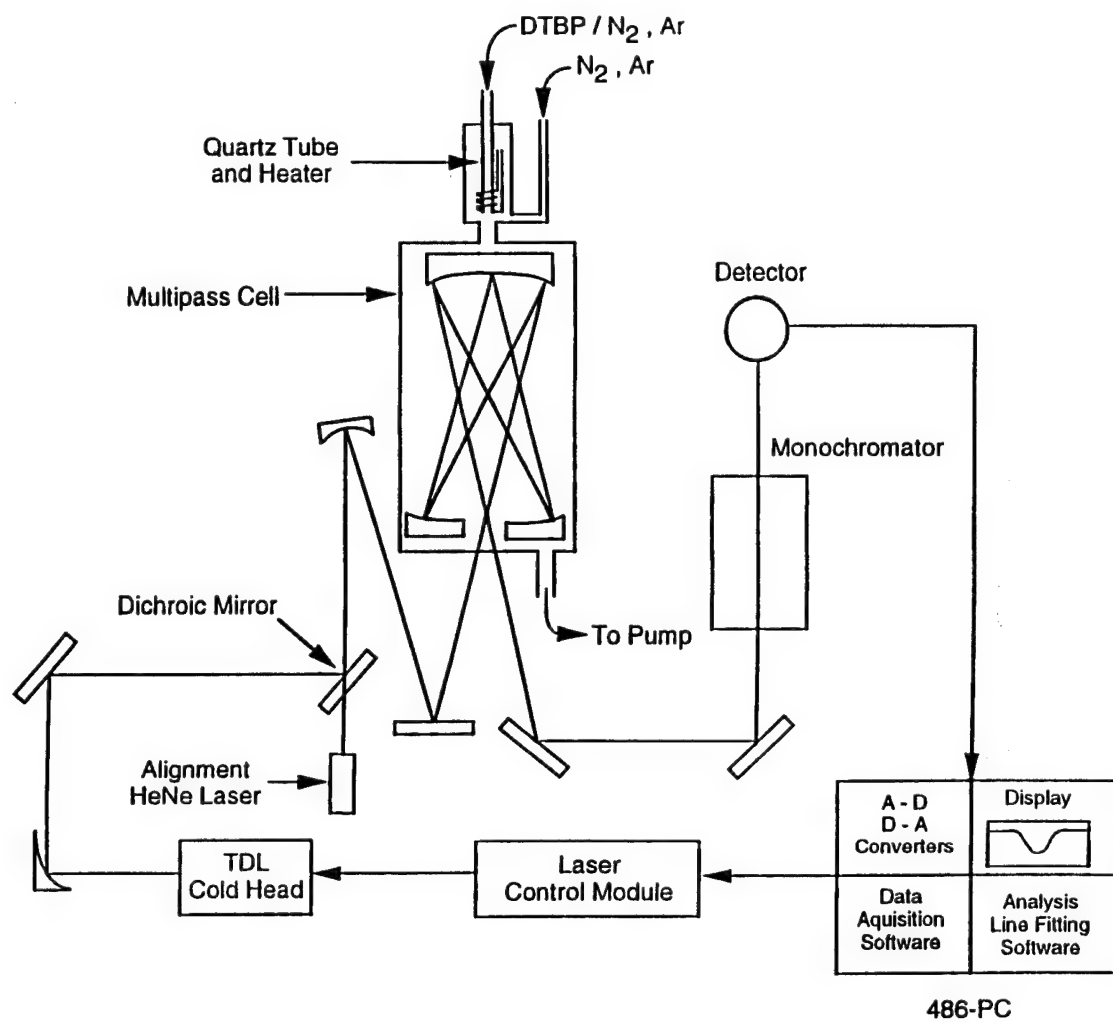
66

Figure 1.   Schematic of experimental apparatus including methyl radical source and tunable diode laser spectrometer.
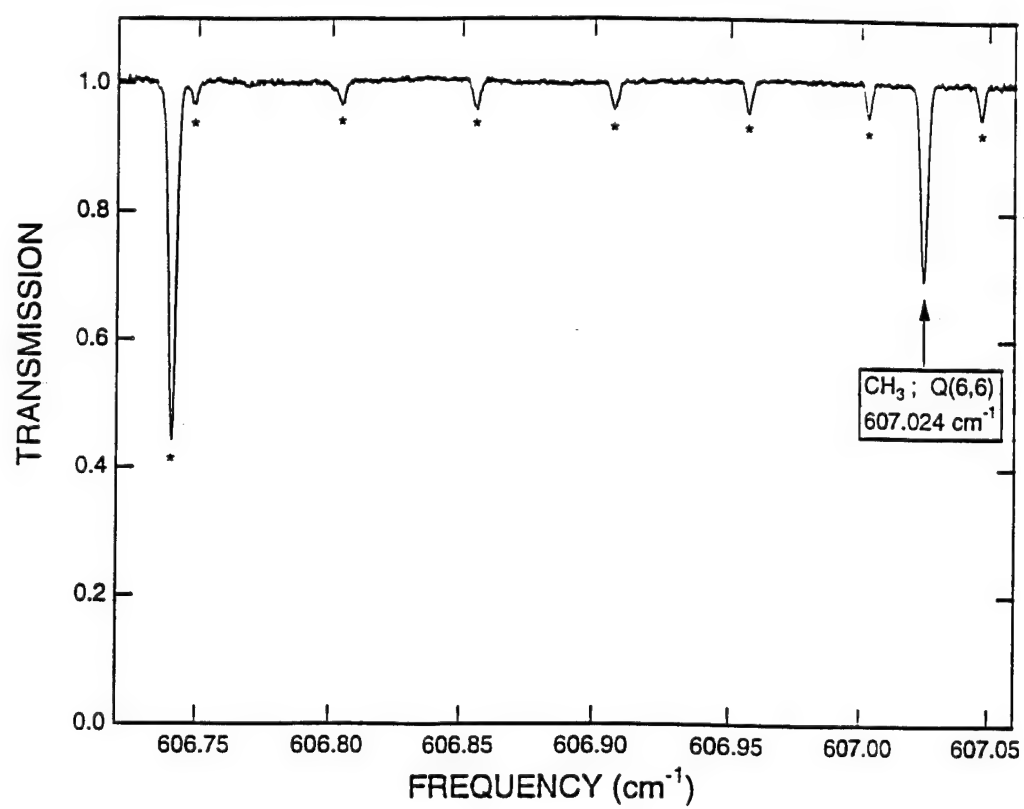
Figure 2. Absorption spectrum of CH_3 and CO_2 in Ar (p_{cell} = 1.5 Torr). CO_2 lines are marked with asterisks.
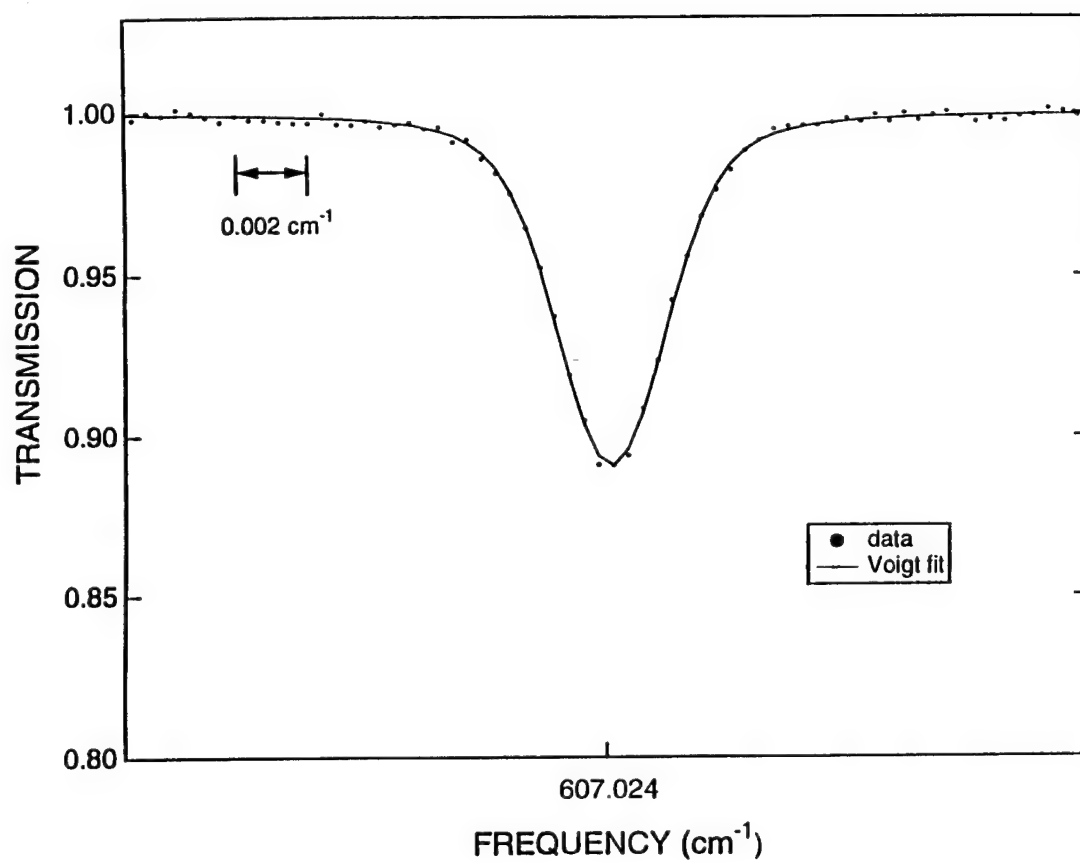
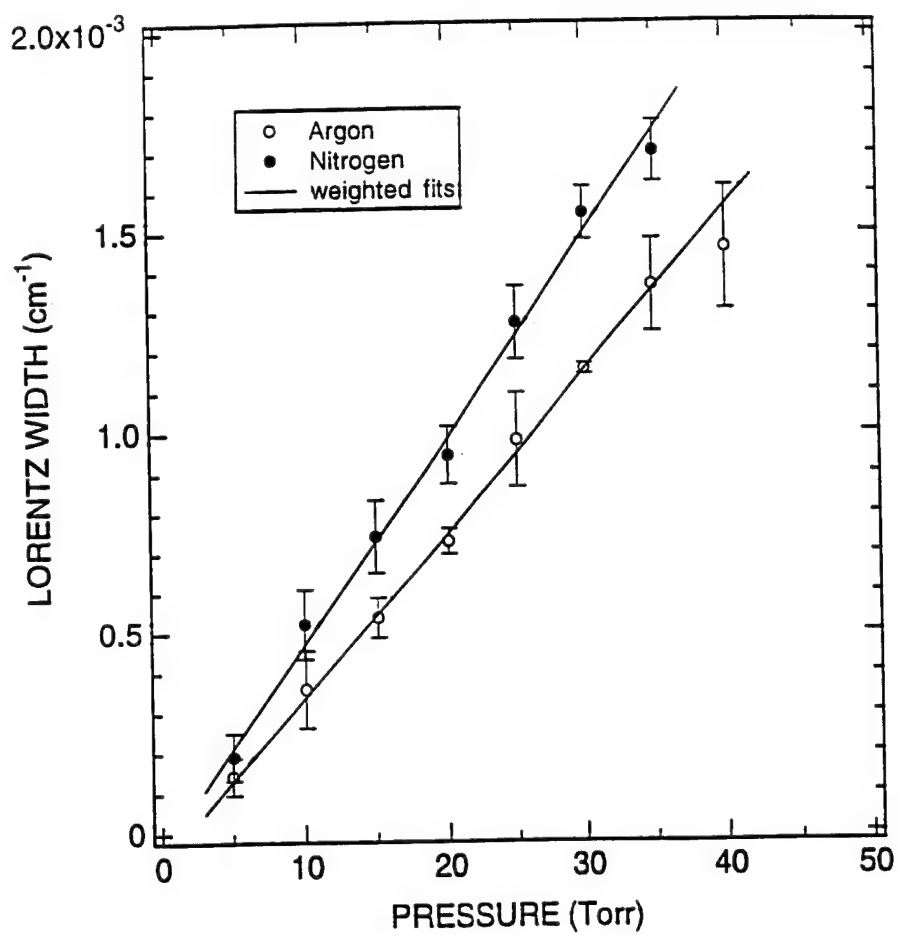Figure 3.   Expanded view of Q(6,6) line of CH_3 in Ar (p_{cell} = 20 Torr) with Voigt fit to the data.

Figure 4.   Pressure-broadened linewidths (HWHM) of the Q(6,6) line of CH_3 in argon and nitrogen with weighted least-squares fits to the data.

TRIBOLOGICAL PERFORMANCE OF DIAMOND THIN FILMS

Prepared by

A. Freedman
Aerodyne Research, Inc.
45 Manning Road
Billerica, MA 01821

and

Wei Zhu and Jeffrey T. Glass,
Department of Materials and Engineering Science
North Carolina State University, Raleigh, NC

and

W. Thomas Brydges and Dean R. Gerber
The Pure Carbon Co., St. Mary's, PA 15857

Prepared for

Third International Symposium on Diamond Materials
Honolulu, Hawaii

March 1993

TRIBOLOGICAL PERFORMANCE OF DIAMOND THIN FILMS

Andrew Freedman,
Aerodyne Research,Inc., 45 Manning Road, Billerica Ma 01821;

Wei Zhu and Jeffrey T. Glass,
Department of Materials and Engineering Science
North Carolina State University, Raleigh, NC; and

W. Thomas Brydges and Dean R. Gerber,
The Pure Carbon Co., St. Mary's, PA 15857

Both hydrogenated and fluorinated diamond films have been tested for wear and friction. The diamond films were deposited on reaction-bonded silicon carbide substrates using a hot filament approach. Several samples were fluorinated using a remote low pressure discharge of fluorine in helium. The diamond films were subjected to tribological testing on a modified drill press tribotester designed to simulate conditions found in rotary union and joint applications. The major conclusion that can be drawn from the test results is that the unpolished diamond coated samples used as a backface, whether fluorinated or not, significantly reduce wear on a SiC seal nose under dry conditions compared to uncoated SiC backfaces.

INTRODUCTION

The recent development of new techniques for the production of homo- and hetero-epitaxial diamond thin films has revealed a host of possible applications for such films [1,2]. Foremost among these applications are coatings for moving parts whose performance is enhanced by low coefficients of friction and improved wear characteristics. To obtain optimum performance from these materials, it may be necessary to controllably modify the characteristics of the surface and near surface layers. Fluorination has been suggested as a solution to the fact that diamond surfaces show high coefficients of friction when adsorbed water or oxygen is present [3,4]. We have tested both hydrogenated and fluorinated diamond films for their tribological properties under realistic conditions.

EXPERIMENTAL

Diamond films were grown on reaction bonded silicon carbide substrates in a hot filament chemical vapor deposition system at North Carolina State University. The basic approach taken here was to grow diamond films at relatively low substrate temperatures (600-800 °C) and high nucleation densities; this results in small size nuclei which better accommodate the thermal stress at the diamond/substrate interface and thus improve the adhesion. In addition, the methane concentrations in hydrogen were manipulated in both the nucleation and growth stages in order to achieve high nucleation densities and small grain sizes. For example, the nucleation of diamond was first conducted at a higher methane concentration (2.0%) for about 30 minutes. Then the

72

deposition conditions were switched to a concentration of methane in hydrogen of 1.0%, gas pressure of 50 torr, and total gas flow rate of 300 sccm.

All films were characterized using Raman spectroscopy and Scanning Electron Microscopy (SEM) which provide information on the structural quality and surface morphology of the films. Figure 1 provides examples of Raman spectra obtained on both silicon carbide and nitride substrates; typical spectral widths were 5-8 cm^{-1} FWHM, indicating excellent film quality. The surfaces of these films consisted of well-faceted diamond grains in the size range of 1.5-3.5 μm; Figure 2 shows a typical SEM micrograph.

The SiC substrates chosen for testing were made from fine-grained α–silicon carbide (known as PR-9242). The SiC matrix is reaction-bonded through the infiltration of molten silicon to provide the desired properties. It is used in high pressure plates and liners in fuel systems, mating rings in rotary union and joint applications, bearings in pumps which handle abrasive and corrosive fluids, and mating rings for graphite noises in mechanical face seals. A list of its properties is given below:

Properties of PR-9242

Temperature Limit	1370 °C
Hardness	2400 Vickers
Compressive Strength	2750 kN mm^{-2}
Thermal Conductivity	145 W/(m·°C) (at 38 °C)
Coefficient of Thermal Expansion	4.5 x 10^{-6} °C^{-1}
Modulus of Elasticity	365 kN mm^{-2}
Density	3.1 g cm^{-3}

Diamond films were fluorinated using a low pressure remote discharge. Fluorine atoms were created by striking a discharge (using an Evenson cavity) in a 5% F_2 in helium gas mixture which flows through an alumina tube at 1 Torr total pressure. Diamond films were cleaned in an ultrasonic cleaner using successive baths of acetone, ethanol, and distilled water and dried in air in an oven at 300 °C. They were then exposed to the atomic fluorine gas mixture for 300 seconds. X-ray photoelectron spectra of the fluorinated samples showed the characteristic C-F peak found in the C 1s spectrum when fluorinating natural diamond substrates.

Tribological testing was performed at the Pure Carbon Division of the Stackpole Corporation on a modified drill press tribotester intended to simulate conditions found in rotary union and joint applications, pumps which handle abrasive and corrosive fluids, and mating components in mechanical face seals. The diamond coated substrates were the stationary pieces (backfaces) in these tests; temperature was monitored using embedded thermocouples. Silicon carbide seal noses were spring mounted under constant pressure; the measured torque was then converted to a coefficient of friction. The wear on the nose piece was measured using a micrometer; wear on the backfaces was measured using a Surfanalyzer. Tests were run under both wet (deionized water) and dry conditions at a pressure of 20 psi and 2000 rpm.

RESULTS AND DISCUSSION

The major conclusion that can be drawn from the test results is that the unpolished diamond coated samples, whether fluorinated or not, significantly reduce wear on the SiC seal nose under dry conditions compared to uncoated SiC backfaces. In some cases, the wear was reduced by over an order of magnitude. The measured coefficients of friction under dry conditions were in the 0.1-0.3 range upon the start of the test. As the test proceeded (6 minutes), the backface temperature rapidly reached temperatures of 160-280 °C; concomitantly, the measured coefficients of friction increased to a range of 0.3-0.7. Table 1 presents the wear results obtained for dry conditions. Note that for the limited number of tested samples, no conclusions can be drawn as to the efficacy of fluorinating

diamond films. Figures 3 and 4 present photographs of a fluorinated diamond coated backface after wet and dry testing respectively; note the glassy surface finish. It should be noted that under wet conditions, little wear is observed for both diamond and uncoated backfaces. Likewise, the measured coefficients of friction are in the range of 0.05-0.1 after a short initial run-in period. These results indicate the high quality of the diamond films produced by the hot filament technique.

Table I - DRY WEAR TESTS

BACKFACE MATERIAL	BACKFACE WEAR (in.)	SEAL NOSE WEAR (in.)
SiC	0.002300	0.003250
F-Diamond	0.000075	0.000253
F-Diamond	0.000038	0.000650
H-Diamond	0.000075	0.000200

We speculate that the low wear of the silicon carbide nose piece is due to the convolution of two effects. The much harder diamond quickly removes any silicon carbide asperities, reducing the mechanical interaction between the surfaces. Furthermore, the silicon carbide residue thus produced oxidizes to a hydrated silicon oxide slurry which provides some lubricity, which further reduces wear [5]. The high coefficients of friction obtained might be caused by local fracture of the silicon carbide which does not significantly increase wear.

It is difficult to directly compare the results obtained in these studies with those presented elsewhere. (See Dugger et al. for a review of the substantial literature on diamond tribology studies.)[6] Most of the literature describes tests performed under low slide velocity conditions where little frictional heat is generated so as to allow comparison between studies.[7-12] What is generally found is that diamond films exhibit an initial high coefficient of friction followed by a gradual decrease to below a value of 0.1 for high quality films. The diamond films in this study, even under wet conditions, show this same behavior, starting with a friction coefficient of 0.3 - 0.5 and decreasing to a value of approximately 0.05. This achievement without any polishing indicates that the films grown by the hot filament technique are of an unusually high quality. It should be noted that the fluorinated samples exhibit a much shorter run-in period compared to the non-fluorinated sample.

The major results can be summarized by the following points:

- Comparatively thick (10μm), fine grained (1-3μm), adherent high quality diamond films can be deposited on reaction-bonded silicon carbide substrates using the biased filament technique;

- Diamond films can be efficiently fluorinated using a remote discharge technique without the need for annealing or other surface chemical treatment; and

- Both fluorinated and unfluorinated diamond coated silicon carbide substrates induce markedly less wear on SiC test pieces compared to uncoated substrates under non-lubricating (dry) running conditions.

This last result is extremely important because silicon carbide typically suffers heavy wear and does not survive dry running conditions which are frequently encountered in critical pumping applications. The question of whether fluorinated films offer any advantage over non-fluorinated films is still not answered. Further testing is still required; in any case, the answer is probably application specific.

ACKNOWLEDGMENTS

REFERENCES

1. "Diamond and Diamond-Like Films", edited by A.J. Purdes, B.S. Myerson, T.D. Moustakas, K.E. Spear, K.V. Ravi, and M. Yoder, Proc. Vol. 89-12, The Electrochemical Society (Pennington, N.J.)

2. SDIO/ISTR-ONR Diamond Technology Initiative Symposium Summaries, 1986-1989, Palisades Institute for Research Services, Inc. (New York, N.Y.)

3. M.N. Gardos anbd K.V. Ravi, "Tribological Behavior of CVD Diamond Films p. 475 in Reference 1

4. M.N. Gardos, B.L. Soriano, D.E. Patterson, R.H. Hauge, and J.L. Margrave, Proc. of 2nd Int'l Symp. on Diamond Materials, Electrochemical Society Proc. 91-8,365 (1991)

5. T.E. Foscher and W.M. Mullins, J. Phys. Chem., 96, 5690 (1992)

6. M.T. Dugger, D.E. Peebles, and L.E. Pope, in "Applications of Surface Science and Advances in Tribology," Y.W. Chung, A.M. Homola, and G.B. Street, eds., Amer. Chem. Soc. Books, Washington, DC (1992).

7. D.E. Peebles and L.E. Pope, J. Mater. Res. Soc. 5, 2589 (1990).

8. Z. Feng and J.E. Field, J. Phys. D. Appl. Phys. 25, A33 (1991).

9. I.P. Hayward and I.L. Singer, 2nd Int'l Conf. on New Diamond Science andTechnology, p. 785 (1991).

10. M.S. Wong, R. Meiluras, T.P. Org, and R.P.H. Chang, Appl. Phys. Lett. 54, 2006 (1989).

11. M.N. Gardos, B.L. Soriano, D.E. Patterson, R.H. Hauge, and J.L. Margrave, Proc. of 2nd Int'l Symp. on Diamond Materials, Electrochemical Society Proc. Vol. 91-8, p. 365 (1991).

12. P.J. Blau, C.S. Yust, L.J. Heatherly, and R.E. Clausing, in "Mechanics of Coatings," Leeds-Lyon 16 Tribology Series, D.Dowson, C.M. Taylor, M. Godet (editors), Elsevier (1990).
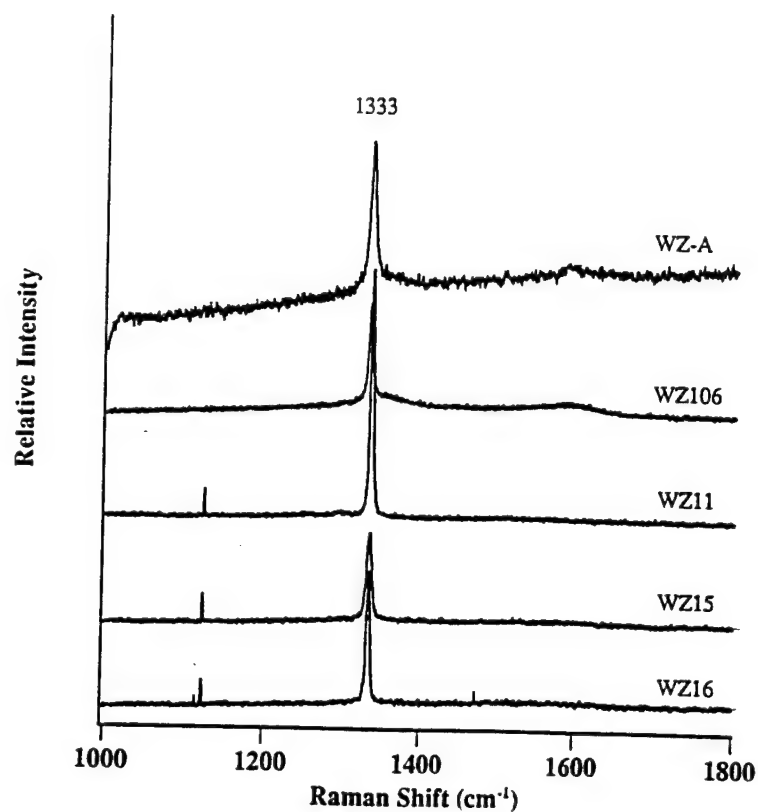
Figure 1. Raman spectra of diamond films produced on various substrates. Samples WZ11,15, and 16 are silicon carbide and the other two are Si_3N_4.
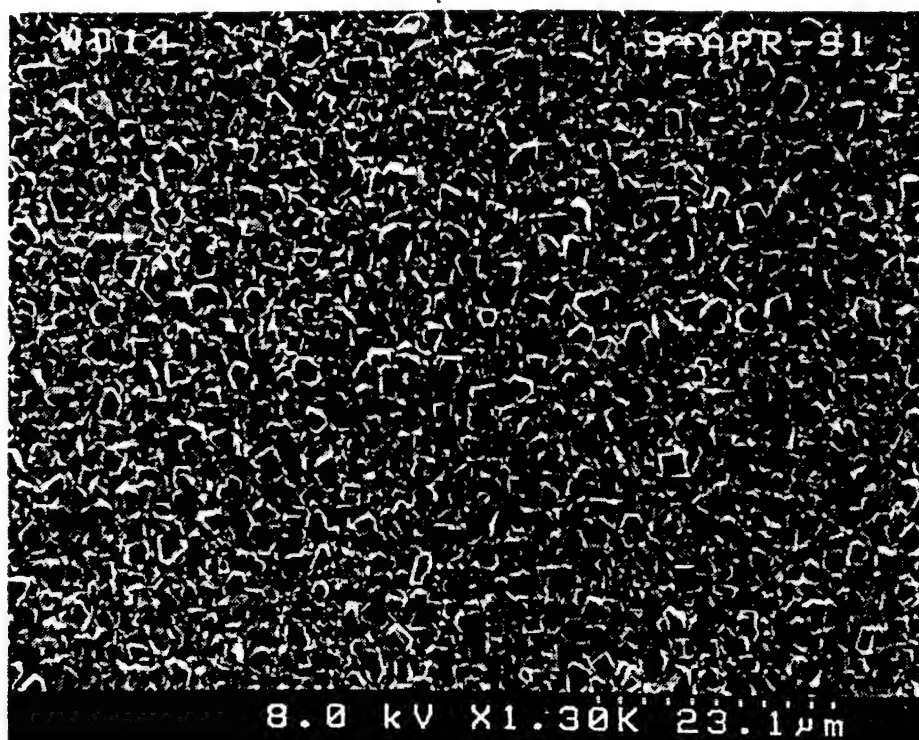

Figure 2. Scanning electron micrograph of diamond coated silicon carbide before fluorination.
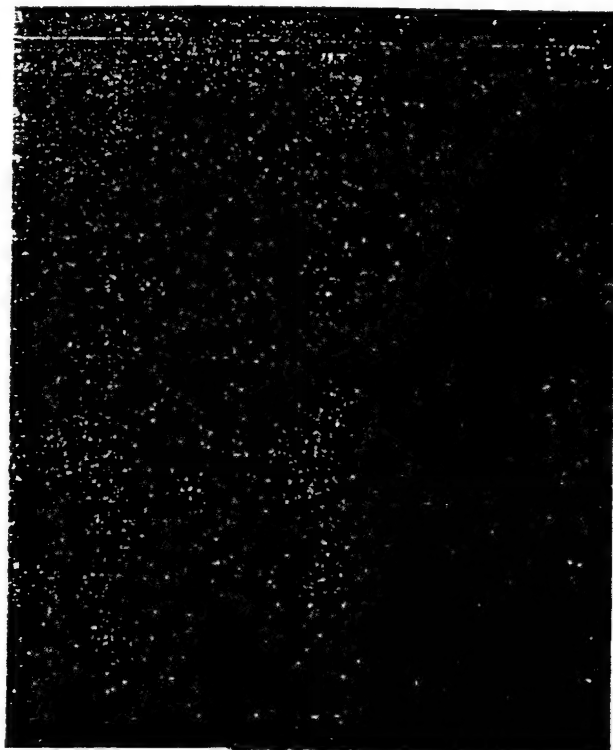
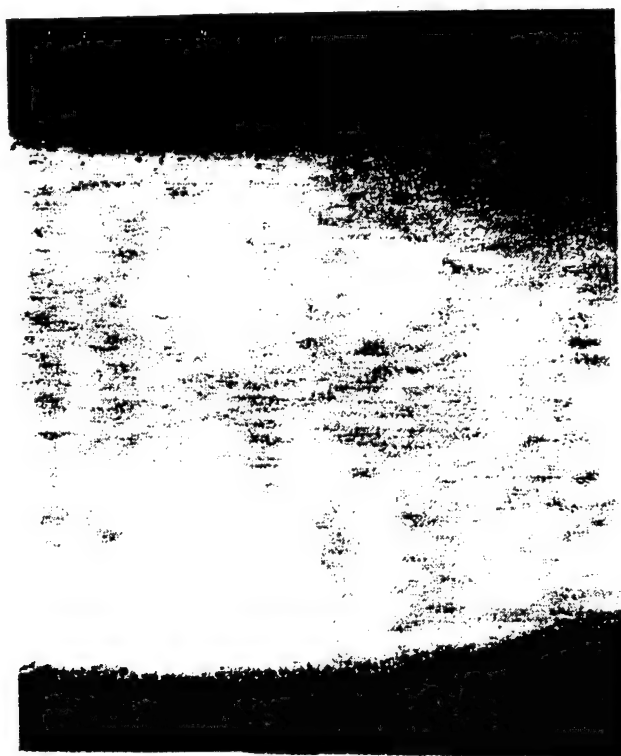Figure 3. Photograph of fluorinated diamond backface after wet testing

Figure 4. Photograph of fluorinated diamond backface after dry testing

UHV-COMPATIBLE ELECTROSTATICALLY-DRIVEN TUNING FORK CHOPPER

by

Paul L. Kebabian, Spiros Kallelis, David D. Nelson, Jr. and Andrew Freedman

September 1992

UHV-COMPATIBLE ELECTROSTATICALLY-DRIVEN TUNING FORK CHOPPER

Paul L. Kebabian, Spiros Kallelis, David D. Nelson, Jr. and Andrew Freedman
Center for Chemical and Environmental Physics
Aerodyne Research, Inc.
45 Manning Road, Billerica, MA 01821

We have developed an electrostatically driven tuning fork chopper which is compatible with an ultrahigh vacuum (UHV) environment. Constructed with a commercially available tuning fork using stainless steel and alumina parts, the chopper is capable of operating while exposed to high temperature samples and corrosive gases. Operation in a UHV environment while modulating both optical and molecular beams is demonstrated.

INTRODUCTION

The development of beam modulating instrumentation that is compatible with the high level of cleanliness required in ultrahigh vacuum (UHV) systems ($P \leq 1 \times 10^{-8}$ Torr) presents a difficult problem. One possible solution is the magnetically driven tuning fork chopper which has been used for over thirty years in conjunction with phase sensitive detection to provide an enhanced means of signal recovery in systems using photon and molecular beams.[1,2] Commercial devices at moderate cost are available. Unfortunately, the use of plastics and epoxies in these devices is not appropriate to UHV systems. In addition, exposure of the chopping device to corrosive gases and heat generated by hot substrates rule out the use of simple encapsulating strategies. Experiments conducted in this laboratory require exposure of substrate surfaces to both atomic and molecular halogen gases at surface temperatures exceeding 1000K.[3,4] To solve this problem, we have developed an electrostatically driven tuning fork chopper constructed entirely of UHV-compatible metals and ceramics. Unlike other electrostatically driven systems,[5,6] this one achieves a large vibration amplitude (several millimeters).

DESIGN AND CONSTRUCTION

Design of an electrostatically driven chopper with a large vibration amplitude offers several problems. The drive electrodes and tuning fork can be thought of as forming a capacitive system under an applied voltage; in order to generate a driving force over a large excursion, the drive electrodes must be placed out of the plane of desired motion. When an AC drive voltage is applied to the drive electrodes, forces (proportional to the square of the voltage) both parallel and perpendicular to the desired plane of motion are generated which will induce motion both in- and out-of-plane at resonance. Any design must maximize the former and minimize the latter; moreover, the fork and electrodes must stay in close proximity (a fraction of a millimeter) over the entire range of motion without shorting out the drive voltage.

80

Figure 1 presents a schematic of the mechanical details of the chopper assembly. The tuning fork proper consists of a set of tines to which vanes are attached. The nominal 500 Hz tine set, made from a carbon steel alloy, was purchased from Frequency Control Products7. The ends of the tines are enlarged, allowing for a set of slots in which the vanes can be attached. Stainless steel vanes (0.25 mm thick) were attached to the tines by spot welding them in the slots using a thin layer of platinum as a binder. The drive electrodes are located approximately 0.1 mm beneath the enlarged areas at the end of the tines. The ends of the electrodes are at the middle of the enlarged region. Thus, the in-plane motion of the tuning fork causes a change in the capacitance between the drive electrodes and the tines, exerting an in-plane electrostatic force. Note that the in-plane motion cannot cause the electrodes to short to the tines. Furthermore, the excitation of the out-of-plane (flapping) motion is minimized by the chosen location of the drive electrodes in that the out-of-plane stiffness of the tines is much greater than that of the vanes.

The pickoff electrodes are located over the vanes at the outer end at a spacing of a few tenths of a millimeter. This location maximizes sensitivity to in-plane motion and minimizes pickup from the drive electrodes. An electrostatic shield covers the drive electrodes to minimize pickup of the drive voltage, but this remains a problem whose solution is discussed below. All insulating bushings are constructed from non-porous alumina; the base and supporting structure are made from stainless steel. The chopper is situated so that the beam passes through the region between the ends of the pickoff electrodes. At rest, the gap between the vanes is 1.5 mm.

Mechanically, there is relatively weak coupling between the two tine/vane assemblies. Thus, to achieve the highest mechanical 'Q', they must be set to the same resonant frequency. This was done by sweeping the drive frequency (using the drive circuitry described below), while observing the vanes under a microscope. The vane on the side having the lower resonant frequency was ground down until the resonant frequencies were matched. At this point, the vibration of the tuning fork is decoupled from the base and maximum mechanical Q results. We were able to achieve Q≅1000 at 323 Hz. This value of Q is somewhat lower than one usually sees for magnetically driven forks in this frequency range; we believe that the cause of this is mainly imperfect matching of the frequencies. We emphasize that the ultimate performance of the chopper is dependent on matching the size and weight of the vanes as closely as possible. For less critical conditions, solder is typically used to match the weight the of the vanes so as to provide the desired frequency and high 'Q' typical of such choppers, an inappropriate option for UHV work.

Figure 2 presents a schematic of the circuitry used to drive the fork and monitor its motion. The drive voltage is typically 6 kV peak-to-peak. The force on the tines is proportional to the square of the drive voltage and thus the drive frequency is set to half the resonant frequency. The sensor electrodes are biased at 90V DC; the motion of the vanes, when C_{sense} is varied, causes a signal current proportional to dC_{sense}/dt at the resonant frequency. A much larger current, at the drive frequency, is present as a result of the coupling through stray wiring capacitance. To cancel this, potentiometers R1 and R2 add in-phase and quadrature signals at the drive frequency. Depending on

81

the phase shift introduced by the amplifier and transformer, it might be necessary to invert the drive voltage to R1 and/or R2; this was not the case for our apparatus. The output is displayed as a Lissajous pattern on the oscilloscope; at resonance, a typical signal of 30 mV p-p is observed.

To operate the chopper, the oscillator is first set slightly off resonance and R1 and R2 are adjusted to minimize coupling at the drive frequency. Then, the frequency is slowly swept through resonance until a signal at twice the drive frequency is observed. This pattern is the sum of a component at twice the drive frequency (parabolic shape) and a component at four times the drive frequency. We ascribe the latter component to an out-of-plane motion caused by the center of mass of one or both of the vanes being above or below the point of attachment to the tines. One could synchronously detect the signal component at twice the drive frequency and use that to stabilize the oscillator frequency. We have not found this to be necessary as the chopper operation has been sufficiently stable for periods up to an hour.

We have noted that the maximum chopper excursion is greatly reduced at atmospheric pressure. This results from the fact that a sufficiently high voltage cannot be used to drive the chopper due to electrical breakdown from the driving electrodes to the tines.

PERFORMANCE

The tuning fork chopper was tested in a molecular beam apparatus used to study the chemistry of surfaces under ultrahigh vacuum conditions. It comprises three chambers: the first houses the sample manipulator and various beam sources, both neutral and ionic; the second contains surface analysis diagnostics (X-ray photoelectron spectrometer and low energy electron diffraction); and the third contains a differentially pumped quadrupole mass spectrometer (Extrel). The last chamber is maintained at a pressure 300 times lower than the sample chamber when a molecular beam is being used to irradiate the sample. The tuning fork chopper is mounted at the opening to the mass spectrometer chamber so as to provide for phase sensitive detection of species emanating from the surface. This arrangement is suitable for both beam scattering and surface desorption experiments.

The first test on the tuning fork chopper under vacuum was an optical one. A HeNe laser beam was directed through the aperture of the tuning fork chopper, into the mass spectrometer chamber and out through a Pyrex window, where it was monitored by a silicon diode. Figure 3 presents the signal obtained. Note that the attenuation of the laser beam amounts to 80-90% at an operating voltage of 6 kV. Attempts to increase the voltage and thus the range of travel of the vanes failed due to electrical breakdown between the tines and electrodes. The limited peak-peak amplitude of 3mm may be due in part to the relatively low Q, as well as the limited extent of the enlarged regions at the ends of the tines where the driving force is applied.

The next test involved scattering a thermal effusive beam of argon off a polished and annealed GaAs wafer (Litton) into the mass spectrometer. The argon beam was detected at mass 40 using the Extrel quadrupole filter and Channeltron particle multiplier (Galileo) in a pulse counting mode. The

individual pulses were amplified and converted to TTL pulses by a discriminator, and were routed to dual 4MHz counters on a LabMaster board (Scientific Solutions) interfaced with an 80286 personal computer. Three other counters on the board are used to trigger and gate the counters used to record signals from the mass spectrometer. This allows two counting windows to be established within each chopper cycle. The width and location of each cycle is adjustable under computer control to match the characteristics of a given chopper. One can establish two large windows coincident with the chopper being open and closed and thereby operate in a digital lockin amplifier mode. Alternatively, one can establish two small windows and scan their time delay to acquire the shape of the waveform.

Figure 4 presents results obtained in the latter mode of operation by collecting signal as a function of phase angle with respect to the chopper drive frequency and signal averaging for a period of an hour. We note that given the distance between the beam aperture and chopper (10 cm), the bulk of the signal comprises ionization of background gas that has entered the detector chamber without passing through the chopper. The modulation depth of 4% is in accord with the signal expected after taking into account the strength of the scattered beam, the background pressure, and the geometry of the apparatus. The chopper has also been shown to properly function when a substrate heated to 1000K (a 500W heat source) is placed within two centimeters distance while a beam of 5% fluorine in argon is irradiating the sample.

In conclusion, we have developed an electrostatically driven tuning fork chopper for modulation of molecular and optical beams that is compatible with an ultrahigh vacuum environment. Constructed of only stainless steel and alumina parts (except for the tuning fork itself which is of a non-stainless steel), the chopper has been operated in an environment which contains corrosive gases and high temperatures.

REFERENCES

1. Y.T. Lee, J.D. McDonald, P.R. LeBreton and D.R. Herschbach, Rev. Sci. Instrum., 40, 1402, (1969)

2. K.C. Herr, P. B. Forney and G.C. Pimentel, Appl. Opt. 11, 493 (1972)

3. A. Freedman and C.D. Stinespring, Appl. Phys. Lett. 57, 1194 (1990)

4. A. Freedman and C.D. Stinespring, J. Phys. Chem. 96, 2253 (1992)

5. R.R. Shreve, "Electrostatic Tuning Fork Resonator", U.S. Patent No. 3,350,667 (1967)

6. A. Fartash, I. Schuller and M. Grimsditch, Rev. Sci. Instrum. 62, 494 (1991)

7. 6120 Woodside Ave., Woodside NY, 11377

TUNING FORK CHOPPER
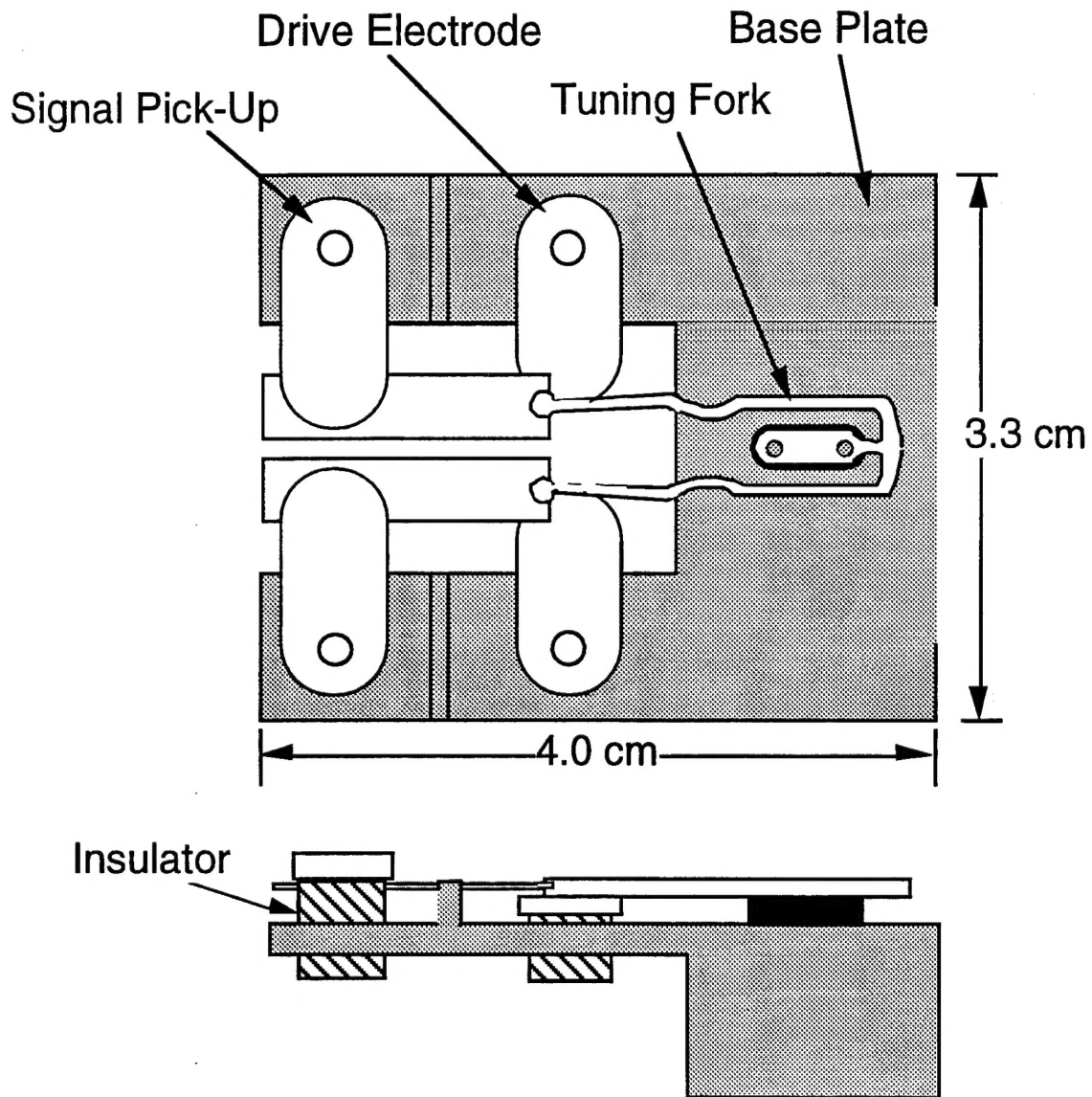
Figure 1. Schematic of mechanical assembly of tuning fork chopper.
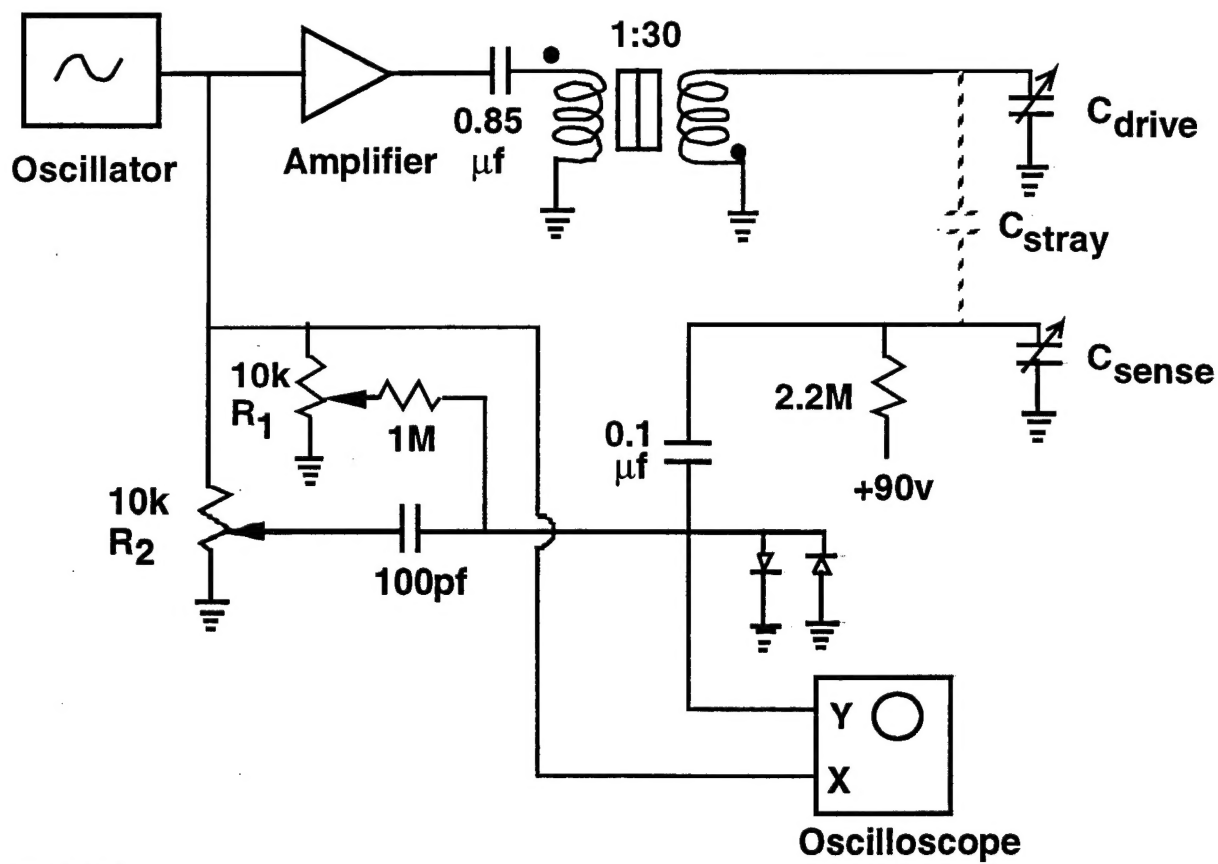
Figure 2. Circuit diagram for drive electronics for tuning fork chopper.
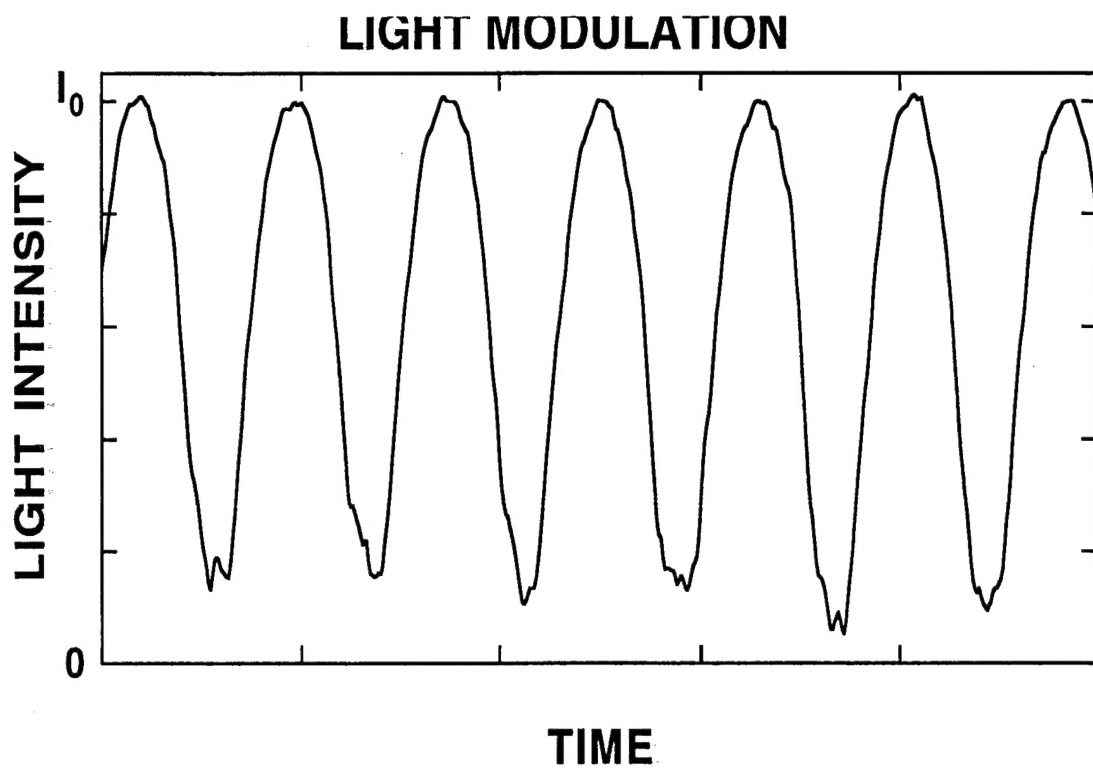
MP92-244/P.K.

Figure 3. Trace of signal obtained from a modulated HeNe laser beam which has been bounced off a substrate and through the tuning fork chopper.
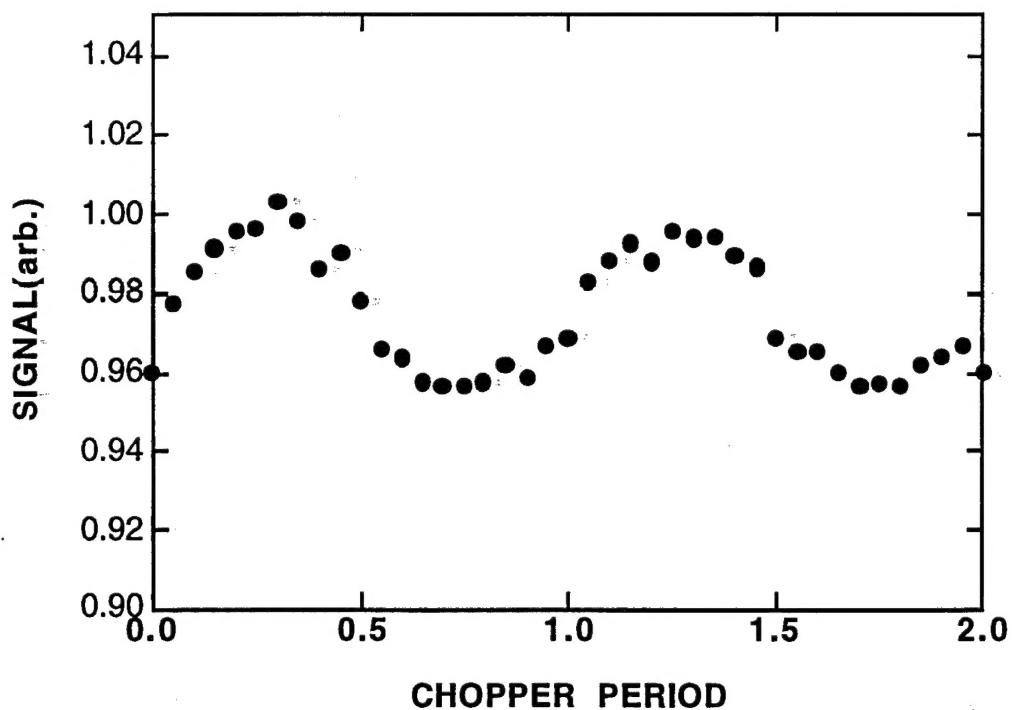
MODULATION OF SCATTERED Ar BEAM

Figure 4. Mass spectrometer signal at mass 40 obtained from modulation of an argon beam which has been bounced off a substrate. The chopper is situated between the substrate and mass spectrometer entrance. The level of modulation represents recovery of the beam signal from background signal.